A thesis for the Degree of Doctor of Philosophy

# Integrated Dynamic Analysis of Floating Offshore

# Contra-Rotating Vertical-Axis Wind Turbine

Hyebin Lee

MULTIDISCIPLINARY GRADUATE SCHOOL PROGRAMME

FOR WIND ENERGY

JEJU NATIONAL UNIVERSITY

2020. 2.

# Integrated Dynamic Analysis of Floating Offshore Contra-Rotating Vertical-Axis Wind Turbine

## Hyebin Lee

## (Supervised by Professor Yoon Hyeok Bae)

A thesis submitted in partial fulfilment of the requirements
for the degree of Doctor of Philosophy

2020. 02.

This thesis has been examined and approved by

_____
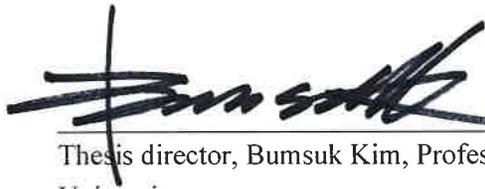
Thesis director, Bumsuk Kim, Professor, Faculty of Wind Energy Engineering, Jeju National
University

_____

Yoon Hyeok Bae, Professor, Dep. of Ocean System Engineering, Jeju National University

_____
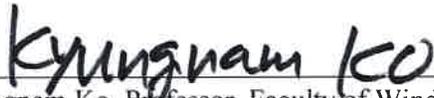
Kyungnam Ko, Professor, Faculty of Wind Energy Engineering, Jeju National University

_____
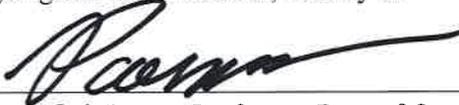
Dong-Guk Paeng, Professor, Dep. of Ocean System Engineering, Jeju National University

_____

Jungchul Choi, Researcher, Korea Institute of Energy Research

2020. 1. 8.
Date

MULTIDISCIPLINARY GRADUATE SCHOOL PROGRAMME
FOR WIND ENERGY
JEJU NATIONAL UNIVERSITY

# ABSTRACT

As the offshore wind industry has been recently played a significant role in the worldwide wind energy market, wind farms are moving towards deeper water. At deeper water depth, floating wind turbines could be more economical than the bottom-fixed wind turbines. Along with this trend, vertical-axis wind turbines (VAWT) have centred on the industry due to its advantages under the offshore environment. In the case of the VAWT, the centre of mass is located lower than the horizontal-axis wind turbines because the mechanical systems are placed at the tower bottom. For this reason, more stable motions are anticipated by adopting the VAWT as an up-and-coming player. When the VAWT is adopted for the floating wind turbine, however, the effect of the torque results in the yaw moment on the supporting tower and platform. Loads continuously acting on the structure, continued platform motions and resulting mooring tension requires the robust design and raises the manufacturing and maintenance costs. Hence, this study suggests a contra-rotating VAWT to mitigate the structural loads and platform motions by the counterbalanced torque produced by the two rotors.

To investigate the contra-rotating VAWT, this study firstly develops and validates the

integrated analysis code for the floating VAWT and finally extends it to be able to consider the contra-rotating rotor. The integrated analysis code was developed based on the FAST's code structure to inherit its openness and the required modules for the integrated analysis of the floating offshore turbines. This research used a double-multiple streamtube model (DMSM), which gives relatively accurate results despite faster and simpler calculation compared to the CFD analysis, as the aerodynamic model of the integrated analysis code. Not only the aerodynamics calculations but the integrated analysis results of the developed code were verified by comparing its results to those from the references and CFD analysis.

The developed integrated analysis code was further advanced for the analysis of the contra-rotating rotor. Using this analysis code, the structural loads and motions of the contra-rotating VAWT were assessed. As a result, the contra-rotating VAWT had reduced power than the conventional VAWT. Nevertheless, the contra-rotating VAWT showed better structural loads and, in the case of the floating model, platform motions as well, resulting in significant decreases in not only the mean values but the standard deviations. The decrease in the average of the structural loads means the tower and substructure can be less sturdy, and less standard deviation indicates the fatigue life can be extended. Reduced platform motions would cause less tension in the mooring system so that the design of the mooring lines could be less robust. Based on the results so far, reduced structural loads with similar power to that of the conventional VAWT is anticipated by the optimisation of the rotor design and thus the design of towers, substructures, and mooring system.

# 요약문

풍력발전기 시장이 해상으로 영역을 확장해감에 따라 해안에서 멀리 떨어진 깊은 수심에서의 풍력발전에 관심이 집중되고 있다. 설치 수심이 깊어질수록 해저 고정식 풍력발전기보다 부유식 풍력발전기를 설치하는 것이 경제적이게 되므로 이에 대한 연구가 활발히 진행되고 있다. 해상 풍력발전에 대한 관심과 더불어 해상환경에서 기존의 수평축 풍력발전기보다 이점을 갖는 수직축 풍력발전기(VAWT)에 대한 관심도 증가하고 있다. VAWT의 경우 기계 장치들이 타워 하단부에 위치하기 때문에 수평축 풍력발전기에 비해 무게중심이 상대적으로 낮은 곳에 위치하게 되므로 보다 안정적이다. 그러나 한 방향으로 지속적으로 회전하는 로터에 의해 타워에 하중이 작용하고 부유식으로 사용될 경우 하부구조물의 yaw 운동이 발생하게 된다. 지속적으로 타워에 작용하는 하중과 하부구조물의 운동은 각 요소에 피로하중을 유발하기 때문에 더욱 강건한 설계가 필요하며 이에 따라 제작 및 유지 비용이 증가한다. 이러한 문제의 해결을 위하여 본 연구에서는 상반회전 로터를 이용하여 같은 축을 공유하며 서로 반대방향으로 회전하는 두 로터에서 각각 발생하는 토크가 회전축에 작용할 때 그 영향이 상쇄되도록 하였다.

부유식 상반회전 VAWT의 영향을 평가하기 위한 통합해석을 실시하고자 다음과 같은 순서로 연구를 진행하였다. 먼저 부유식 VAWT의 통합해석코드를 FAST의 구조를 기반으

로 개발하고 이를 검증하였다. VAWT의 공력 해석을 위하여 CFD 해석에 비해 비교적 빠르고 단순한 계산으로도 정확한 결과를 얻을 수 있는 이중다류관 모델(DMSM)을 사용하였다. 공력 해석 결과를 비롯하여 통합해석 결과를 선행 연구 및 CFD의 계산결과와 비교하여 개발된 통합해석코드를 검증하였다. 최종적으로 부유식 상반회전 VAWT의 통합해석을 위하여 통합해석코드를 보완하였으며 이 코드를 이용하여 해석된 결과를 기존의 부유식 VAWT의 결과 비교하여 평가하였다.

동일한 크기의 기존 VAWT와 비교하였을 때 상반회전 VAWT의 출력은 다소 감소하는 경향을 보였지만 상반회전 로터로 인하여 타워에 작용하는 하중이 상쇄되고 하부구조물의 운동도 감소하는 효과를 보였다. 타워 하중 평균값의 감소로 인하여 타워 및 하부구조물의 재설계를 통한 제작비 감소를 기대할 수 있으며, 표준 편차의 감소로 피로하중은 줄어들고 피로수명은 늘어날 수 있다. 감소된 하부구조물 운동의 평균값은 계류선에 작용하는 장력을 감소시키며, 표준편차의 감소는 피로하중을 줄이는데 큰 역할을 할 것으로 기대할 수 있다. 본 연구에서 해석을 진행한 상반회전 VAWT는 초기 연구를 위하여 설계된 단순한 모델이기 때문에 추후 설계 최적화를 통하여 기존의 VAWT와 비슷한 수준의 출력을 가지면서 타워의 하중이나 하부구조물 운동의 관점에서 향상된 결과를 갖는 설계안을 도출해낼 수 있을 것으로 기대한다.

# Acknowledgements

This thesis is written under the supervision of Professor Yoon Hyeok Bae. I would like to express my sincere gratitude to him for the guidance he has given for this work. During my PhD, working for not only this work but other researches, I was able to learn a wide range of knowledge from him and gain a researcher's attitude. Once again, I am truly thankful to him.

I would also like to express my deepest appreciation to the rest of my committee: Bumsuk Kim, Kyungnam Ko, Dong-Guk Paeng and Jungchul Choi, for reviewing this thesis and providing their invaluable insight on my work.

I would like to extend my deepest gratitude to Professor Il-Hyoung Cho at the Department of Ocean System Engineering. I have learnt a great deal with his guidance for various researches for years from undergraduate to PhD.

I must also thank Professor Jinho Bae and Chong Hyun Lee at the Department of Ocean System Engineering and Professor Jongchul Huh at the Department of Mechanical Engineering for their support and encouragement.

I am very grateful to all members of the Ocean Engineering Laboratory, Dr Haengsik Ko, Dr Sunny Kumar Poguluri, Dr Jeongrok Kim, Dongeun Kim and Arun George, for their

constructive and helpful advice on the work with this thesis and generous support.

I would like to thank all those who directly or indirectly help me with my research and encourage me during my PhD.

And finally, I dedicate this thesis to my mother, who always gives me unlimited love and understanding.

# 감사의 글

모두가 그렇듯 저 역시 많은 고민도 하고 어려움도 느꼈던 시간이었습니다. 이 시간동안 어긋나지 않고 계속하여 달릴 수 있도록 이끌어 주신 하느님께 감사드립니다.

먼저 본 학위논문 뿐만 아니라 박사학위 과정 내내 지도해주신 배윤혁 교수님 감사합니다. 처음 방향을 잡지 못하고 갈팡질팡하던 시간부터 교수님의 아낌없는 지도와 격려 덕분에 무사히 마무리할 수 있었습니다. 교수님과 함께 연구하는 시간동안 다양한 연구 지식을 비롯하여 연구자의 태도에 대해서도 많은 것을 보고, 느끼고, 배울 수 있었습니다. 진심으로 감사드립니다. 학위논문 심사를 맡아 주신 풍력공학부의 김범석 교수님과 고경남 교수님, 해양시스템공학과의 팽동국 교수님, 한국에너지기술연구원의 최정철 박사님께도 감사의 인사를 드립니다. 학위논문이 더 나은 방향으로 나아갈 수 있도록 해 주셨던 조언을 통하여 더 넓은 시각으로 연구를 바라보며 마무리할 수 있었습니다. 감사합니다. 박사학위 과정동안 좋은 연구들을 할 수 있도록 큰 도움을 주셨던 해양시스템공학과의 조일형 교수님 감사합니다. 그리고 늘 따뜻한 격려를 해 주셨던 풍력공학부 허종철 교수님, 해양시스템공학과의 이종현 교수님과 배진호 교수님께도 감사의 인사를 드립니다.

학위 논문 준비 기간 동안 본인의 일처럼 함께 고민해주고 많은 배려를 해주었던 해양공학실험실의 고행식 박사님, Dr Sunny Kumar Poguluri, 김정록 박사님, 김동은님, George Arun 감사합니다.


이 외에도 가까운 곳에서, 또 먼 곳에서 저를 응원해 주셨던 모든 분들 감사합니다. 앞으로 어디서 어떻게 제가 제 꿈을 펼쳐 나갈지 모르지만 지금의 순간을 잊지 않고 자만하지 않으며 늘 감사하는 마음으로 성실하게 임하도록 하겠습니다.


마지막으로 곁에서 아무런 조건없이 변함없는 사랑으로 보듬어 주시는 어머니께 이 논문을 바칩니다.

# CONTENTS

# LIST OF FIGURES

# LIST OF TABLES

# Chapter 1

# INTRODUCTION

## 1.1 WIND ENERGY TECHNOLOGY

### 1.1.1 GENERAL

It is obvious that renewable energy keeps growing its portion of total energy supply in the future by current and planned energy policies of many countries, which is because of arising people's attention to the environment and climate change. Figure 1.1 shows the total primary energy supply (TPES) and the share of renewable and non-renewable energy in 2015 and 2050, including energy supply in electricity generation as well as that in district heating and cooling, industry, buildings and transport sectors. While Reference Case, including commitments made in Nationally Determined Contributions (NDCs) by the Paris Agreement and other planned targets, forecasts the total share of renewable energy will increase from around 15% of the TPES in 2015 to 27% by 2050, IRENA(International Renewable Energy Agency) foresees even more to two-thirds by 2050 (Remap Case) [1]. Especially in the power

sector, the share of renewables will rise to 85% of total electricity generation in 2050 as can be seen in Figure 1.2. According to this figure, wind capacity will emerge as the leader in this trend among many renewable sources.
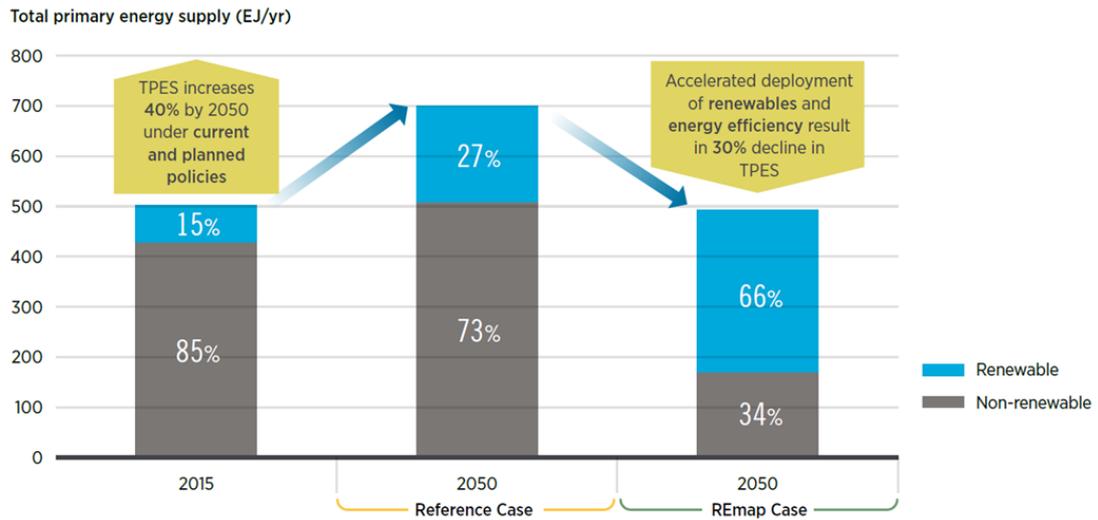


Figure 1.1 Global total primary energy supply in 2015 and 2050 [1]
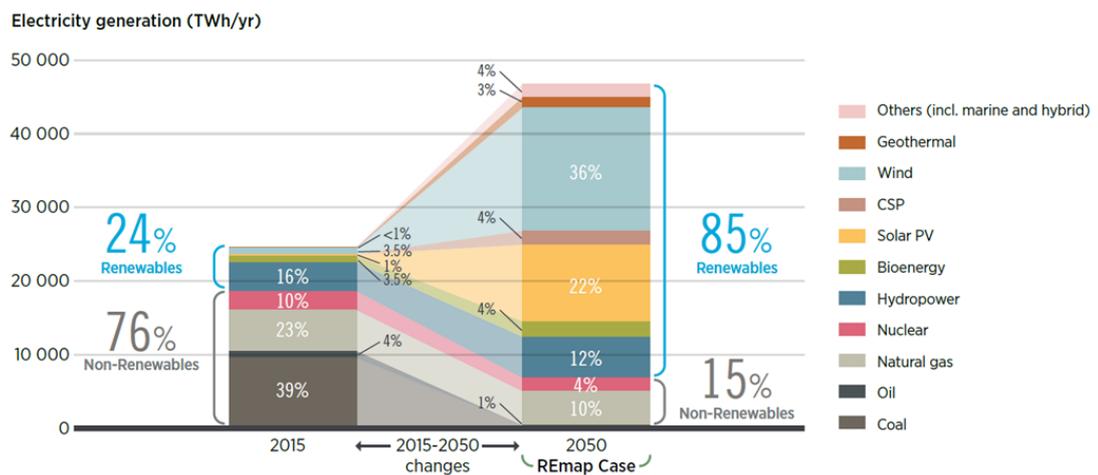


Figure 1.2 Electricity generation forecasted by REmap Case [1]

Since wind energy has been focused by the countries which seek unlimited and clean energy for the electricity, onshore wind turbine technology has reached maturity for the last decades. Not only the development of the technology but also Levelized cost of electricity (LCOE) is vital to evaluate the value of energy resources. LCOE is the standard measure of defining the cost of not only wind energy but other energy sources for several years. As shown in Table 1.1, onshore wind energy secures cost competitiveness compared to solar energy or even to coal.

Table 1.1 Global Levelized cost of electricity (US Dollars per MWh) [2]

| source | Onshore wind | Utility-scale solar | Coal |
|---|---|---|---|
| UNEP/BNEF in 2019 | 50 | 57 | |
| Lazard in 2018 | 29 | 36 | 36 or 60 |
| Bloomberg in 2018 | 55 | 70 | |
| IRENA in 2018 | Renewables projected to be equal or below the cost of conventional sources | | |
| EBRD in 2018 | Renewables are now the cheapest energy source | | |

When it comes to the offshore wind, LCOE is still higher than onshore wind and other energy sources but has a decreasing trend over the last decade (Figure 1.3). While LCOE of onshore wind energy has been remained relatively constant and started to drop again since 2016, that of offshore wind energy has been notably decreased since 2012 and roughly halved in 2018. As LCOE is affected by capital expenditures (CapEx) and operational expenditures (OpEx), the technologies to solve the problems which an offshore wind turbine (OWT) are

having due to its characteristics and environment could lead to the further decrease in LCOE

in the future.
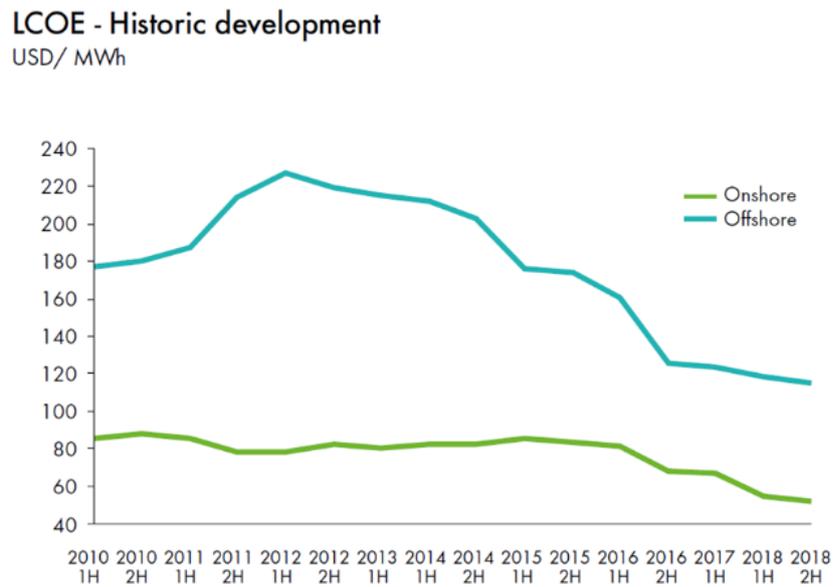


Figure 1.3 LCOE development [3]

Despite its weak cost competitiveness, OWTs have been steadily focused by wind

industries. Compared to onshore wind turbines, OWTs has advantages and disadvantages.

Since the onshore wind turbines frequently face objections of the residents due to its noise

and sight problems, onshore wind farms usually have a limit in the area. In the case of the

offshore wind turbines, the problems with the fishery and ecosystem of the sea could arise,

but the offshore wind turbines do not usually have the limit of the site because of the vast sea

area. There might be a problem with the water-depth causing the high costs and risks, but

appropriate types of substructures or platforms could overcome it. However, due to the harsh and unexpectable sea environment, the OWTs face many challenges and difficulties in operation and maintenance are also one of the disadvantages.

The offshore wind turbines can be categorised by its supporting type. One is bottom-fixed OWT (BFOWT), and another is floating OWT (FOWT) as can be seen in Figure 1.4. The choice between BFOWT and FOWT is usually based on the water depth of the installation site in order to reduce the installation cost. It is widely known that the FOWT is better in the case of deep water from the economic point of view.



Figure 1.4 Offshore wind turbines: bottom-fixed type (three from left) and floating type (three from right) [4]

According to the IEA report, the steady reduction in LCOE of both BFOWT and FOWT along with the decreasing trend of the onshore wind turbine is continuously expected for the next few decades [5]. Figure 1.5 shows the Median LCOE reduction scenario by 2050 for the onshore wind turbine, BFOWT and FOWT. LCOE of the FOWT is anticipated to reduce by 38 % by 2050, and IEA experts predict the further decrease of more than 10 %. It can be achieved by several factors considering FOWT's characteristics.
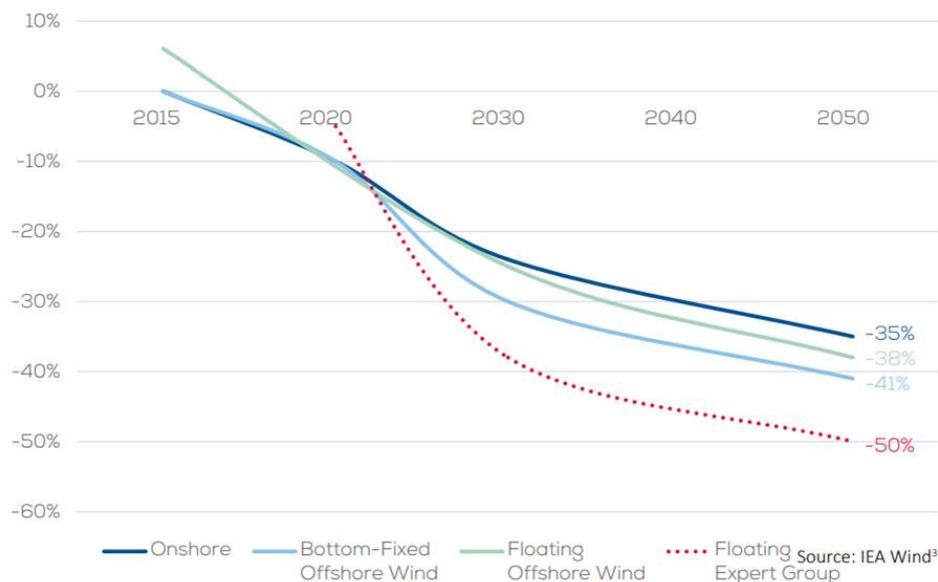


Figure 1.5 Median LCOE cost reduction scenario [6]

Since FOWT is free for water depth, turbines can be located in the area which is anticipated to extract much higher-averaged electricity. It will result in a decrease in LCOE. Furthermore, it leads to an increase in the turbine sizes and, as a result, higher output per turbine. The advanced designs of support structures, mooring solutions, electrical cables and

grid connections are the main factor to reduce LCOE of FOWT. The efficient installation

process of FOWT can lead to a further reduction of LCOE as well [5][6][7].

### 1.1.2 CLASSIFICATION OF THE WIND TURBINE

The machinery systems which use wind energy as a resource are based on the windmills.

From its initial functions and operating mechanisms, various types of wind turbines have

been developed. Its configurations and installation locations simply categorise wind turbines

as Figure 1.6.
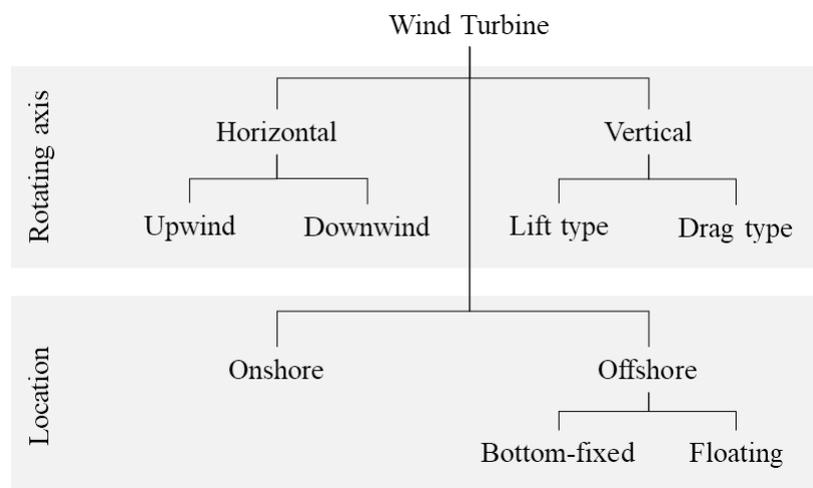
Figure 1.6 Wind turbine categories

Firstly, it can be categorised by the rotating axis – horizontal-axis (HAWT) and

vertical-axis (VAWT). The HAWTs have two types depending on the location of a rotor. If the

rotor faces the wind to avoid the wind shade behind the tower, it is an upwind turbine. On the

contrary to it, a downwind turbine has its rotor on the lee side of the tower. In the case of the VAWT, which wind forces are used to generate the power decides the type. Conventionally, VAWTs can be classified into two main features according to the type of aerodynamic forces generated by blades – lift type and drag type.

The installation site of the wind turbines categorises as onshore and offshore wind turbines. In the case of the offshore wind turbines, its substructure type again classifies them as bottom-fixed and floating wind turbines.

### 1.1.3 TREND AND PROSPECT

The power of wind energy depends on the swept area of the rotor of the turbine. For this reason, the size of the rotor diameter keeps growing to extract more energy. In the case of OWTs, there is less limit to its size compared to the onshore wind turbines. Additionally, having high capacity makes a profit under the offshore environment. These facts accelerate the evolution of the turbine size. MHI Vestas led the way in turbine capacity with its V164-9.5MW, V164-10.0MW and V174-9.5MW. GE Renewable Energy newly introduced the biggest wind turbine, named the Haliade-X 12MW, to be used as OWTs and has installed its first full prototype in Port of Rotterdam, the Netherlands on October 2019 for the testing phase (Figure 1.7). It features a world-firstly 12MW capacity and 220m rotor with three 107m long blades designed by LM Wind Power.

Figure 1.7 Haliade-X 12MW installed in the Port of Rotterdam, the Netherlands [8]

As the offshore wind is mostly not interrupted by the land shape, its qualities are better and steadier than those on land. For this reason, more stable power is expected by deploying OWTs. Furthermore, offshore wind speeds are typically faster than on land. Many advantages of the OWTs, previously mentioned, lead to a steady increase in demands in the wind industry. Currently, most offshore wind farms have lied in water depths below 50 m with the fixed foundations. Still, there are disadvantages and problems to be solved. Because the offshore environment is typically more severe than land, the substructure, mooring system and the turbine have the risk of damage. The high cost of construction and power transmission is one of the chief impediments. However, as expanding the floating offshore wind industry, the sites are becoming far further from the shore which has deeper depths more than 60 m or far larger area within the depths of 45 to 60 m [9]. It can help in getting rid of the objections, mainly

9

about the sight, noise, and coastal fishing and leisure.

Along with this trend, several full-scale prototypes of FOWTs have been deployed, and many studies on it have continued. The world's first floating wind farm, 30-MW Hywind Scotland Pilot Park, was situated 29 kilometres off the Aberdeenshire coast and in depths varying between 95 to 129m in October 2017 (Figure 1.8). In the farm, five Hywind floating wind turbines with spar-type substructure are placed. It operated at its maximum theoretical capacity of 65% during three months of the winter season after deployment, which exceeded the typical capacity of a bottom-fixed offshore wind farm. Recently, Equinor signed contracts for Hywind Tampen, which is a floating offshore wind farm powering the oil and gas platforms using 11 Hywind turbines with a total capacity of 88MW. The wind farm will be situated about 140 km from shore in 260 to 300m of water depth and between the Snorre and Gullfaks platforms.



Figure 1.8 30-MW Hywind Scotland Pilot Park [10]

WindFloat Atlantic is the world's largest floating wind power plant located 20km off the coast of Viana do Castello, Portugal. It comprises three units designed by Principle Power Inc for a total of 25MW of floating offshore wind power. Each unit has the V164-8.4MW turbine from MHI Vestas, placed atop a WindFloat semi-submersible substructure.
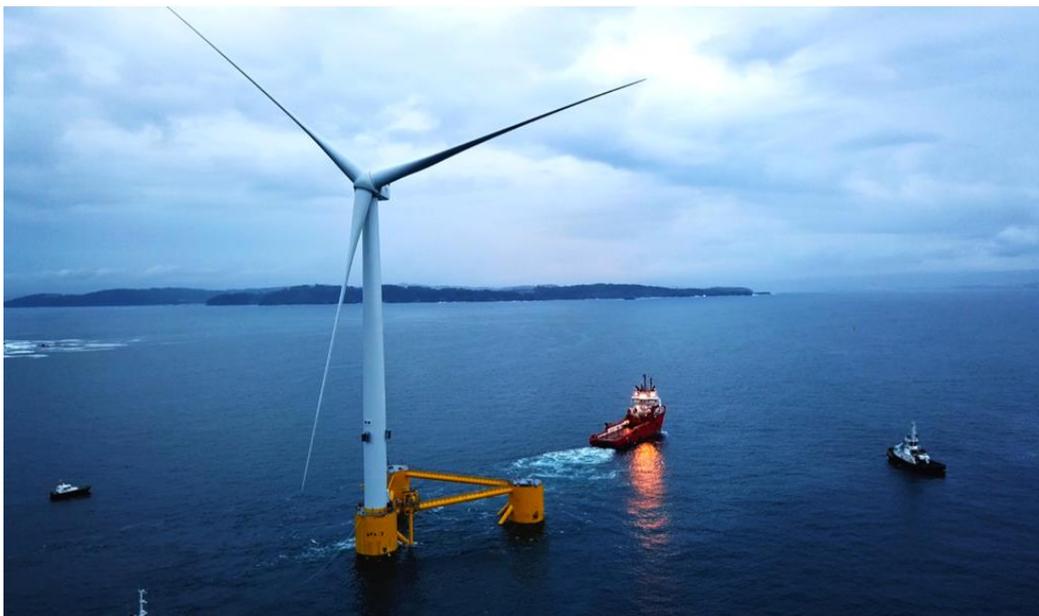


Figure 1.9 WindFloat Atlantic towed to its installation site [11]

Regardless of the water depth, the critical key for the growth of commercialisation is to reduce costs and risks. As the capacity is growing, the blade swept area becomes larger. Conventionally, the majority of the offshore wind turbine is HAWT, because its technology has matured and validated at the onshore site. In the case of the offshore wind turbines, which is deployed at relatively shallow sea ($< 50\ m$), the subsea structure is fixed at the sea bottom. However, when it comes to the FOWT for deeper water depth, the platform moves due to the

winds and, most importantly, waves. In this case, excessive weight focuses on the tower-top and causes unstable motion when the floating platform moves. Although the angular motion of the platform is small, it causes the large amplitude of the motion on the top of the tower. In this case, the HAWT, generally having a heavy mass on the tower-top, suffers from the stability problem due to high loading on top. Strategies such as damping plate and tuned liquid damper (TLD) can be utilised to overcome the unstable behaviour. In this respect, the VAWT, which has a lower located centre of mass, is a promising alternative to have a more stable motion. The details of VAWT are introduced in the following section.

## 1.2 VERTICAL AXIS WIND TURBINES

### 1.2.1 GENERAL

Vertical-axis wind turbines (VAWT) is one of the game-changers in the offshore wind energy market. It has a vertical shaft, and the rotor turns around this shaft (Figure 1.10). In the history of the wind energy, the researches on the VAWT had been carried out in the early stage along with the HAWT. However, the issues such as the fatigue problem and the low efficiency blocked the further development of the VAWT, and only the small-scaled VAWT has barely kept itself in existence.

Figure 1.10 4MW Darrieus VAWT, Éole, on the north shore of Quebec's Gaspe peninsula
[12]

As aforementioned, there are two types of VAWTs. The first is a Savonius wind turbine, which is the drag-type wind turbine, and the second is a Darrieus wind turbine, which turns a shaft using lift forces.

The Savonius wind turbine, developed by Finnish engineer Sigurd Savonius in the 1920s, is consisted of scoops, which employ a drag action to convert wind energy into torque to drive a turbine, as Figure 1.11 (a) [13]. Unlike wind turbines using lift forces to drive a turbine, the Savonius turbine cannot rotate faster than the approaching wind speed and has a value of TSR lower than 1. Despite its low efficiency, new designs such as a helical type of the Savonius wind turbine have been suggested [14][15]. The improvement has been shown in Figure 1.11 (b)¬(d).

(a)　　　　　　　(b)　　　　　　　(c)　　　　　　　(d)
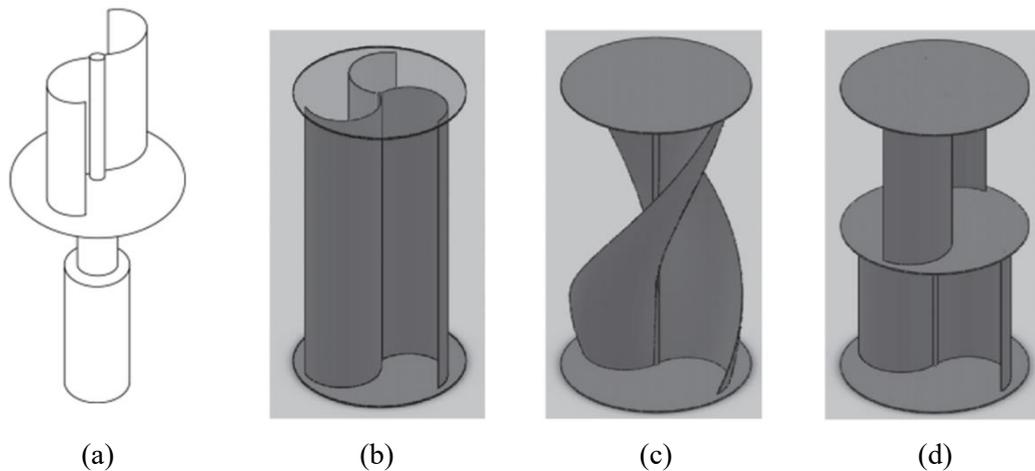
Figure 1.11 Savonius wind turbines: (a) Classic model [13]; (b) 3 Blades model; (c) Helical model; (d) Double-step model [15]

The Darrieus wind turbine is a lift-type wind turbine, which was introduced by George Jeans Marie Darrieus in 1931 [16]. He originally proposed the rotor having curved blades (Φ-rotor). The modern onshore VAWT was developed after the first oil crisis, and several studies on the VAWT followed, especially in the US and Canada [17]. In the UK, a different type of Darrieus wind turbine was developed and studied in the 1980s and 1990s. It is a straight-bladed (H-rotor) Darrieus wind turbine. It was designed to reduce blade manufacturing costs and simplify the support structure. Although the fatigue problems and unsuccessful operation due to failures made further development of the Darrieus wind turbine difficult, researches on the VAWT has been continued. Figure 1.12 shows the brief development history of the Darrieus wind turbine.
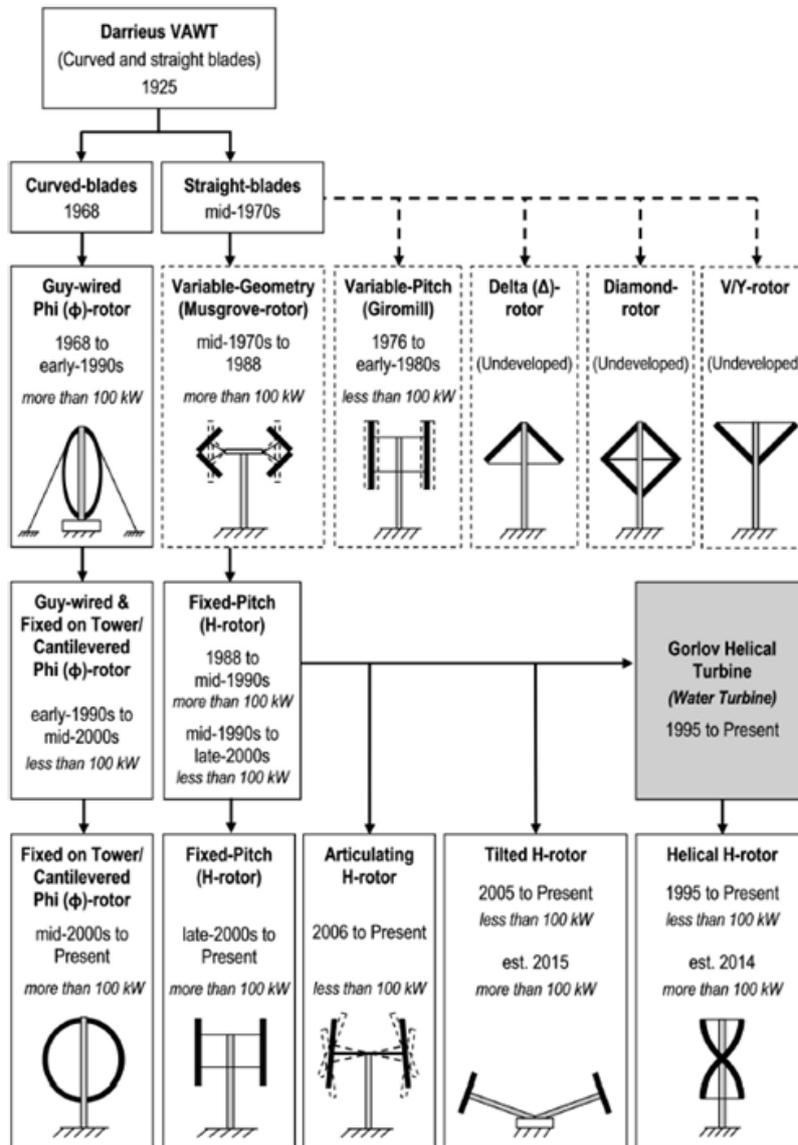
Figure 1.12 Evolution of Darrieus Turbine [18]

A recent movement that the wind energy market has extended its stage to the offshore led

the light to the VAWT. The VAWT has heavy components at the base of the turbine so that the

centre of mass is located at the lower part compared to the HAWT. It is the significant

advantage of the VAWT when deployed as a floating turbine on the offshore environment,

where the harsh loads due to waves and winds are expected. Since the machinery components are placed near the tower-base, operation and maintenance are much more comfortable. Due to the lowly located centre of mass, the tower and substructure can be designed more efficiently, and costs for them could be reduced. Generally wake from VAWT dissipates much quicker than HAWT. It is an excellent advantage when it comes to consisting of a wind farm by reducing the space between turbines and placing much more turbines. More advantages of VAWT against HAWT are well described by Borg et al. [19].

## 1.2.2 PREVIOUS RESEARCH ON VAWT

Figure 1.13 shows a contra-rotating VAWT suggested by Chaichana and Chaitep [20]. It is a Savonius type of the rotor, consisted of 2 rotors rotating opposite direction. According to their work, the contra-rotating concept achieved an average of power coefficient of 14.89%.
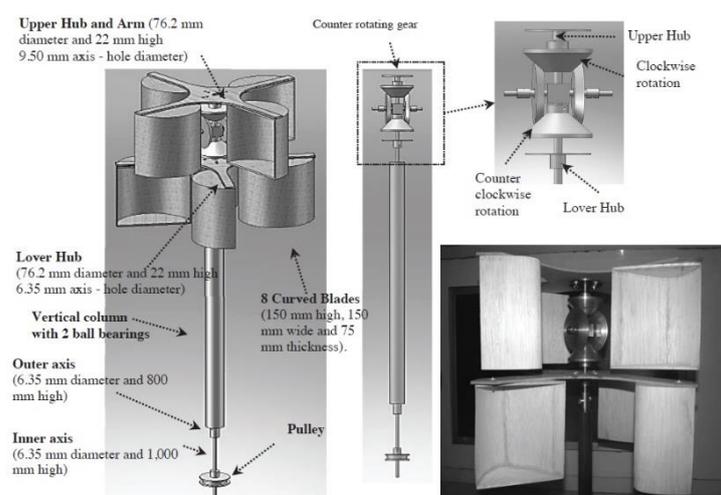


Figure 1.13 Two-shaft Co-axis Contra-rotating Wind Turbine [20]

Didane et al. designed a contra-rotating VAWT and performed the experiments as shown in Figure 1.14 [21]. The study aims to evaluate the effectiveness of adopting the contra-rotating concept to a straight-bladed VAWT with the expectation of an increase in its conversion efficiency. They showed enhanced performance of the wind turbine in power and aerodynamic torque at any given wind speed compared to a conventional single-rotor system of a similar type.



1. Shaft 2. Weight 3. String 4. Pulley 5. Bearing 6. Spring balance 7. Fram
8. Blade 9. Tower 10. Bearing 11. Generator 12. Slip ring 13. PVC 14. Str
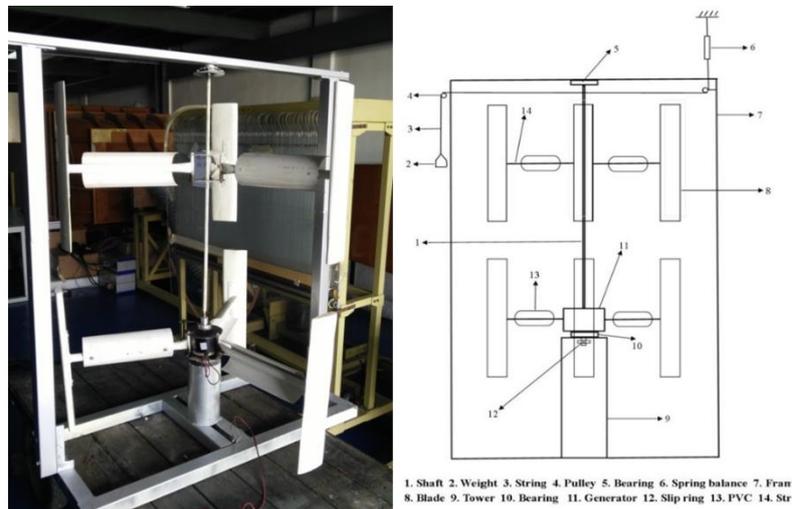
Figure 1.14 Experimental set-up and drawings of a contra-rotating VAWT [21]

A Hybrid VAWT was also suggested and studied by several researchers [22][23][24][25]. It comprised the Savonius turbine and studied a lift-drag hybrid-type of VAWT as Figure 1.15. It consists of the Darrieus-type blades and Savonius-type blades to have advantages of the drag forces as well as the lift forces generated by the wind. As a result, a higher starting torque is achieved, but the power coefficient of this type of VAWT is lower than that of conventional

Darrieus-type VAWT.

Figure 1.15 Hybrid-type VAWT [26]

Since VAWTs have benefits if installed at an offshore site as aforementioned, efforts to apply floating offshore VAWTs have led to studies and projects. Various designs of the rotor of the VAWT have been investigated under the offshore environment with its floating substructure.

Vita et al. proposed and researched a Darrieus-type rotor mounted on a spar buoy rotating platform, known as DeepWind concept, with an expectation of simple construction and transportation and cost reduction potentials [27][28]. The whole system is rotating, and the generator is placed at the bottom of the substructure. Because of a large draft, it could be installed in water depths deeper than 150 m.
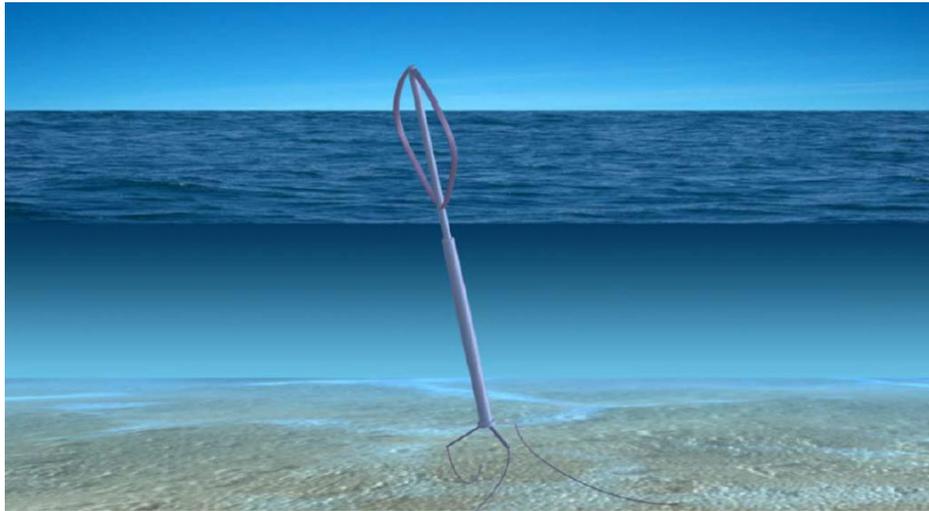
Figure 1.16 DeepWind concept of floating offshore VAWT

NENUPHAR proposed the TWINFLOAT® concept consisting of two 2.5MW VAWT on a semi-submersible substructure (Figure 1.17) [29]. They took advantages of several concepts, suggested to improve the performance of VAWTs such as increasing the swept area, using flap and pitch systems, combined with the counter-rotating effect [31].



Figure 1.17 The TWINFLOAT® concept [32]

SeaTwirl S1, developed by SeaTwirl, is a 30kW VAWT on a spar-type substructure (Figure 1.18) [33]. It is placed at the coast of Lysekil, Sweden on a depth of 35m in 2015. SeaTwirl S2, a full-scale 1MW VAWT, is currently under development (Figure 1.19). Its rotor blade height is approximately 40 m, and optimal operating depth is deeper than 100m [34].



Figure 1.18 SeaTwirl S1 placed at Test Lab Lysekil



Figure 1.19 Concept illustration of the wind farm with multiple SeaTwirl S2

### 1.2.3 FULLY COUPLED SIMULATION CODES OF FLOATING VAWT

Relatively less interest in VAWT had delayed the development of integrated analysis codes for floating offshore VAWT. Along with the increasing attention to VAWT as floating offshore turbine, the necessity of fully coupled time-domain analysis of VAWTs under the offshore environment has made various institutes and researchers developing the appropriate tools.

Wang et al. developed the SIMO-RIFLEX-DMS code and performed the fully coupled non-linear aero-hydro-servo-elastic simulations for floating VAWT [35][36]. They used SIMO and RIFLEX for offshore structures subjected to wave loads. For aerodynamic calculations, the DMSM is used with the Beddoes-Leishman dynamic stall model.

Collu et al. developed FloVAWT code to provide a simplified coupled dynamic design tool [37][38]. They used the DMSM with Gormont-Berg dynamic stall for the aerodynamic calculation. Although the mooring module adopts a quasi-static catenary equations approach and structural and controller dynamics are not considered, it can be used in the preliminary design stages of floating VAWTs.

The OWENS (Offshore Wind Energy Simulation) toolkit was developed by Sandia National Laboratories [39]. It allows users to integrate easily with existing aerodynamic and hydrodynamic codes. Also, it offers flexibility for users to consider arbitrary configuration geometries and loading scenarios.

Madsen et al. implemented a fundamentally different aerodynamic momentum model,

using an actuator cylinder to represent the turbine, with the aero-hydro-servo-elastic code

HAWC2 to conduct the fully coupled time-domain simulations [40]. Its results are accurate

even at high wind turbine loading and are computationally efficient. DeepWind project

investigated their VAWT using this code in their various studies [28][41][42].

Cheng et al. developed and verified SIMO-RIFLEX-AC, which uses the AC model for an

aerodynamic calculation and SIMO-RIFLEX, for a fully coupled aero-hydro-servo-elastic

simulation tool giving highly accurate results [43].

Most of the introduced simulation tools are based on commercial programmes or

unveiled to the public. However, the needs of the integrated analysis codes for floating

offshore VAWT is expected to increase continuously both in academic and industry area. For

this reason, an easy-to-use analysis tool for floating offshore VAWTs needs to develop. It can

also boost interests in VAWTs.

## 1.3 OBJECTIVES

As introduced, the interest in the VAWT has increased along with the growth of the

offshore wind industry due to its advantages under the offshore environment. In the case of

the VAWT, the centre of mass is located lower compared to the HAWT because the

mechanical systems are placed near the tower bottom. Hence, more stable motions are

expected by adopting the VAWT, especially for the floating model. However, the torque of the

VAWT affected to the tower and substructure, causing the yaw moment on the supporting

tower and substructure. Loads continuously acting on the structure requires robust design. Continued platform motions cause the increase in the mooring tension, which means the mooring system should be sturdy. Consequently, the manufacturing and maintenance costs could be raised. Hence, this study suggests a contra-rotating VAWT to mitigate the structural loads and platform motions by the counterbalanced torque produced by the two rotors.

This study was proposed and conducted to achieve the following objectives:

- develop a non-commercial and easy-to-use numerical code for integrated analysis of a floating offshore VAWT based on the FAST structure,

- adapt a contra-rotating VAWT for the use of a floating offshore turbine and evaluate its motion and power by comparison to a conventional VAWT.

The present work proceeded in the order shown in Figure 1.20. In Step 1, the aerodynamic analysis code for VAWT was developed using the structure of AeroDyn v15.03, which is a HAWT aerodynamic analysis code, developed by National Renewable Energy Laboratory (NREL). The aerodynamic analysis code for VAWT was verified by comparing to results from other studies. After finishing Step 1, an integrated analysis code for the whole system of VAWT was developed and verified. The structure of this code was based on that of FAST v8.16.00a-bjj. FAST is developed by the NREL as well. It is a well-known and widely used open-source code for the HAWT aero-hydro-servo-elastic analysis. At this step, the

work from Step 1 was used instead of the aerodynamics of HAWT and combined with the other module of FAST. Once the advanced analysis code was verified for the onshore VAWT, the analysis code was extended by including the hydrodynamic calculation and mooring calculation for a floating offshore VAWT. Finally, at step 3, the developed code was further improved for the contra-rotating VAWT simulation, and the contra-rotating VAWT was evaluated.

Throughout the present study, the reason for using the structures of AeroDyn and FAST is its inheritance advantage and openness. The present work was carried out for the same purpose. All the required changes and modifications in FAST modules were according to the guidelines in NWTC Programmer's Handbook [44].
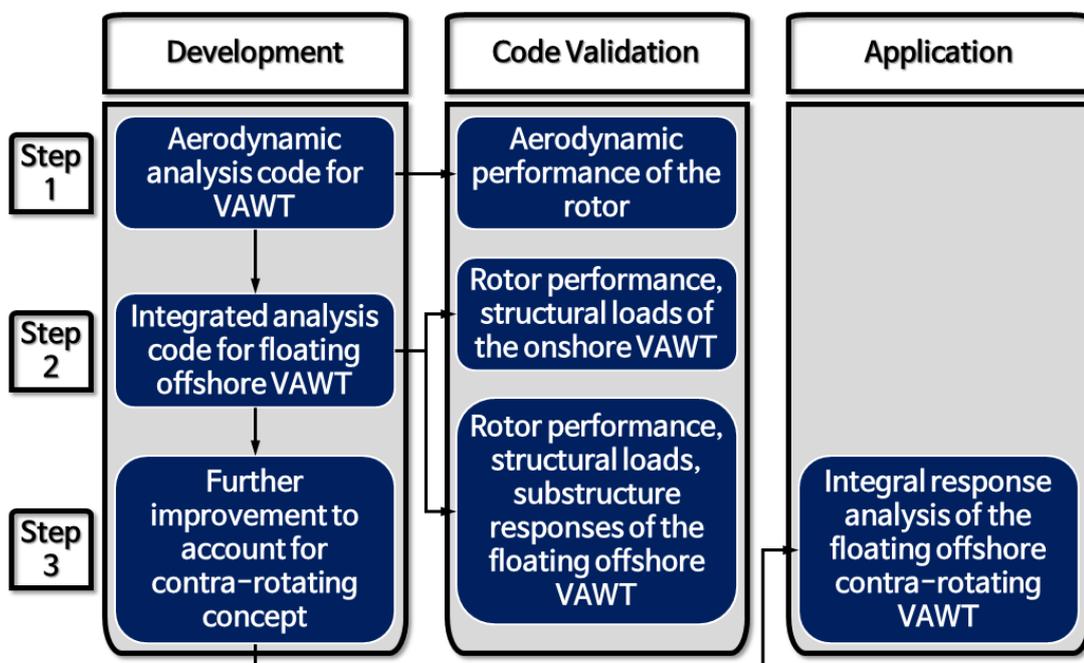


Figure 1.20 Process of the present work

The entire paper is structured, as outlined below.

Chapter 2 presents the aerodynamics of the VAWT and the development of the aerodynamic analysis code for the VAWT using the standalone code of AeroDyn.

Chapter 3 introduces the integrated analysis code of the floating offshore VAWT developed using FAST and its verification.

Chapter 4 shows the contra-rotating VAWT and its analysis results compared to the conventional VAWT.

Chapter 5 concludes this study and suggests future studies.

# Chapter 2

# AERODYNAMICS OF VAWT

**2.1 MOMENTUM MODELS**

Several numerical models such as momentum models, cascade models, vortex models have been developed to analyse the aerodynamic characteristics of the VAWT and used for the performance prediction and design of the VAWT.

Momentum models are based on the conservation of momentum principle, which calculates flow velocity through the turbine by equating the streamwise momentum change rate of air across the turbine to the streamwise aerodynamic forces acting on the blades. The actuator disk theory assumes homogeneous, incompressible and steady-state fluid flow having no frictional drag. Also, the pressure increments or thrust per unit area are assumed to be constant over the disk. The rotational component of the velocity in the slipstream is zero, the velocity is continued through the disk, and it assumes an infinite number of blades [45]. For the VAWT aerodynamics, there are variations of the momentum models as Figure 2.1.
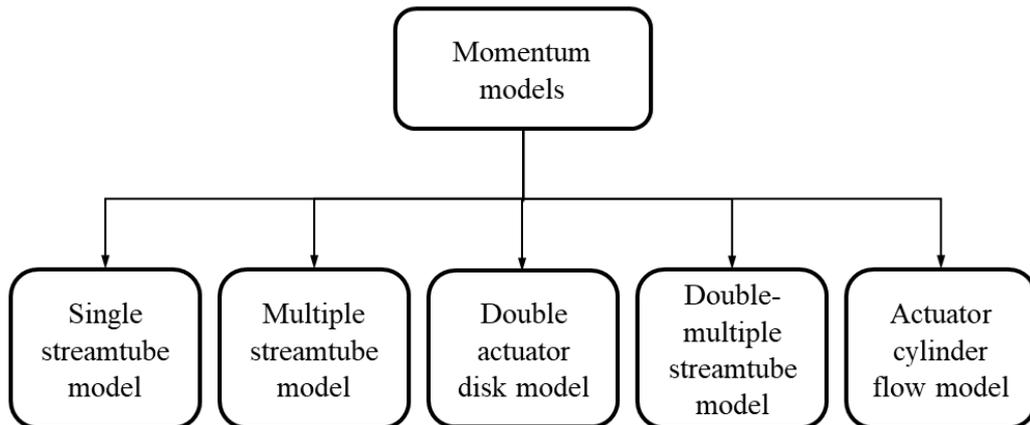
Figure 2.1 Momentum models

Templin firstly proposed a single streamtube model to calculate the aerodynamics of a curved-blade VAWT, based on the approach of the aerodynamics of the propeller or windmill [46]. It considers the entire rotor area of the VAWT as an actuator disk in a single streamtube. It assumes the induced velocity is constant through the disk. Thus, the induced velocity is the same throughout the upwind and downwind parts of the rotor.

A multiple streamtube model was introduced by Wilson and Lissaman [47] and Strickland [48]. This model gives an improved prediction of the wind velocity compared to the single streamtube model by dividing the rotor area into several streamtubes, each of which having its induced velocity, as shown in Figure 2.2. With this model, the different induced velocities perpendicular to the streamwise direction can be considered by dividing the rotor area into multiple streamtubes, each of which has its velocity.
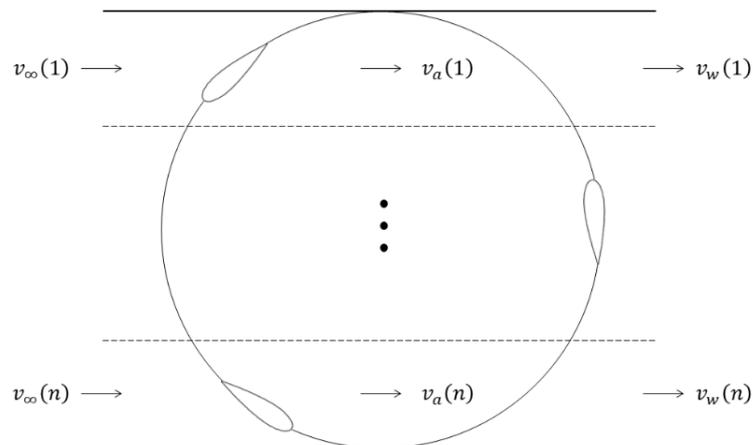
Figure 2.2 Schematic of the multiple streamtube model

The mentioned streamtube models cannot consider the variation in induced velocity between upwind and downwind zones of the rotor. Unlike the case of HAWT, the wind passes twice through the rotor of the VAWT, and the induced velocities on the upwind and downwind zones change. The double actuator disk theory assumes that two actuator disks are placed at the upwind zone and downwind zone as Figure 2.3 [49][50].
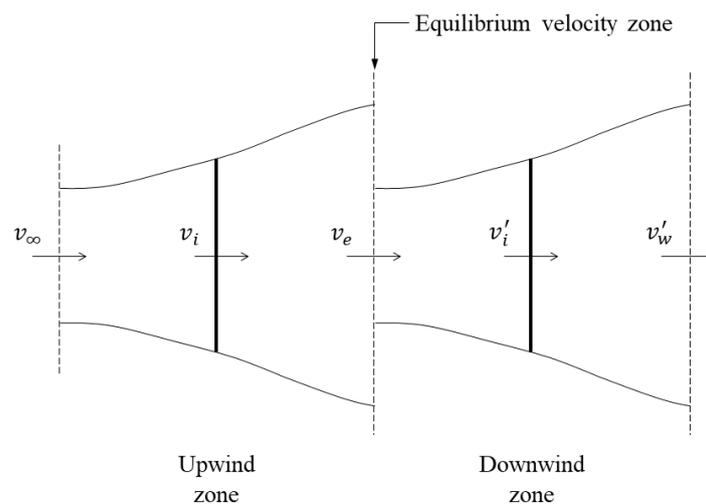


Figure 2.3 Schematic of the double actuator disk theory

Using this theory makes consideration of a distinction between the upwind and downwind zone of the turbine possible. Newman showed, in his study, that the maximum power coefficient for the double disks is about 0.640, which is bigger than the single-disk Betz limit of 0.593 [50].

Paraschivoiu introduced a double multiple streamtube model (DMSM) by dividing multiple streamtubes into the upwind and downwind parts [51]. It uses two constant interference factors calculated by a double iteration. Although the DMSM shows better correlation with the experimental results [52][53], it overpredicts power for a high solidity turbine and has a convergence problem at the higher tip speed ratio. However, the DMSM can be done by a simple calculation process and promises the fast calculation time and efficient computational memory which is advantages for the early step of VAWT design. For this reason, this research used the DMSM for the calculation of the VAWT aerodynamics. The details of the DMSM is presented in the next section.

There is the other momentum model, which is the actuator cylinder flow model. It was proposed by Madsen [54]. It is based on the actuator disk theory by considering an energy balance for the swept surface of a VAWT acting as an actuator cylinder.

## 2.2 DOUBLE MULTIPLE STREAMTUBE MODEL

Paraschivoiu developed the DMSM by combining the multiple streamtube model and the double actuator disk [51]. The DMSM takes the advantages of the multiple streamtube model

and double actuator disk theory so that velocity changes not only in the direction perpendicular to the free stream flow but also between the upwind and downwind zone of the turbine are considered. As can be seen in Figure 2.4, the DMSM divides the rotor area into the multiple streamtubes, and each streamtube has two actuator disks placed on the path where the blade passes at the upwind and downwind zone.
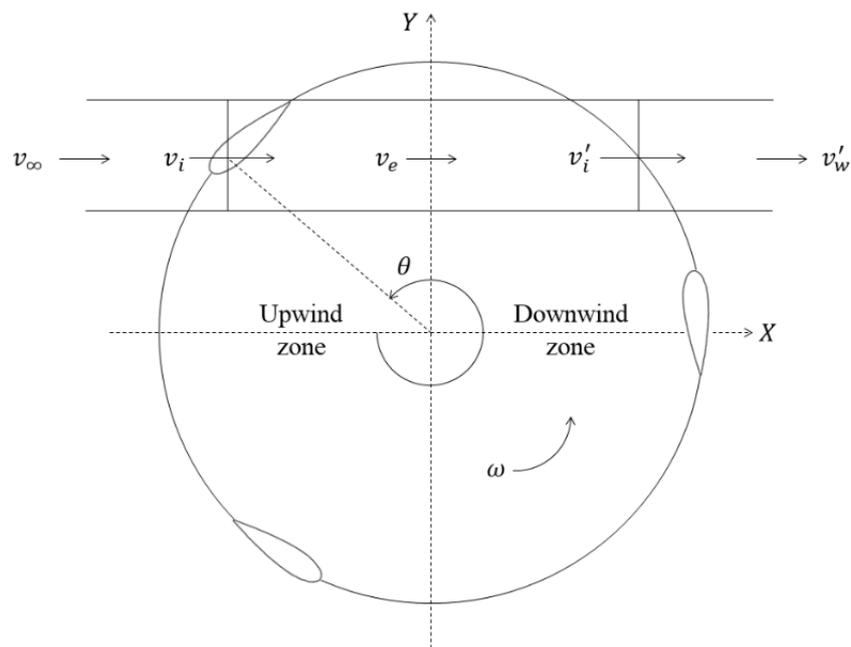


Figure 2.4 Schematic of the DMSM

The air flowing with a freestream velocity, $v_\infty$, passes through the rotor disk of the upwind zone with an induced velocity, $v_i$, which is slower than $v_\infty$ due to the resistance of the rotor disk. An interference factor, $u_1$, represents the change rate of the flow velocity at the upwind zone. It is calculated by equation (2.1).

$$u_1 = \frac{v_i}{v_\infty} \tag{2.1}$$

The air passing through the upwind zone flows with the equilibrium velocity ($v_e = (2u_1 - 1)v_\infty$) to the downwind zone and passes the downwind zone with the velocity $v'_i$. The interference factor at the downwind zone ($u_2$) is obtained by equation (2.2).

$$u_2 = \frac{v_i{}'}{v_e} \tag{2.2}$$

After passing through the rotor, the air flows with the wake velocity ($v_w = (2u_2 - 1)v_e$). Local relative velocity ($W$) and angle of attack ($\alpha$) are calculated by equation (2.3) and (2.4).
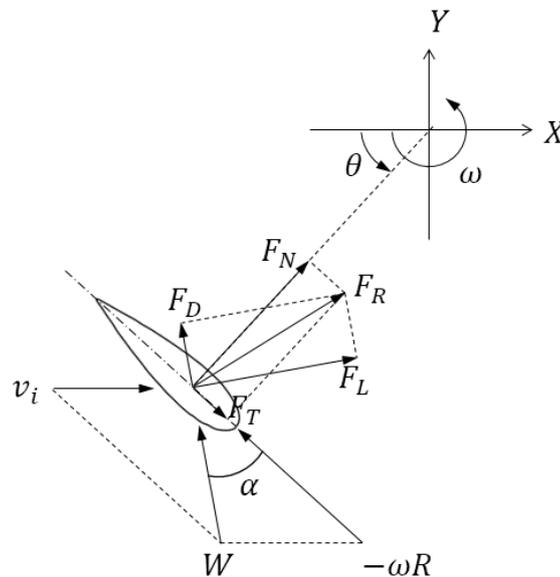


Figure 2.5 Velocities and forces on blade element

$$W^2 = v_i^2[(\lambda_l - \sin\theta)^2 + \cos^2\theta] \tag{2.3}$$

$$\alpha = \sin^{-1}\left[\frac{\cos\theta}{\sqrt{(\lambda_l - \sin\theta)^2 + \cos^2\theta}}\right] = \sin^{-1}\left[\frac{v_i \cos\theta}{W}\right] \tag{2.4}$$

where $\lambda_l$ is local tip speed ratio, dividing $\omega R$ by $v_i$, and $R$ is the rotor radius.

The lift and drag force coefficients $(C_L, C_D)$ are estimated by Reynolds number ($Re = Wc/v_\infty$) and an angle of attack, and the normal and tangential force coefficients $(C_N, C_T)$ are calculated by equation (2.5) and (2.6), respectively.

$$C_N = C_L \cos\alpha + C_D \sin\alpha \tag{2.5}$$

$$C_T = C_L \sin\alpha - C_D \cos\alpha \tag{2.6}$$

As a result, the upwind interference factor can be presented as equation (2.7).

$$u_1 = \pi/(f_{up} + \pi) \tag{2.7}$$

where

$$f_{up} = \frac{Nc}{8\pi R|\cos\theta|}\left(\frac{W}{v_i}\right)^2 \int\limits_{-\pi/2}^{\pi/2} (C_N \cos\theta + C_T \sin\theta)d\theta \tag{2.8}$$

In equation (2.8), $N$ is the number of blades, $c$ is the chord length.

The normal force ($F_N$) and tangential force ($F_T$) of the blade are calculated by the equation (2.9) and (2.10), respectfully.

$$F_N = \frac{1}{2}\rho c W^2 H \int_{-1}^{1} C_N d\zeta \tag{2.9}$$

$$F_T = \frac{1}{2}\rho c W^2 H \int_{-1}^{1} C_T d\zeta \tag{2.10}$$

where $H$ is the half-height of the rotor, $z$ is the local height of the streamtube, $\zeta = z/H$, and $\rho$ is air density.

The thrust force ($F_X$) and side force ($F_Y$) of each blade at azimuth angle $\theta$ are calculated as follows.

$$F_X = F_N \cos\theta + F_T \sin\theta \tag{2.11}$$

$$F_Y = F_N \sin\theta - F_T \cos\theta \tag{2.12}$$

The torque on a whole blade ($T_{UP}$) is obtained using equation (2.13) as a function of the blade position (azimuth angle, $\theta$). The average half-cycle of the rotor torque produced by the half of $N$ blades ($\bar{T}_{UP}$) is given by equation (2.14).

$$T_{UP}(\theta) = \frac{1}{2}\rho cRH \int_{-1}^{1} C_T W^2 d\zeta \tag{2.13}$$

$$\bar{T}_{UP} = \frac{N}{2\pi} \int_{-\pi/2}^{\pi/2} T_{UP}(\theta) d\theta \tag{2.14}$$

The average half-torque coefficient by the upwind zone of the rotor is $\bar{C}_{Q1}$.

$$\bar{C}_{Q1} = \bar{T}_{UP} / \left(\frac{1}{2}\rho v_\infty^2 RS\right) \tag{2.15}$$

where $S$ is the rotor area, which is $2RH$ for the straight-bladed VAWT.

Then the power coefficient for the upwind zone of the rotor ($\bar{C}_{P1}$) is expressed by equation (2.16).

$$\bar{C}_{P1} = (R\omega/v_\infty)\bar{C}_{Q1} \tag{2.16}$$

For the downwind half of the rotor, $\bar{C}_{Q2}$ and $\bar{C}_{P2}$ can be obtained by the same calculation procedure as the upwind half of the rotor.

At the blade tips of the straight-bladed rotor, velocity could be expressed by two components: one is the spanwise component along the blade's length, and another is the downwash component in the plane of the blade aerofoil, perpendicular to the local relative direction of the wind. The spanwise component of the velocity changes along the blade's

entire length. The air passing through the rotor flows toward the blade tips and the streamtubes passing near the blade tips consequently transfer less momentum to the aerofoil than those passing at the equator. As a result, the efficiency at the blade tips decreases compared the rest part of the blade. To consider this effect, Willmer modified a Prandtl model developed for screw propellers [55][56]. The downwash component affects the angle of attack and causes changes in the lift and drag force coefficients., Prandtl's finite-wing theory is used to consider the downwash component of the induced velocity.

Willmer introduced the modified version of the Prandtl method to include the effects of the spanwise component. Consequently, the relative velocity and the angle of attack are adjusted as equation (2.17) and (2.18).

$$W^2 = u_i^2[(\lambda_l - \sin\theta)^2 + F^2\cos^2\theta] \tag{2.17}$$

$$\alpha = \sin^{-1}\frac{Fv_i\cos\theta}{W} \tag{2.18}$$

In these equations, $F$ is calculated by Equation (2.19).

$$F = \frac{\cos^{-1}\left(e^{-\pi h/s}\right)}{\cos^{-1}\left(e^{-\pi H/s}\right)} \tag{2.19}$$

$s = \frac{\pi v}{N\omega}$, $h = H - |z|$, $v$ is the equilibrium velocity at the upwind zone and the wake velocity at the downwind zone.

The lift and drag force coefficients for the finite blade length ($C_{Lf}, C_{Df}$) are calculated by equation (2.20) and (2.21).

$$C_{Lf} = \frac{C_L}{1 + m/(\pi/AR)} \tag{2.20}$$

$$C_{Df} = C_D + C_{Di} \tag{2.21}$$

where $AR = H/c$. $m$ is expressed as equation (2.22), $t$ is the thickness of aerofoil.

$$m = 1.8\pi(1 + 0.8t/c) \tag{2.22}$$

In equation (2.21), $C_{Di}$ is calculated using $C_{Lf}$ as equation (2.23).

$$C_{Di} = C_{Lf}^2/(\pi/AR) \tag{2.23}$$

## 2.3 CODE DEVELOPMENT

### 2.3.1 AERODYN (STANDALONE) & QBLADE

AeroDyn, which was developed by the NREL, is a Fortran-based aerodynamic analysis code [57]. It is used for calculating the aerodynamics of HAWT, based on Blade Element Method (BEM). It is possible to use as a standalone code to compute wind turbine

aerodynamic response uncoupled from FAST or be coupled into the FAST version 8 multi-physics engineering tool. In the present work, the aerodynamic analysis code for VAWT was developed using the standalone code of AeroDyn.

One of the VAWT aerodynamic calculation codes using DMSM is QBlade, developed by TU Berlin [58]. It is an open-source code for the calculation of aerodynamic characteristics of both the horizontal- and vertical-axis wind turbine rotor. It is easily used because of a graphical user interface (GUI) as can be seen in Figure 2.6. The results from Qblade has been verified by showing a good agreement with the experimental results on Sandia 17 m VAWT. The present study used the results from QBlade as one of the references to validate the results from the developed aerodynamic analysis code.
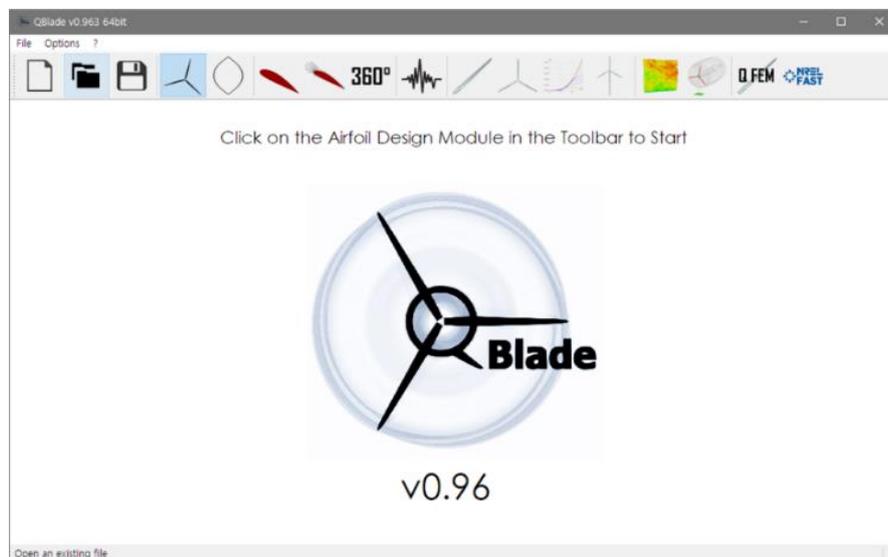


Figure 2.6 Qblade GUI

## 2.3.2 DEVELOPMENT USING DMSM

This study developed the aerodynamic analysis code using AeroDyn ver. 15.03.00 by adjusting appropriately for the VAWT rotor aerodynamics. Since the rotor blades in the downwind zone are behind the tower, the tower influence on wind needs to be considered, but this study neglected the tower effect for simplicity.

To develop the aerodynamic code for VAWT using AeroDyn, some of input file parameters, related to the geometrical layout and mechanical properties, are unnecessary or need to be suitably adjusted for the VAWT. The present study assumed a hub of the VAWT as a point without volume, so a hub radius does not act in the developed code. The input parameters of the turbine are described in Figure 2.7.
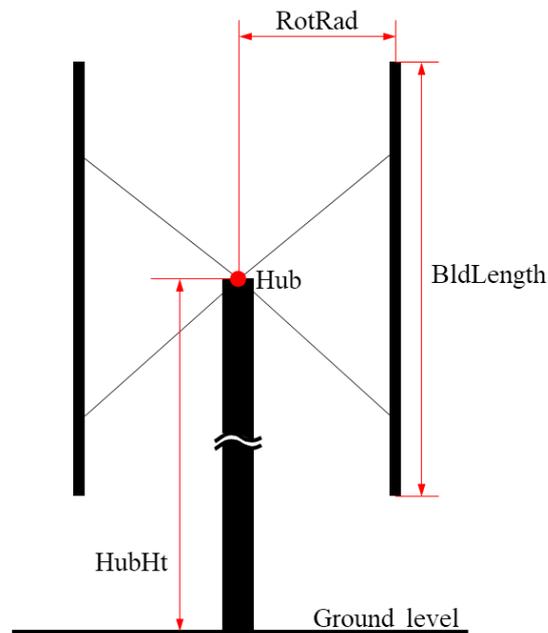


Figure 2.7 Input parameters of the turbine

'RotRad' specifies the radius to the origin of the blade reference point to the centre-of-rotation in the horizontal plane. In the case of the straight-bladed (H-type) VAWT, no matter where the blade reference point is located, 'RotRad' is constant. There is no yaw control in VAWT systems, so 'Yaw' parameter of analysis setting is removed as well. The other input file parameters are maintained, but, depending on their role in the calculation, could not be used in the code.

In this aerodynamic analysis code for VAWT, the geometric layout is simplified having blades and hub. The initial position and orientation of the hub and each element of the blades are calculated as equations (2.24) – (2.29). The wind is assumed to flow along the *X*-axis. The rotor rotates in a counter-clockwise direction as Figure 2.8. Hub reference orientation ($x_{refHub}$, $y_{refHub}$, $z_{refHub}$) is fixed at the centre of the rotor area.
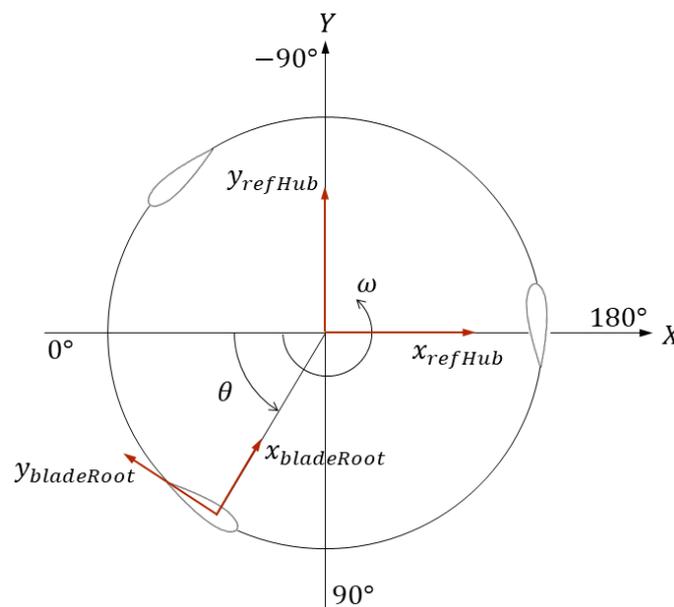


Figure 2.8 Hub and blade orientations

Hub orientation ($\boldsymbol{x}_{Hub}$, $\boldsymbol{y}_{Hub}$, $\boldsymbol{z}_{Hub}$) is positioned as equation (2.24) and initially the same as hub reference orientation as equation (2.25).

$$\boldsymbol{Hub} = \begin{bmatrix} 0 & 0 & HubHt \end{bmatrix} \tag{2.24}$$

$$\begin{bmatrix} \boldsymbol{x}_{hub} \\ \boldsymbol{y}_{hub} \\ \boldsymbol{z}_{hub} \end{bmatrix} = \begin{bmatrix} \boldsymbol{x}_{refHub} \\ \boldsymbol{y}_{refHub} \\ \boldsymbol{z}_{refHub} \end{bmatrix} \tag{2.25}$$

Each blade is equally azimuthally spaced depending on the number of blades ('*NumBlade*') about hub as equation (2.26).

$$\begin{bmatrix} \boldsymbol{x}_{bldRoot} \\ \boldsymbol{y}_{bldRoot} \\ \boldsymbol{z}_{bldRoot} \end{bmatrix} = RotationMatrix \begin{bmatrix} \boldsymbol{x}_{hub} \\ \boldsymbol{y}_{hub} \\ \boldsymbol{z}_{hub} \end{bmatrix} \tag{2.26}$$

where $RotationMatrix = R(\vartheta_z)_1 * R(\vartheta_y)_2 * R(\vartheta_x)_3$ and $\boldsymbol{\vartheta} = \begin{bmatrix} 0.0 & 0.0 & (k-1) * 2\pi/NumBlade \end{bmatrix}$. Blade root position is calculated as equation (2.27), and based on the blade root position, the positions of the other blade elements are calculated.

$$\begin{bmatrix} 0.0 & 0.0 & -BldLength/2 \end{bmatrix} + RotRad * \boldsymbol{x}_{bldRoot} + \boldsymbol{Hub} \tag{2.27}$$

The azimuth angle of each blade is calculated as equation (2.28).

$$\theta = \operatorname{atan} \frac{\boldsymbol{y}_{bldRoot} \cdot \boldsymbol{y}_{refHub}}{\boldsymbol{x}_{bldRoot} \cdot \boldsymbol{x}_{refHub}} \tag{2.28}$$

From the initial position and orientation, hub and blades rotate about z-axis as depicted in Figure 2.8. At every time step, the instantaneous hub orientation, rotating with rotational speed ('*RotSpeed*', $\omega$), is calculated as equation (2.29), and the instantaneous orientations, position and translation velocities are calculated based on the hub orientation.

$$\begin{bmatrix} \boldsymbol{x}_{hub} \\ \boldsymbol{y}_{hub} \\ \boldsymbol{z}_{hub} \end{bmatrix} = RotationMatrix \begin{bmatrix} \boldsymbol{x}_{refHub} \\ \boldsymbol{y}_{refHub} \\ \boldsymbol{z}_{refHub} \end{bmatrix} \tag{2.29}$$

where $RotationMatrix = R(\vartheta_z)_1 * R(\vartheta_y)_2 * R(\vartheta_x)_3$ and $\boldsymbol{\vartheta} = [0.0 \quad 0.0 \quad time *$ $RotSpeed]$.

A whole rotor revolution must be computed to evaluate the instantaneous loads on the rotor by DMSM. As defined in Figure 2.8, the upwind zone is from -90 to 90 degrees, and the downwind zone is from 90 to 270 (=-90) degrees. The accuracy of the DMSM depends on the number of streamtubes. Since a whole rotor revolution needs to be calculated in every time step, the developed code divides the rotor area into 36 streamtubes to increase the time and memory efficiencies, and the values at the instantaneous blade position are interpolated.

The overall process of the aerodynamic calculation is like that of the BEM calculation for the HAWT, as can be seen in Figure 2.9. Iteration of Equations (2.1)– (2.8) for upwind zone

stops when the upwind interference factor converges. The equilibrium wind velocity is calculated using the upwind interference factor and used for the induced velocity of the downwind zone. In the downwind zone, the downwind interference factor converges, the iteration stops, and, finally, the rotor torque and power are obtained.
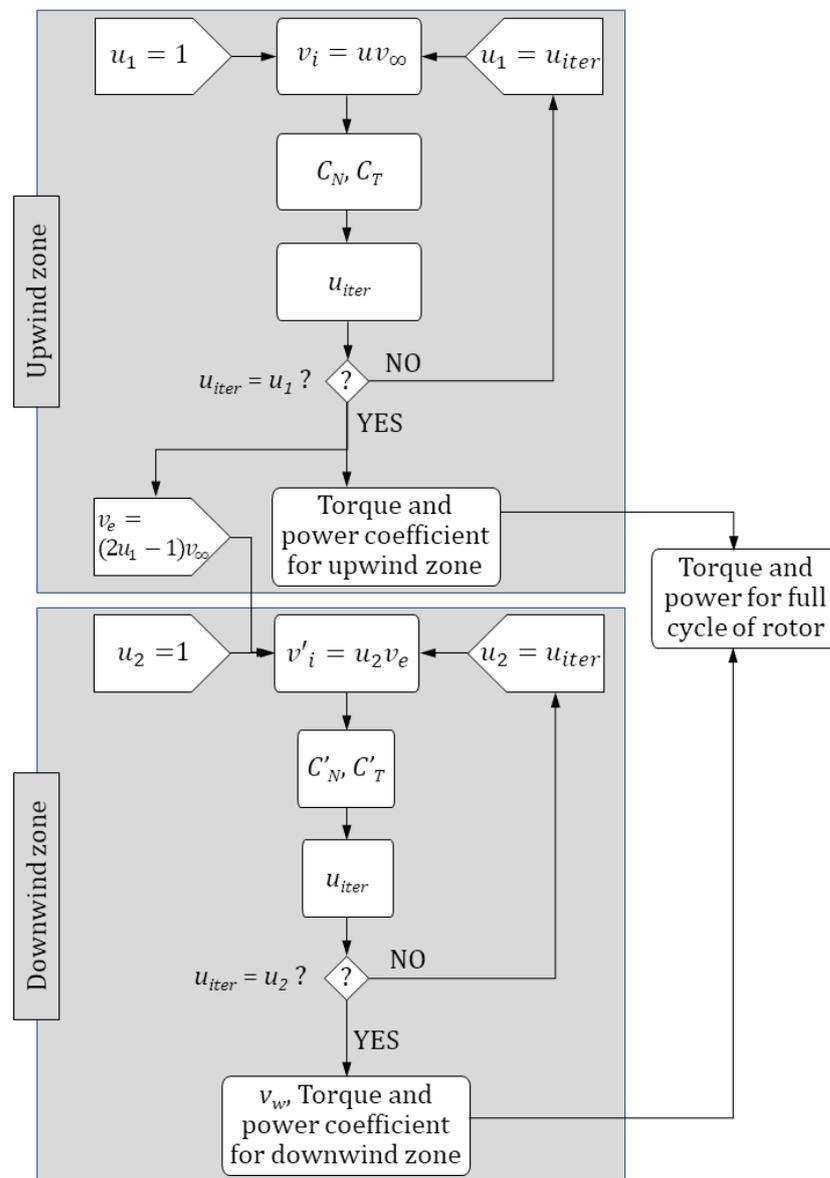
Figure 2.9 Iterative procedure for upwind and downwind part of VAWT

**2.4 VALIDATION**

In the following section, the results from the in-house code were validated by comparing with the results from Qblade, CFD analysis and the experiment from the literature.

2.4.1 VALIDATION USING QBLADE RESULTS

Firstly, power coefficient, angle of attack and rotor torque of the developed analysis code were compared to those of QBlade. Figure 2.10 and Table 2.1 depict a simulation model, which is used for the study of Castelli et al. [59].
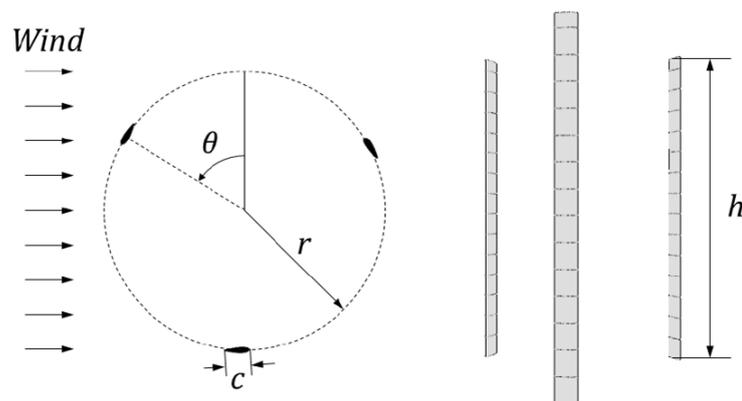


Figure 2.10 Geometrical layout of the rotor for comparison to QBlade

Table 2.1 Specifications of the rotor for comparison to QBlade

| Item | Unit | Value |
|---|---|---|
| Rotor radius (r) | m | 0.515 |
| Number of rotor blades | - | 3 |
| Blade length (h) | m | 1.456 |
| Blade profile | - | NACA 0021 |
| Chord length (c) | m | 0.0858 |

Figure 2.11 shows the power coefficient curves according to the tip speed ratios (TSR) of 1.1 to 3.0 with an interval of about 0.1 and the pitch angle of -4 to 4 deg with an interval of 2 deg. Table 2.2 is the maximum error and the average of the absolute values of the errors compared to the QBlade results according to the blade pitch angle. In the case of the blade pitch angle of -4 deg, the maximum percentage is similar to the other results except for TSR of 3.0, showing the maximum value of the maximum percentage of 1.424. Overall, the results from the developed code agree well with the QBlade's results.
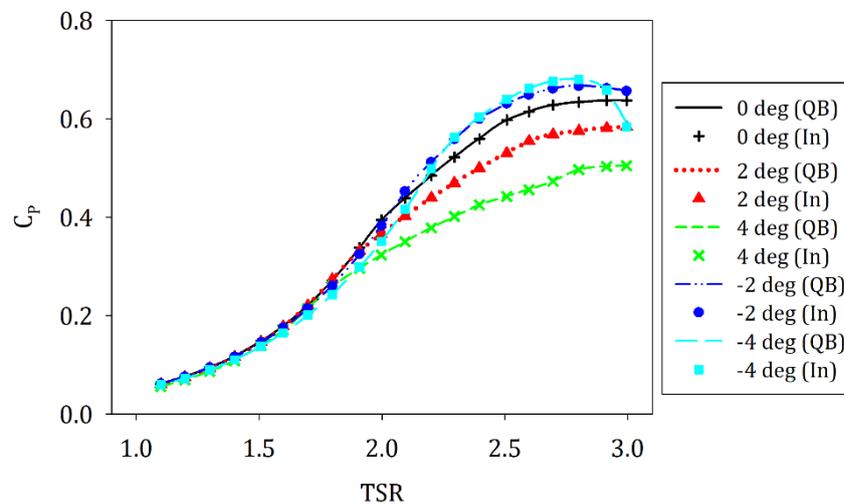


Figure 2.11 Power coefficient curves as a function of TSR according to change in the blade pitch angle (In: developed code, QB: QBlade)

Table 2.2 Differences between power coefficients obtained from the developed code and

QBlade

| Blade pitch [deg] | Differences [%] | |
| --- | --- | --- |
| | Max. | Mean |
| -4 | 1.424 | 0.109 |
| -2 | 0.206 | 0.093 |
| 0 | 0.218 | 0.077 |
| 2 | 0.208 | 0.074 |
| 4 | 0.227 | 0.081 |

Figure 2.12 is the calculated angle of attack when the blade pitch angle is 0 deg. In order

to see the difference of the results by the change of TSR ($\lambda$), four TSR were chosen, including

the maximum and minimum TSR of the calculation of the power coefficient curves. The

angle of attack is a function of inflow velocity and direction, azimuth angle of a blade and a

blade pitch angle. When the blade is at the downwind zone, the angle of attack becomes

smaller than when it is located on the upwind zone because the air at a lower speed flows into

the blade. As shown in Figure 2.12, the magnitude of the angle of attack on the downwind

zone is smaller since DMSM can reflect this phenomenon. Table 2.3 shows the maximum

error and the average of the absolute values of the errors compared to the QBlade results. For

all TSRs, the two values are less than 0.1 %, indicating that the two results are almost

identical.
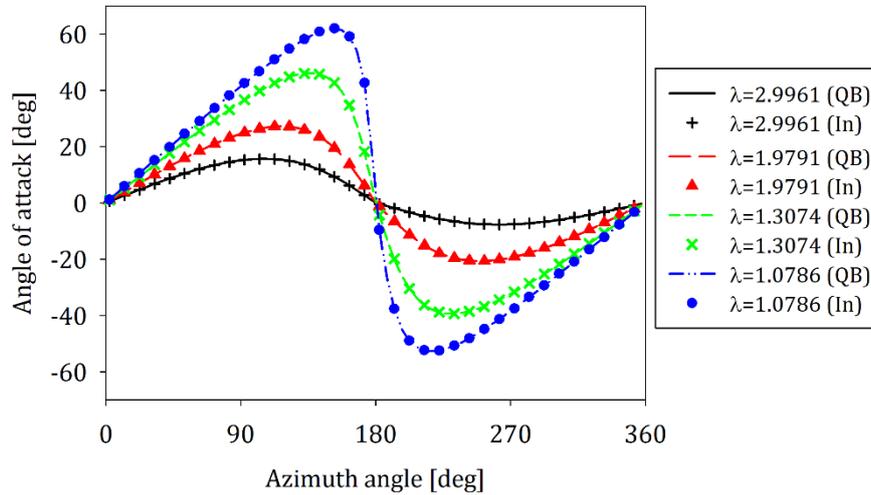
Figure 2.12 Angle of attack as a function of the azimuth angle (In: developed code, QB: QBlade)

Table 2.3 Differences between the angle of attack calculated from the developed code and QBlade

| Tip speed ratio | Differences [%] | |
| --- | --- | --- |
| | Max. | Mean |
| 1.0786 | 0.014 | 0.002 |
| 1.3074 | 0.007 | 0.002 |
| 1.9791 | 0.057 | 0.021 |
| 2.9961 | 0.100 | 0.051 |

Figure 2.13 is the rotor torque curves calculated by the developed analysis code (In) and QBlade (QB). Table 2.4 is the maximum value of the error between the calculation results of the two codes and the average of the absolute values of the errors.
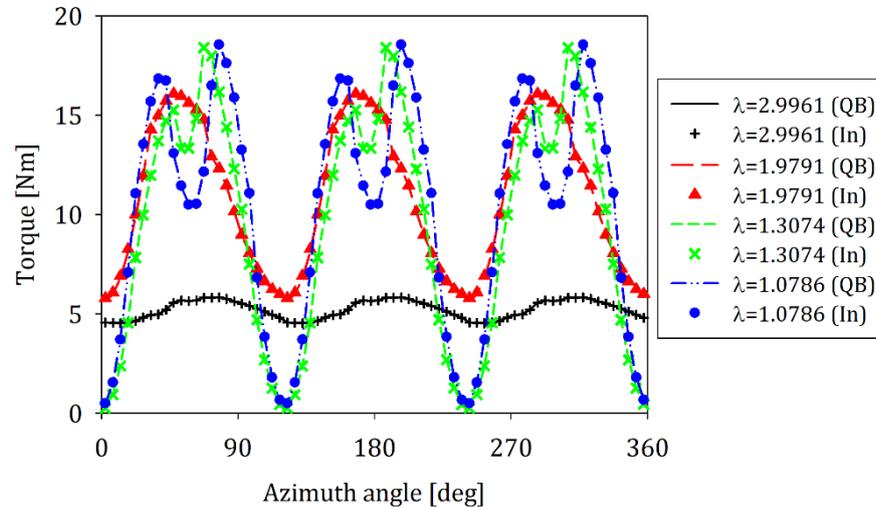
Figure 2.13 Rotor torque curves as a function of the azimuth angle according to TSR (In: developed code, QB: QBlade)

Table 2.4 Differences between the rotor torque results calculated from the developed code and QBlade

| Tip speed ratio | Differences [%] | |
| --- | --- | --- |
| | Max. | Mean |
| 1.0786 | 0.448 | 0.095 |
| 1.3074 | 1.261 | 0.141 |
| 1.9791 | 2.014 | 0.424 |
| 2.9961 | 0.180 | 0.116 |

The pitch angle of the rotor blade is 0 degrees, and the results of the same four TSRs are compared to see the difference according to the TSR. In Figure 8, when the TSR is high (2.9961, 1.9791), the rotor torque has three peaks during one revolution since the torque at upwind zone is dominant. On the other hand, when the TSR is low (1.3074, 1.0786), the

torques at the upwind zone and the downwind zone are similar, so that there are two peaks per blade during one revolution, resulting in a total of six peaks. In general, the results of the developed analysis code and the QBlade show a close agreement. The maximum error in the specific TSR was about 1–2 %, but it is not a significant influence on the result. Except for the point where the maximum error occurred, the error between the results of the two codes is very similar, less than 1 %.

### 2.4.2 VALIDATION USING THE EXPERIMENTAL AND CFD RESULTS

The developed aerodynamic analysis code was further assessed by comparing the results to the experimental results and CFD analysis results. A small-scaled H-type VAWT from Lei et al. [60] was used for the validation. Figure 2.14 shows the configuration of the VAWT, and the specifications are listed in Table 2.5.
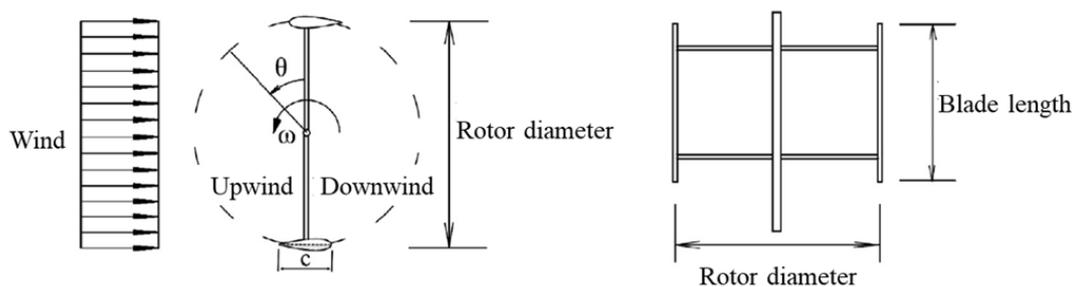


Figure 2.14 Rotor configuration for comparison with CFD and experimental results [60]

Table 2.5 Specifications of the rotor for comparison with CFD and experimental results

| Item | Unit | Value |
|---|---|---|
| Rotor diameter | m | 2 |
| Number of rotor blades | - | 2 |
| Blade length | m | 1.2 |
| Blade profile | - | NACA 0021 |
| Chord length | m | 0.265 |
| Pitch angle | deg | 4 |

CFD simulations were carried out by StarCCM+ using two turbulence models; one is the SST (Shear Stress Transport) k-ω model and another is the IDDES (Improved Delayed Detached Eddy Simulation) model. Those two models are known to predict relatively accurate steady-state simulations [61]. Experiment results are from [60].

Power coefficients and rotor torques are validated with the experiment results and CFD simulation results. Figure 2.15 is the power coefficient curves as a function of TSR. For calculations, wind speed is 8 m/s, and rotor speed is changed. When the CFD results are compared to the experimental results, it shows a good agreement, meaning that the CFD results can be used as a reference to verify the DMSM results.

By comparing with the CFD results, DMSM results tend to follow the overall trend, especially when the tip loss effect is considered. For this reason, the tip loss effect should be considered to obtain more realistic results. However, as TSR is higher, which means the rotor speed is faster, the DMSM overpredicts the power coefficients. After TSR of 2.3, the power coefficients from the experiment and the CFD calculations decrease, but those from the

DMSM do not follow the trend. To verify the DMSM results in detail, Table 2.6 lists the

power coefficients from CFD simulation using two different models and DMSM calculation

and the errors of the DMSM results compared to the CFD results using IDDES model.
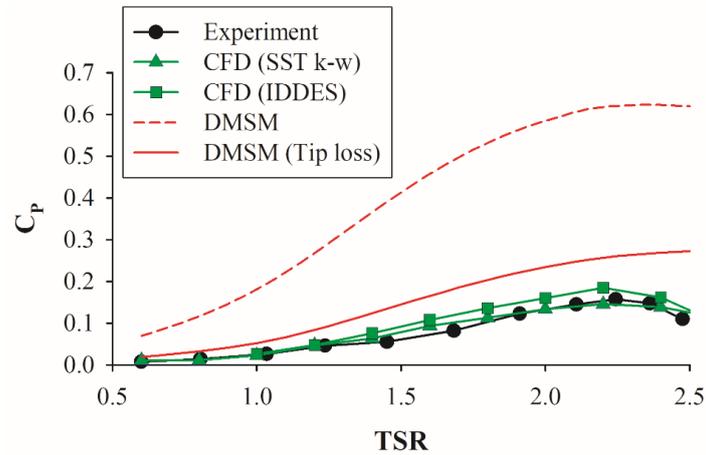


Figure 2.15 Power coefficient curves as a function of TSR

Table 2.6 Power coefficient results from the developed aerodynamic code and CFD analysis

| TSR | $C_P$ | | Differences |
|---|---|---|---|
| | CFD (IDDES) | DMSM (Tip loss) | |
| 0.6 | 0.0080 | 0.0194 | 0.0114 |
| 0.8 | 0.0166 | 0.0322 | 0.0156 |
| 1 | 0.0260 | 0.0522 | 0.0262 |
| 1.2 | 0.0475 | 0.0837 | 0.0362 |
| 1.4 | 0.0761 | 0.1236 | 0.0475 |
| 1.6 | 0.1079 | 0.1654 | 0.0575 |
| 1.8 | 0.1360 | 0.2034 | 0.0674 |
| 2 | 0.1599 | 0.2342 | 0.0743 |
| 2.2 | 0.1847 | 0.2565 | 0.0718 |
| 2.4 | 0.1616 | 0.2684 | 0.1068 |
| 2.6 | 0.1005 | 0.2785 | 0.1780 |

Figure 2.16 shows rotor torque curves of two TSRs as a function of an azimuth angle and

the flow separation at certain azimuth angles computed by CFD.



(a)  TSR = 1.032



(b)  TSR = 2.245
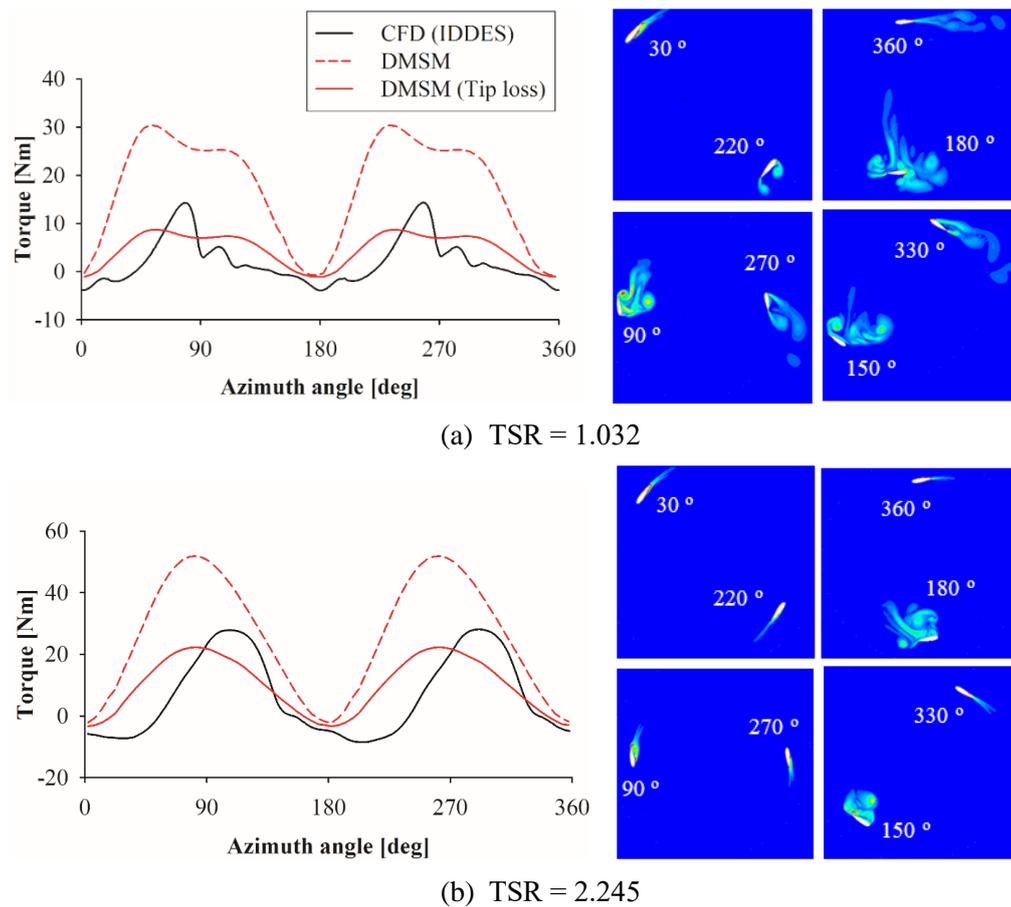
Figure 2.16 Rotor torque curves and flow separation at the given TSR as a function of the
azimuth angle

Because the DMSM gave significantly different power coefficient trends before the TSR of

1.2 and after the TSR of 2.3, the results with TSR = 1.032 and TSR = 2.245 are selected to

validate. As expected, the DMSM with the tip loss effect gives closer magnitudes to CFD

results in both TSRs. In the case of the lower TSR, the DMSM gives relatively moderate

torque compared to the CFD results. In this case, the variation in torque is severe due to the strong flow separations. The differences between DMSM and CFD predictions might arise from these secondary flow effects. When the flow separation occurs strongly, resulting in a stall, the DMSM under- or overpredicts the torque since it does not account for the secondary flow effects. In the higher TSR, the torque curves, predicted by both DMSM and CFD, smoothly ups and downs, showing a similar trend. Although there are some differences in the peak position, overall the DMSM gives consistent results compared to the CFD, with the simpler computational time.

## 2.5 CONCLUSIONS

In this chapter, the development and verification of the aerodynamic analysis code for VAWT were presented. The DMSM is one of the momentum models to analyse the aerodynamic characteristics of vertical-axis rotors. DMSM places the multiple streamtubes in the rotor area, and each streamtube is divided into two flow parts–upwind and downwind zone. It leads to more accurate results by introducing the different induced velocities in both zones. Despite its disadvantages in high solidity rotor and higher tip speed ratio, the DMSM has been used broadly in many studies due to the computational efficiency. For this reason, this study adopted the DMSM for development of the aerodynamic analysis code.

The structure of the developed code was based on AeroDyn ver. 15.00.03, which is a Fortran-based open-source code made by NREL. AeroDyn is for the analysis of the

horizontal-axis rotor, so the relevant geometrical layout, mechanical properties and aerodynamic calculations were modified. The iteration of the whole rotor revolution proceeded to obtain the instantaneous loads on the blade. Prandtl method and Willmer's modification were used in the calculation in order to include the tip loss effect.

The developed code was validated using small-scale H-type VAWTs. The results calculated by the developed code agreed well with the QBlade's results, which is also developed using DMSM. Compared to the CFD, the developed code gave relatively higher power coefficient curves, but its trend is close to the CFD results up to TSR of 2.3. In the case of the rotor torque curves of lower and higher TSR, the developed code gave similar magnitudes and trends.

The present developed aerodynamic analysis code gives close tendency and magnitude compared to the CFD although it cannot capture the complex aerodynamic phenomenon. Since its calculation process is much simpler and the computational time is much faster, the developed code can be used for the preliminary design of the VAWT. It does not yet include the secondary flow effects in the calculation, so it is left for future work.

# Chapter 3

# INTEGRATED ANALYSIS FOR

# FLOATING VAWT

## 3.1 GENERAL

The present work developed the integrated analysis code for the floating VAWT and validated the developed code. The developed code is based on the structures of FAST v8.16.00a-bjj. As aforementioned, FAST is the aero-hydro-servo-elastic analysis code for the fixed and floating HAWT. FAST contains the modules and components listed in Table 3.1. The modules interfaces, as shown in Figure 3.1.

There are assumptions as listed below to simplify the problem:

- Supporting arms, which connects the blades and the tower are not considered at all calculations,

- The tower and blades are assumed as a rigid body,

- The tower is rigidly connected to the substructure,

- The substructure is considered as a rigid body, and

- The geometry of the other mechanical systems is not included in the calculations.

Table 3.1 Modules and components in FAST v8.16.00a-bjj

| Function | Component | Version |
|---|---|---|
| | FAST | v8.16.00a-bjj |
| Structure dynamics | ElastoDyn | v1.04.00a-bjj |
| | BeamDyn | v1.01.04 |
| Aerodynamics | AeroDyn | v15.03.00 |
| | AeroDyn v14 | v14.05.01a-bjj |
| Wind loads | InflowWind | v3.03.00 |
| Control dynamics | ServoDyn | v1.06.00a-bjj |
| Part of ServoDyn | TMD | v1.02.01-sp |
| Loads in marine | HydroDyn | v2.05.01 |
| Structural dynamics for multi-member substructures | SubDyn | v1.03.00 |
| Mooring dynamics | MAP++ | 1.20.10 |
| | FEAMooring | v1.02.01 |
| | MoorDyn | v1.01.02F |
| | OrcaFlex Interface | v1.01.02 |
| Surface ice loads | IceFloe | v1.01.01 |
| | IceDyn | v1.02.01 |
| | NWTC Subroutine Library | v2.09.00 |
| | FAST Registry | v3.02.00 |
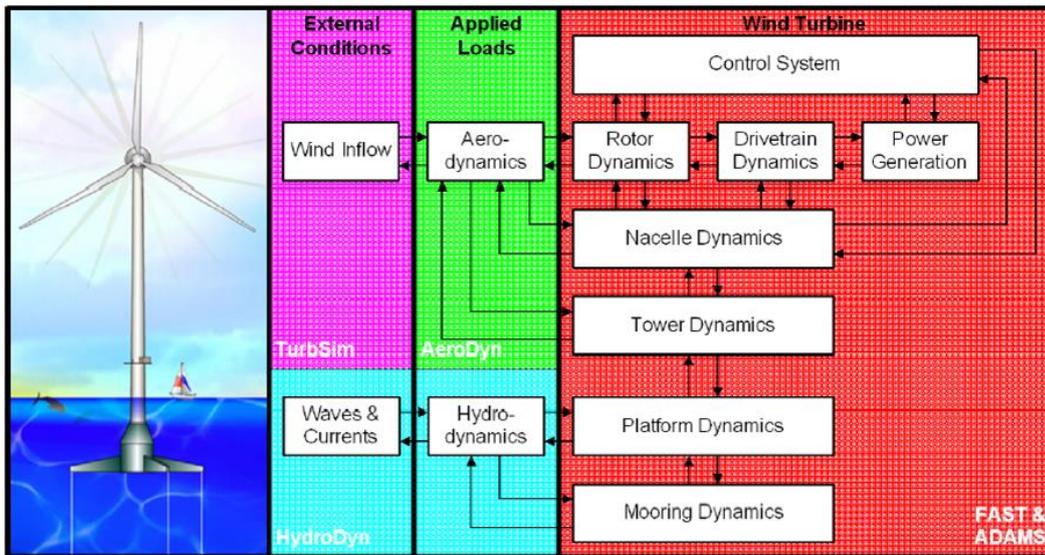
Figure 3.1 FAST modules and interfaces [62]

The main differences between HAWT and VAWT are the configuration and the aerodynamics. ElastoDyn deals with the geometric layout, coordinate systems and structural dynamics. Since this study assumed all bodies are rigid, all deflections in ElastoDyn and BeamDyn are not considered and remained as future work. The control dynamics is out of the scope of this study, so modifying ServoDyn is remained as future work as well. The present work used AeroDyn for the aerodynamic calculation so did not use AeroDyn v14 at all. The modules dealing with the substructure and mooring systems do not need to be changed because the geometry of a turbine does not affect their geometry and dynamics. Overall, the structure of the developed integrated analysis code is like Figure 3.2.

The input data, code structure and expressions were kept as an original version of them if possible. All changes were based on Jonkman's previous study on FAST [63] and other

reports and publications about the improvements of FAST.
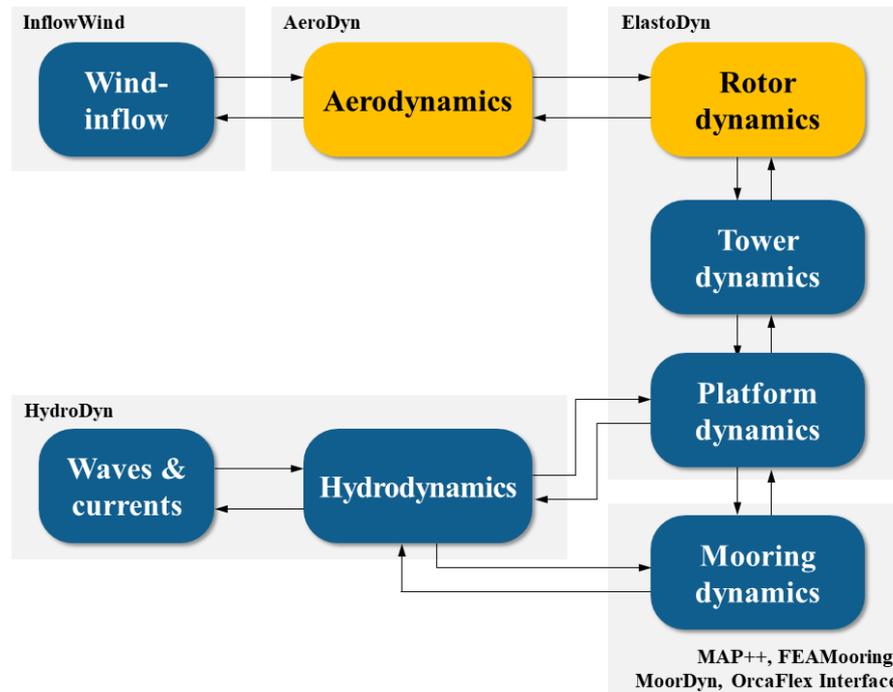


Figure 3.2 Code structure of the developed integrated analysis code for FOVAWT

The following section will firstly discuss the changes in ElastoDyn, such as the geometry of the turbine, coordinate system, and degrees of freedom and AeroDyn and then introduce the hydrodynamics and mooring dynamics.

## 3.2 STRUCTURAL MODELLING

Because of the changes in geometry, some of the coordinates and structural inputs should be modified to suit for the VAWT. VAWT has structurally modelled as a combination of rigid bodies–the Earth (Body E), tower (Body F), tower-top (Body B), hub (Body H), blades (Body

M, max. 3), platform (Body X). As the present study considers the H-type Darrieus wind turbine, input values and geometry calculation of ElastoDyn need to be changed.

### 3.2.1 CHANGES IN INPUT PARAMETERS

Figure 3.3 shows a simplified configuration of the turbine. All blades are located the rotor radius ('RotRad') away from the hub. The hub is at the centre of the tower-top and is assumed to be a single point. The distance from the bottom of the blade or the top of the blade to the hub is half the blade length ('BldLength'). Other inputs used for the calculation of the HAWT configuration are neglected.
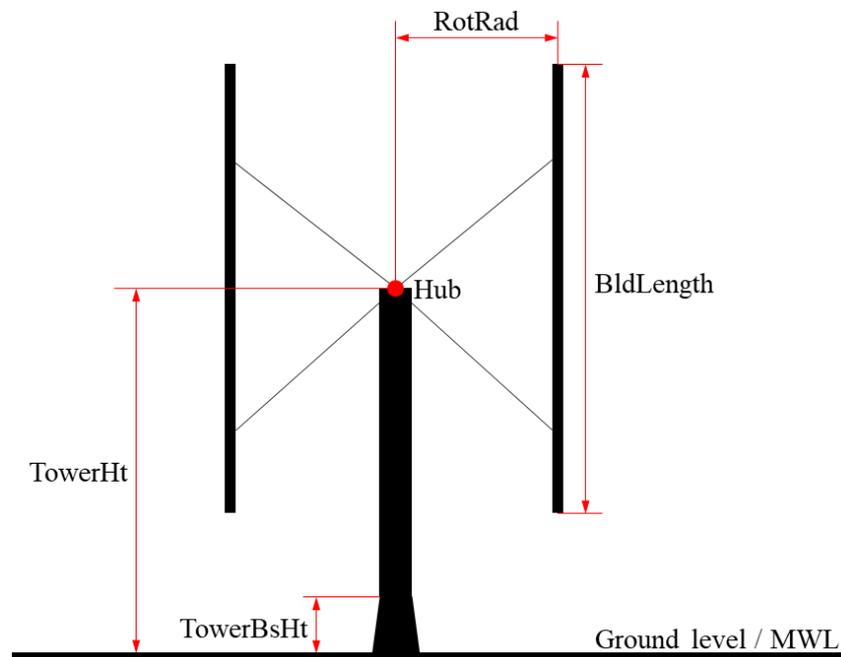


Figure 3.3 Configuration of the H-type Darrieus wind turbine

3.2.2 COORDINATE SYSTEMS AND STRUCTURAL MODELLING

The coordinate system of the integrated analysis code based on the coordinate systems of FAST is set as follows. Inertial coordinates ($x_i$, $y_i$, $z_i$), tower-base/platform coordinates ($x_t$, $y_t$, $z_t$), tower-top coordinates ($x_p$, $y_p$, $z_p$) and tower element-fixed coordinates ($L_{xt}$, $L_{yt}$, $L_{zt}$) are the same as those of FAST for HAWT and graphically described in Figure 3.4.
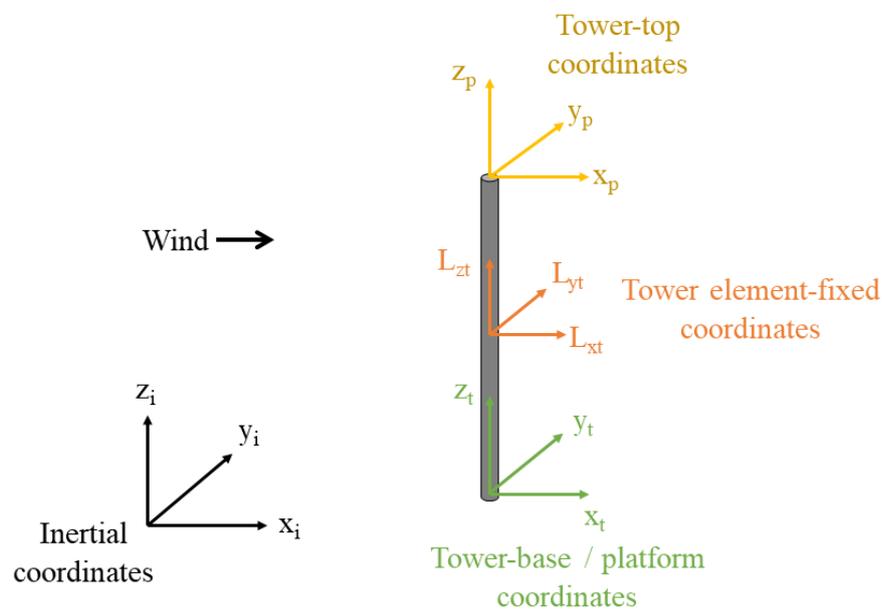


Figure 3.4 Inertial, tower-base/platform, tower-top and tower element-fixed coordinates

Figure 3.5 shows the coordinate systems at the tower-top, hub and blades. Since the rotor of the VAWT rotates around the z-axis, azimuth coordinates ($\boldsymbol{x_a}$, $\boldsymbol{y_a}$, $\boldsymbol{z_a}$) rotate by an azimuth angle about $z_p$ as equation (3.1). Hub coordinates ($\boldsymbol{x_h}$, $\boldsymbol{y_h}$, $\boldsymbol{z_h}$) is not shown in the figure, but the same as azimuth coordinates. Blade coordinates ($\boldsymbol{x_i}$, $\boldsymbol{y_i}$, $\boldsymbol{z_i}$) and blade

element-fixed coordinates ($L_{xb}$, $L_{yb}$, $L_{zb}$) of each blade are calculated as equation (3.2).
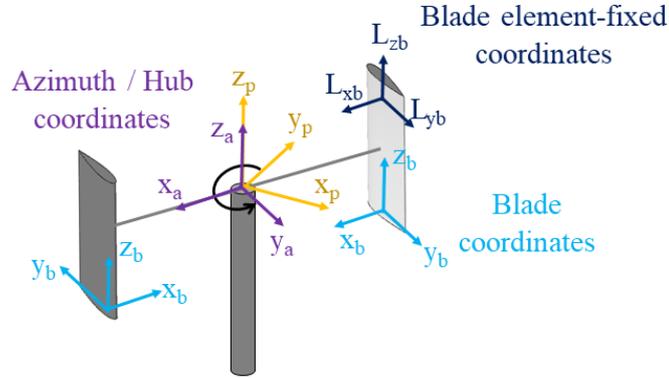


Figure 3.5 Azimuth/hub, blade, blade element-fixed coordinates

$$\begin{bmatrix} x_h \\ y_h \\ z_h \end{bmatrix} = \begin{bmatrix} x_a \\ y_a \\ z_a \end{bmatrix} = RotationMatrix \begin{bmatrix} x_p \\ y_p \\ z_p \end{bmatrix} \tag{3.1}$$

where $RotationMatrix = R(\vartheta_z)_1 * R(\vartheta_y)_2 * R(\vartheta_x)_3$ and $\boldsymbol{\vartheta} = [0.0 \quad 0.0 \quad time *$

$RotSpeed]$.

$$\begin{bmatrix} x_b \\ y_b \\ z_b \end{bmatrix} = RotationMatrix \begin{bmatrix} x_h \\ y_h \\ z_h \end{bmatrix} \tag{3.2}$$

where $RotationMatrix = R(\vartheta_z)_1 * R(\vartheta_y)_2 * R(\vartheta_x)_3$ and $\boldsymbol{\vartheta} = [0.0 \quad 0.0 \quad (k-1) *$

$2\pi/NumBlade]$. In this study, as the blade deflection is not considered, all blade

element-fixed coordinates are identical to the blade root coordinates.

Blade root position with respect to the ground level/mean water level is calculated as equation (3.3). The positions of the other elements of the blade are calculated based on the blade root position.

$$[0.0 \quad 0.0 \quad TowerHt - BldLength/2] + RotRad * \boldsymbol{x}_b \tag{3.3}$$

## 3.3 AERODYNAMICS

Aerodynamics for VAWT of the integrated code is almost the same as the aerodynamics described in Chapter 2. To be combined with other FAST modules for integrated analysis, there are few changes in the code.

In the case of the floating VAWT, the efforts to include the platform pitch motion and resulting tower tilting into the aerodynamic analysis were made by Wang et al. [36] and Guo et al. [64]. Floating wind turbines move with 6 degrees of freedom, and each blade and tower element, rigidly connected with the floating platform, consequently, has the instantaneous translation velocity. The induced wind velocity at upwind and downwind zone should account for the translation velocity of each blade as equation (3.4) and (3.5) where $v_{bld}$ is the blade translation velocity due to the platform motion.

$$\boldsymbol{v}_i = u_1(\boldsymbol{v}_\infty - \boldsymbol{v}_{bld}) \tag{3.4}$$

$$\boldsymbol{v}'_i = u_2(\boldsymbol{v}_e - \boldsymbol{v}_{bld}) \tag{3.5}$$

61

## 3.4 HYDRODYNAMICS

FAST has a module for hydrodynamics, named 'HydroDyn'. HydroDyn contains a potential-flow theory and Morison's equation. The hydrodynamic loads on the floating platform, calculated in HydroDyn, is passed to the FAST and FAST gives the platform motions to HydroDyn as Figure 3.6. Since hydrodynamic modelling for HydroDyn is well described in several papers [65][66][67][68], the hydrodynamics in time-domain is briefly presented here.

**Aero-Elastics**
$$M_{ij}(q,u,t)\ddot{q}_j = f_i(q,\dot{q},u,t)$$

Platform motions $(q_j, \dot{q}_j, t)$

Hydrodynamic loads $(A_{ij}, f_i)$

**Time-domain Hydrodynamics**
$$A_{ij} = A_{ij}(\infty), f_i = F_i^W + F_i^V + F_i^M + \rho g V_0 \delta_{i3} - C_{ij}^{HS} q_j - \int_0^t K_{ij}(t-\tau)\dot{q}_j(\tau)d\tau$$

Platform position $(q_j)$

Mooring restoring $(F_i^M)$

**Mooring dynamics**
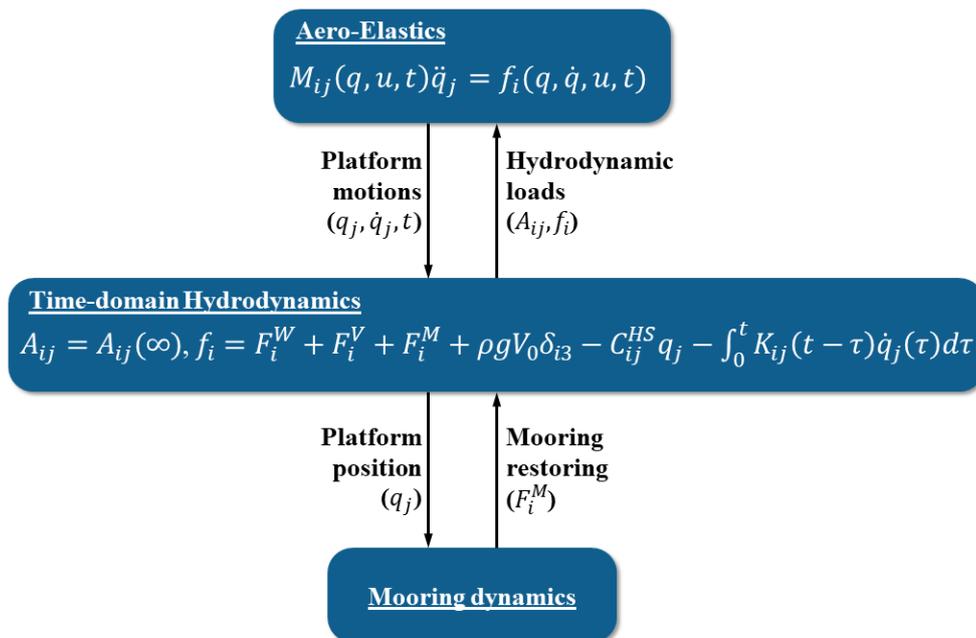
Figure 3.6 Interface of HydroDyn with the other modules

Hydrodynamic loads in time-domain comprise the followings:

- Added mass($A_{ij}(\infty)$) and damping($\int_0^t K_{ij}(t-\tau)\dot{q}_j(\tau)d\tau$) contributions from wave radiation,

- Incident wave excitation ($F_i^W$) from diffraction,

- Restoring contributions of buoyancy ($\rho g V_0 \delta_{i3}$) and hydrostatics ($C_{ij}^{HS} q_j$) and

- Viscous contributions from Morison's equation ($F_i^V$).

Additionally, the mooring restoring as a result of the calculation of mooring dynamics can contribute ($F_i^M$). The subscripts $i$ and $j$ indicate the mode of the platform DOF, ranging from one to six. $\delta_{i3}$ is the $(i, 3)$ component of the Kronecker-Delta function.

The frequency-domain hydrodynamic loads should be calculated beforehand to obtain each component included in the time-domain hydrodynamic loads. WAMIT is the potential-based 3-D panel program to solve radiation and diffraction problems in the frequency domain. By solving the radiation problem, it gives the added mass ($A_{ij}(\omega)$), which is due to accelerations that are given to the water particles near to the platform, and radiation damping ($B_{ij}(\omega)$), which is the damping of the radially propagating wave generated by the oscillation of the platform. These depend on the oscillation frequency of the mode of the platform motion. By solving the diffraction problem, the incident wave excitation forces/moments ($X_i(\omega, \beta)$) can be obtained. It depends on the incident wave frequency. WAMIT also gives the displaced volume ($V_0$) and the hydrostatic restoring coefficients ($C_{ij}^{HS}$). $C_{ij}^{HS}$ is calculated as equation (3.6). $S_0$ is the waterplane area of the platform, $\rho$ is the water density, $g$ is the gravitational acceleration, and $z_{CB}$ is the vertical location of the centre of buoyancy of the platform. $x$ and $y$ are the distances in $x$- and $y$-axis from the reference to each panel.

$$C_{ij}^{HS} = \begin{bmatrix} 0 & 0 & 0 & 0 & 0 & 0 \\ 0 & 0 & 0 & 0 & 0 & 0 \\ 0 & 0 & \rho g S_0 & 0 & -\rho g \iint_{S_0} x dS & 0 \\ 0 & 0 & 0 & \rho g \iint_{S_0} y^2 dS + \rho g V_0 z_{CB} & 0 & 0 \\ 0 & 0 & -\rho g \iint_{S_0} x dS & 0 & \rho g \iint_{S_0} x^2 dS + \rho g V_0 z_{CB} & 0 \\ 0 & 0 & 0 & 0 & 0 & 0 \end{bmatrix} \quad (3.6)$$

The time-domain hydrodynamics are solved using the frequency-domain solutions. The total added mass and radiation damping load ($F_i^{Rad}$) on the platform is as equation (3.7).

$$F_i^{Rad}(t) = -A_{ij}(\infty)\ddot{q}_j - \int_0^t K_{ij}(t-\tau)\dot{q}_j(\tau)d\tau \quad (3.7)$$

$A_{ij}(\infty)$ is the added mass at an infinite frequency, and it can be estimated by equation (3.8) for the finite set of frequencies.

$$A_{ij}(\infty) = A_{ij}(\omega) + \frac{1}{\omega}\int_0^\infty K_{ij}(t)\sin\omega t\, dt \quad (3.8)$$

$K_{ij}$ in equations (3.7) and (3.8) is an impulse response function, calculated using the

64

frequency-dependent radiation damping as equation (3.9).

$$K_{ij}(t) = \frac{2}{\pi} \int\limits_{0}^{\infty} B_{ij}(\omega) \cos \omega t \, d\omega \qquad (3.9)$$

Incident wave excitation is calculated using the wave spectrum and the incident wave excitation force on the platform per unit incident wave amplitude in frequency-domain, as equation (3.10).

$$F_i^W(t) = \frac{1}{2\pi} \int\limits_{-\infty}^{\infty} W(\omega) \sqrt{2\pi S_\zeta^{2-Sided}(\omega)} X_i(\omega, \beta) e^{j\omega} d\omega \qquad (3.10)$$

$W(\omega)$ is a Fourier transform of a realisation of a white Gaussian noise time-series process with unit variance. Two-sided wave spectrum, $S_\zeta^{2-Sided}$, has a relationship with the one-sided wave spectrum, $S_\zeta^{1-Sided}$, such as Pierson-Moskowitz and JONSWAP wave spectrum, depending on $\omega$ as equation (3.11).

$$S_\zeta^{2-Sided}(\omega) = \begin{cases} \dfrac{1}{2} S_\zeta^{1-Sided}(\omega) & for \ \omega \geq 0 \\ \dfrac{1}{2} S_\zeta^{1-Sided}(-\omega) & for \ \omega < 0 \end{cases} \qquad (3.11)$$

The one-sided JONSWAP wave spectrum from the IEC 61400-3 is as equation (3.12).

$$S_\zeta^{1-Sided}(\omega) = \frac{1}{2\pi}\frac{5}{16}H_S^2 T_P \left(\frac{\omega T_P}{2\pi}\right)^{-5} exp\left[-\frac{5}{4}\left(\frac{\omega T_P}{2\pi}\right)^{-4}\right][1-0.287\ln(\gamma)]\gamma^{exp\left[-0.5\left[\frac{\frac{\omega T_P}{2\pi}-1}{\sigma(\omega)}\right]^2\right]} \quad (3.12)$$

where $\gamma$ is the peak shape parameter, defined as equation (3.13) and $\sigma(\omega)$ is a scaling factor,

defined as equation (3.14).

$$\gamma = \begin{cases} 5 & for \ \frac{T_P}{\sqrt{H_S}} \le 3.6 \\ exp\left(5.75 - 1.15\frac{T_P}{\sqrt{H_S}}\right) & for \ 3.6 < \frac{T_P}{\sqrt{H_S}} \le 5 \\ 1 & for \ \frac{T_P}{\sqrt{H_S}} > 5 \end{cases} \quad (3.13)$$

$$\sigma(\omega) = \begin{cases} 0.07 & for \ \omega \le \frac{2\pi}{T_P} \\ 0.09 & for \ \omega > \frac{2\pi}{T_P} \end{cases} \quad (3.14)$$

Hydrostatic loads include the buoyancy force from Archimedes' principle, $\rho g V_0 \delta_{i3}$, and

the effects of the water-plane area and the centre of buoyancy (CB) as the floating platform is

displaced, $-C_{ij}^{HS}q_j$. $\rho g V_0 \delta_{i3}$ will act due to the continuously changed location of the centre

of mass of the floating wind turbine when the rotor and tower flexibilities are considered.

Morison's equation can be used to obtain the hydrodynamic loads when the diameter of

the body is much smaller than the wavelength so that the diffraction effects do not have to be

considered. Morison's equation is as equation (3.15).

$$F = \rho V \dot{u} + \rho C_A V (\dot{u} - \dot{v}) + \frac{1}{2} \rho C_D A (u - v)|u - v| \tag{3.15}$$

$V$ is the volume of the body, $u$ is the flow velocity, $v$ is the water particle velocity, $C_A$ is the added mass coefficient, $C_D$ is the drag coefficient, and $A$ is the cross-sectional area of the body perpendicular to the flow direction. The first term in RHS of equation (3.12) is Froude-Krylov force, the second one is hydrodynamic force, and the last is the drag force. The drag force alone can be applied to calculate hydrodynamic loads in combination with the contributions from the potential theory ($F_i^V$).

## 3.5 MOORING DYNAMICS

Mooring systems can be modelled as a quasi-static model, dynamic model or lumped mass model. In FAST, there are three modules for mooring calculation. MoorDyn is for lumped-mass mooring dynamics, developed by Hall [69]. MAP++ is developed by Masciola to model the steady-state forces on a multi-segmented, quasi-static mooring line, based on an extension of conventional single line static solutions [70]. FEAMooring is a finite-element-based mooring dynamics module developed by Bae [71]. One more option is OrcaFlexInterface, using OrcaFlex, a commercial programme for the design and analysis of the marine system.

**3.6 SIMULATION MODEL DESCRIPTION**

The integrated analysis code was verified using the simulation model from the study of Cheng et al. [72], as shown in Figure 3.7. In the case of the floating model, the VAWT was moored by three catenary lines, having an angle of 120 deg between the adjacent lines, as shown in Figure 3.8.



(a)                           (b)
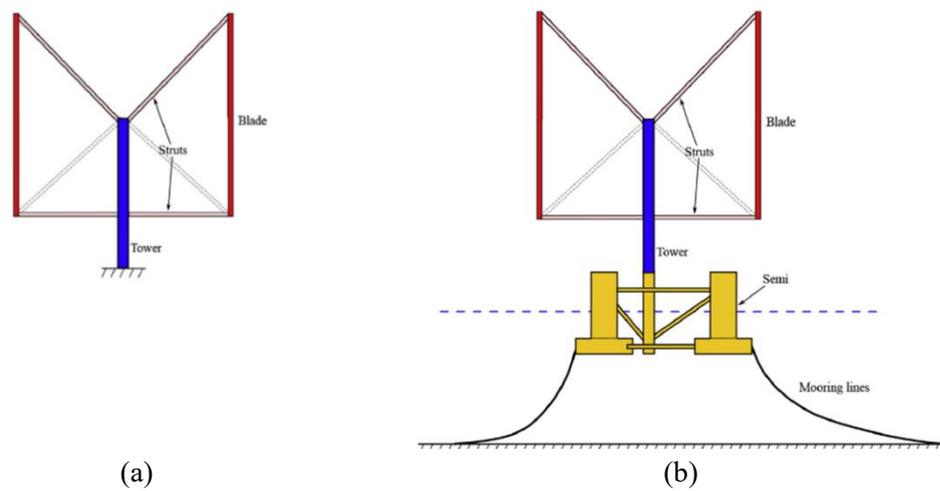
Figure 3.7 Straight-bladed VAWT (a) Land-based model, (b) Floating model
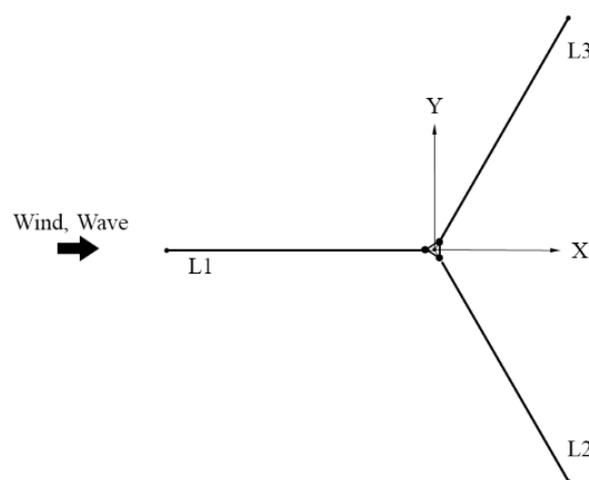


Figure 3.8 Mooring layout

The proposed VAWT is designed for a rated power of 5.3 MW, and the specifications of the rotor are listed in Table 3.2. For the design of the floating VAWT, OC4 semi-submersible and its mooring system were adopted [73]. The properties of the floating VAWT and its mooring system are listed in Table 3.3 and Table 3.4, respectively. The water depth of the installation site was assumed to be 200 m. In the present study, $I_{xx}$ and $I_{yy}$ were assumed to be the same as the OC4 Semisubmersible since the geometry of the substructure was identical. There were small differences in mass and centre of mass, but it was ignored. The detailed information of the semi-submersible platform and mooring system is given by Robertson et al. [73].

Table 3.2 Specifications of the rotor

| Item | Unit | Value |
|---|---|---|
| Rated Power | MW | 5.21 |
| Blade number | - | 2 |
| Rotor Radius | m | 39.0 |
| Blade Height | m | 80.0 |
| Chord length | m | 4.05 |
| Tower height | m | 9.78 |
| Aerofoil section | - | NACA 0018 |
| Cut-in, rated and cut-out wind speed | m/s | 5.0, 14.0, 25.0 |
| Rated rotational speed | rad/s | 1.08 |

Table 3.3 Properties of the floating VAWT

| Item | Unit | Value |
|------|------|-------|
| Draft | m | 20 |
| Topside mass (rotor, tower, shaft, struts) | ton | 350.1 |
| Centre of mass for rotor above MWL | m | 51.03 |
| Platform mass (Substructure, ballast, generator) | ton | 13761.3 |
| Centre of mass for platform above MWL | m | -13.44 |
| Buoyancy at the equilibrium position | kN | 139816 |
| Centre of buoyancy above MWL | m | -13.15 |

Table 3.4 Properties of the mooring system

| Item | Unit | Value |
|------|------|-------|
| Number of mooring lines | - | 3 |
| Depth to anchors below MWL | m | 200 |
| Depth to fairleads below MWL | m | 14 |
| Unstretched length | m | 835.5 |
| Mooring line dry mass density | kg/m | 113.35 |
| Mooring line wet mass density | kg/m | 108.63 |
| Mooring line extensional stiffness | MN | 753.6 |
| Hydrodynamic drag coefficient | - | 1.1 |
| Hydrodynamic added-mass coefficient | - | 1.0 |

In the present simulation, the HydroDyn model for the substructure was a hybrid containing a potential-flow solution and Morison's equation for viscous-drag loads. Water ballasting was simplified by summation of its mass to the whole platform mass. As a result, the centre of mass for the platform was the result containing the water ballast. The loads due to sea currents and the second-order wave-excitation loads were not considered. For mooring calculation, MoorDyn was used.

## 3.6.1 VERIFICATION OF THE PROPERTIES OF FLOATING VAWT

Since there might be some differences in features because of the lack of information and in settings between the developed code and the code used in the literature, the verification of the floating turbine must take precedence. Firstly, free decay simulations were carried out in 6 DOF to obtain natural periods. Next, response amplitude operators (RAOs) in each mode were computed using a white-noise spectrum.

### 3.6.1.1 FREE DECAY SIMULATIONS

From free decay simulations in three translation modes (surge, sway and heave) and three rotation modes (roll, pitch and yaw), the natural periods of the floating platform can be obtained. Figure 3.9 is the time histories of the floating VAWT in 6 DOF.
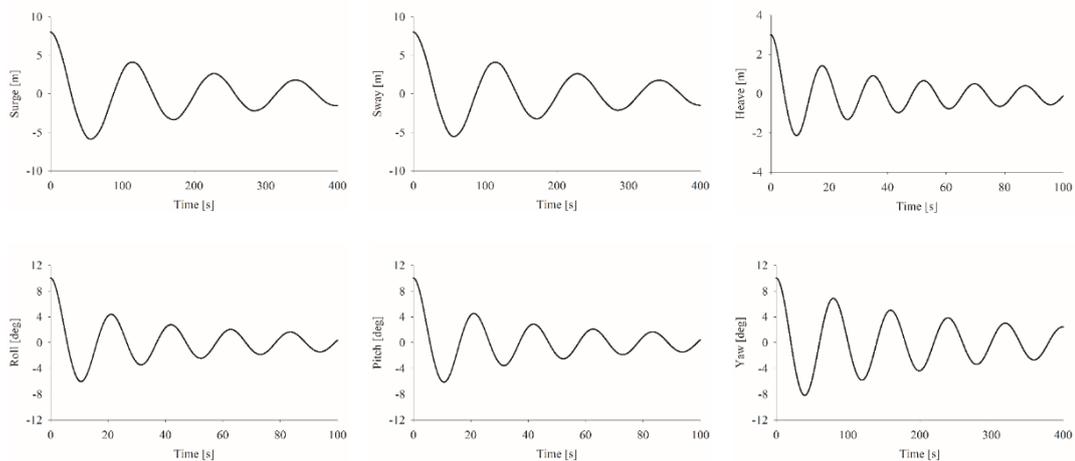


Figure 3.9 Time histories from free decay simulations in 6 DOF

From the free decay results, the natural periods were calculated as listed in Table 3.5. The natural periods in all six modes of this study show very slight differences from the literature. The differences in the natural periods in surge and sway are about 0.8 and 0.9 s, respectively. The heave natural period of this study is almost the same as the literature, showing the difference of about 0.2 s. In the case of roll and pitch, the natural periods are relatively smaller than those of literature, showing differences of 0.5 s. The yaw natural period of this study is also smaller than the literature, differing 0.6 s. These results indicate all geometrical properties including the mass moments of inertia ($I_{xx}, I_{yy}$) are well implemented in the present study.

Table 3.5 Natural periods of the floating VAWT

|  | Unit | Surge | Sway | Heave | Roll | Pitch | Yaw |
|---|---|---|---|---|---|---|---|
| Natural period | s | 113.97 | 114.02 | 17.27 | 20.78 | 20.74 | 79.78 |

3.6.1.2 RAOS USING A WHITE-NOISE SPECTRUM

Using white-noise wave excitation and the associated time-domain responses, FAST can compute the RAOs, and Ramachandra et al. verified the RAOs from FAST by comparing to the RAOs from WAMIT [74]. The present study also investigated the surge, heave and pitch RAOs of the floating VAWT using FAST, as shown in Figure 3.10. White-noise waves with a

significant wave height of 2 m were used. Because of the incident wave direction, the noticeable motion of the floating turbine occurs in the surge, heave and pitch. As expected, all the RAOs have peaked at around its natural frequencies of 0.0551 in the surge, 0.3638 in the heave and 0.3030 in the pitch. Surge RAO has an additional peak at around the natural frequency of pitch because of the coupled effect, and this effect is observed in the pitch RAO, which has the peak at the natural frequency of surge. Heave RAO also has an additional peak at the natural frequency of pitch. In all RAOs, especially heave and pitch, there is non-zero response beyond 0.4 rad/s due to the white noise wave.
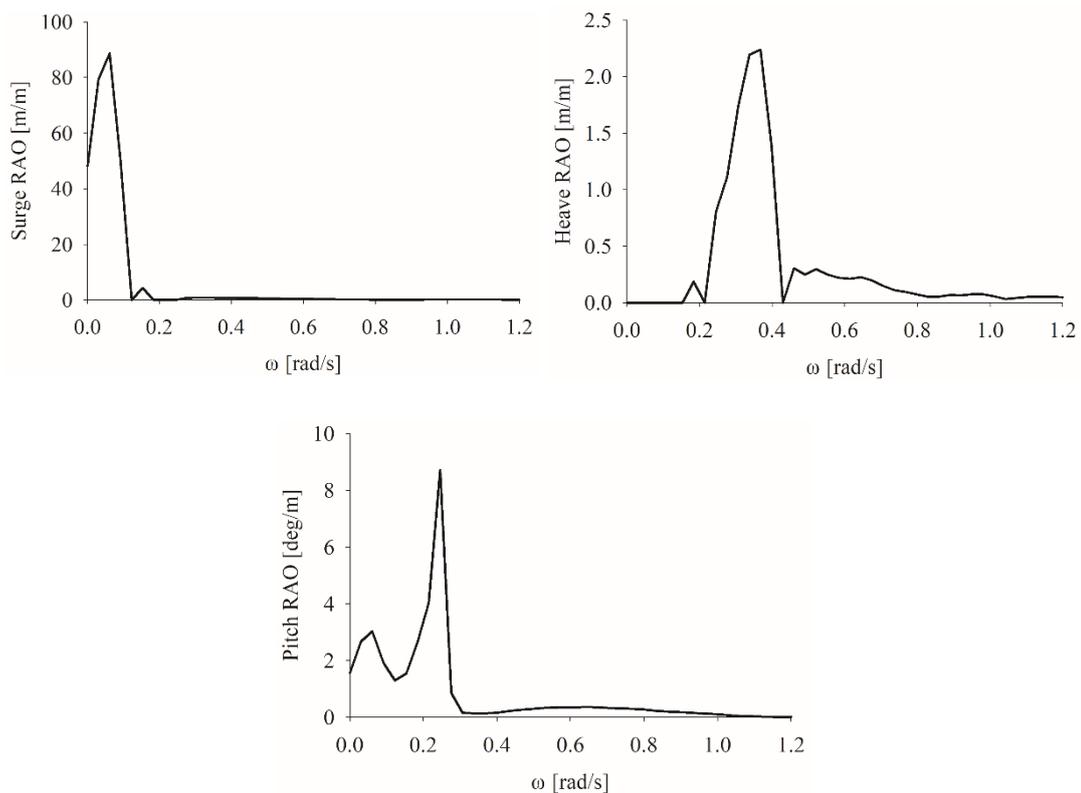
Figure 3.10 Surge, Heave, Pitch RAOs using white noise spectrum

## 3.7 RESULTS AND VALIDATION

Table 3.6 gives the load cases for the time-domain simulations. In the present study, control strategies for the VAWT were not included. For this reason, the wind speed was considered from the cut-in wind speed (5 m/s) up to the rated wind speed (14 m/s) as a steady wind. First, the simulations of the land-based and floating VAWT were conducted under the steady wind conditions with no waves (LC 1.1–1.5). Secondly, the simulations of the floating VAWT were carried out under steady wind and irregular wave conditions in order to watch the effect of the waves on the whole wind turbine (LC 2.1–2.5). Current was not considered. For all simulations, external loads were collinear, and their headings were fixed at 0 deg, as indicated in Figure 3.8.

Table 3.6 Load cases for time-domain simulations

| LC | Wind $U_{ref}$ [m/s] | $H_S$ [m] | Wave $T_P$ [s] | Wave Spectrum | Simulation time [s] |
|----|-----|-----|-----|-----|-----|
| 1.1 | 5 | - | - | - | 100, 3600 |
| 1.2 | 8 | - | - | - | 100, 3600 |
| 1.3 | 10 | - | - | - | 100, 3600 |
| 1.4 | 12 | - | - | - | 100, 3600 |
| 1.5 | 14 | - | - | - | 100, 3600 |
| 2.1 | 5 | 2.10 | 9.74 | | 4600 |
| 2.2 | 8 | 2.55 | 9.86 | | 4600 |
| 2.3 | 10 | 2.88 | 9.98 | JONSWAP | 4600 |
| 2.4 | 12 | 3.24 | 10.12 | | 4600 |
| 2.5 | 14 | 3.62 | 10.29 | | 4600 |

Each simulation with steady wind condition with no waves lasted 100 s for the land-based wind turbine. In the case of the floating wind turbine, the simulation lasted 3600 s to capture the turbine motion after stabilisation. The simulations with the irregular waves as well as the steady wind, the simulation time lasted 1000 s longer for an hour dynamic analysis.

### 3.7.1 STEADY WIND CONDITIONS WITH NO WAVES

Figure 3.11 shows the mean value of the thrust and aerodynamic torque of the land-based and floating VAWTs in the steady wind conditions (LC 1.1–5). The mean values of the thrust and torque calculated by the developed code are very close to those from the literature in both cases–land-based and floating VAWTs. The differences appear apparently near rated wind speed. These may be a result of different aerodynamic analysis scheme, including the dynamic stall effect. Furthermore, the tower deflection, which is not accounted for in the present study, could lead to these differences.
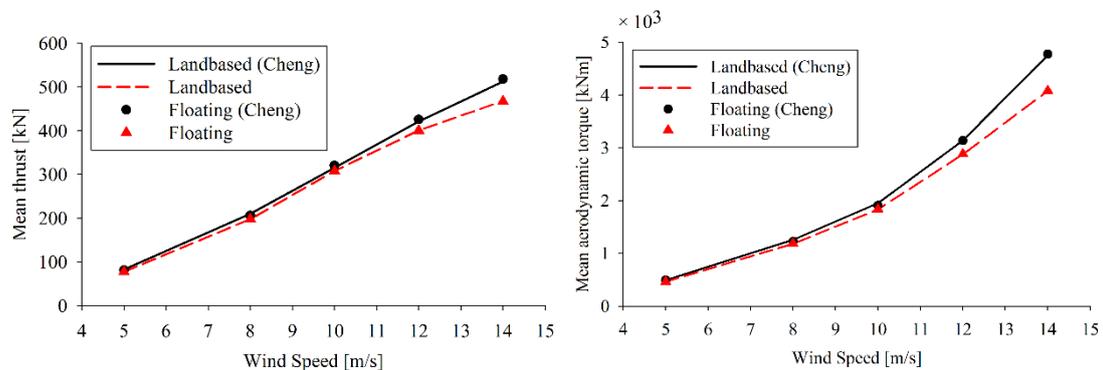


Figure 3.11 Mean values of thrust and aerodynamic torque of the land-based and floating VAWTs in steady wind conditions

Figure 3.12 and Figure 3.13 show the mean value and standard deviations of the tower-base fore-aft and side-to-side moments. The mean and STD values of the present work show similar tendencies compared to that of the literature. The magnitude of it is close to the one from the literature in low wind speed for both cases, but the differences become more significant in high wind speed, especially for the floating turbine. In the present study, it was assumed that all bodies, consisting of the wind turbine, are rigid bodies, meaning that the elasticity is not considered. As a result, the rotor mass, including the blade, hub, struts, and tower, was assumed to be a point mass at the rotor centre of mass. The tower-base loads of the literature include the effects not only of aerodynamic loads, but also contributions from gravity and inertia. For this reason, the assumptions in the present work, in turn, affect the calculation and ultimately cause the discrepancy in the magnitude of results from the literature and the present study.
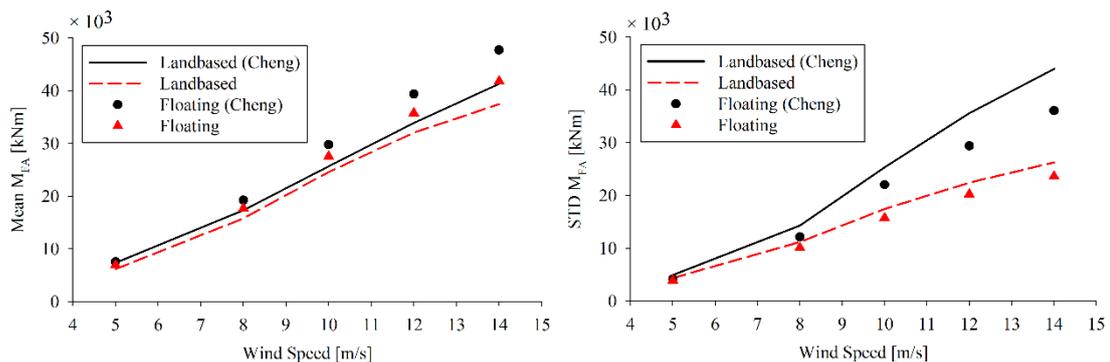


Figure 3.12 Mean and STD values of tower-base fore-aft moments of the land-based and floating VAWTs in steady wind conditions

In Figure 3.12, the higher mean value of the tower-base fore-aft moment is observed when the turbine is floating as a result of the platform pitch motion. In the case of the standard deviation, the floating VAWT shows lower than those of the land-based VAWT. As mentioned in the literature, the mooring system contributes to moderate platform motions. Concerning the tower-base side-to-side moment shown in Figure 3.13, the land-based turbine gives a lower mean value than the floating turbine, unlike the results from the literature. The standard deviations from the developed code in both cases follow the trend those from the literature.
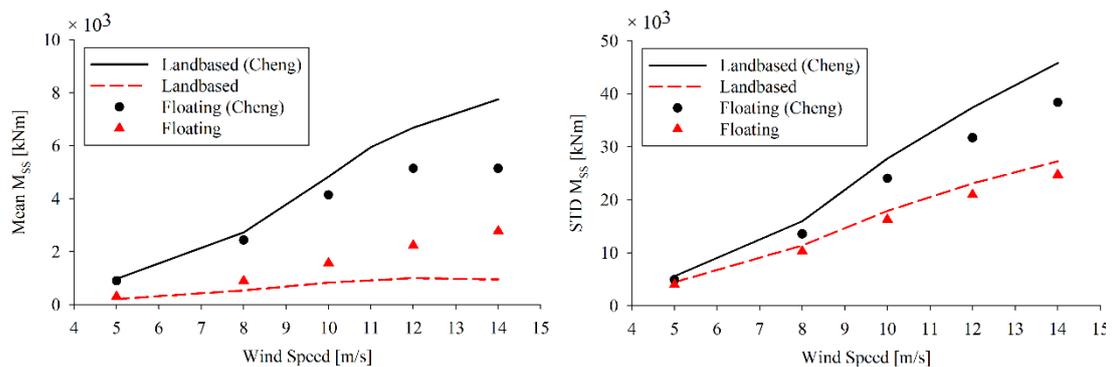


Figure 3.13 Mean and STD values of tower-base side-to-side moments of the land-based and floating VAWTs in steady wind conditions

Overall, the results from the developed integrated analysis code have similar trends to those in the literature. Tower deflection has a considerable effect on the tower-base loads. Unfortunately, the present work did not consider the tower deflection due to the unknown tower properties. Future research is required to include the tower elasticity in the integrated analysis. Moreover, the mass distribution should be included in the analysis for more accurate

predictions.

### 3.7.2 STEADY WIND CONDITIONS WITH IRREGULAR WAVES

Load cases 2.1–5 are with steady wind and irregular waves. By comparing the results of load cases 1.1–5, the effect of the irregular waves on the rotor performance, platform motions and structural loads can be evaluated. Figure 3.14–17 show the mean value and standard deviation (STD) of the rotor performance, platform motions and tower-base loads respectively, under the load cases of the steady wind only (LC1.x) and the combination of the steady wind and irregular waves (LC2.x).

In the case of the rotor performance, it is found that wind loads dominantly affect the mean values. Although there are slight differences in STD depending on the wave loads, the rotor performance is hardly affected by the wave loads.
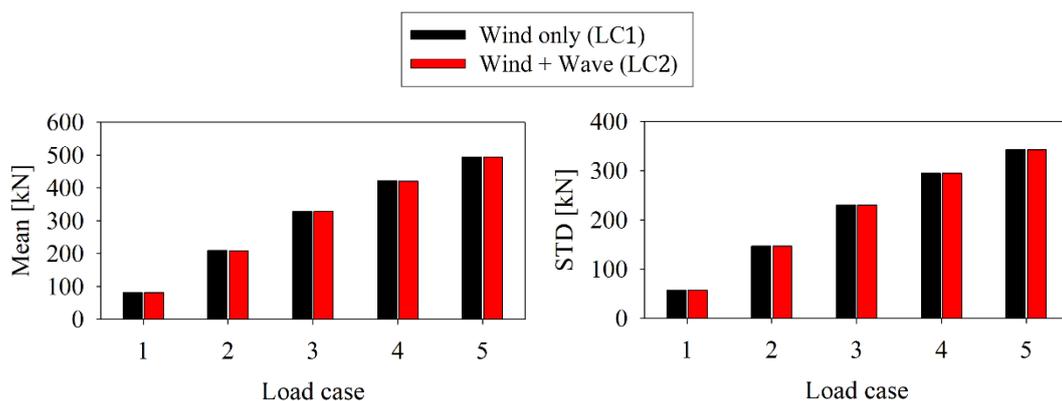


(a) Thrust
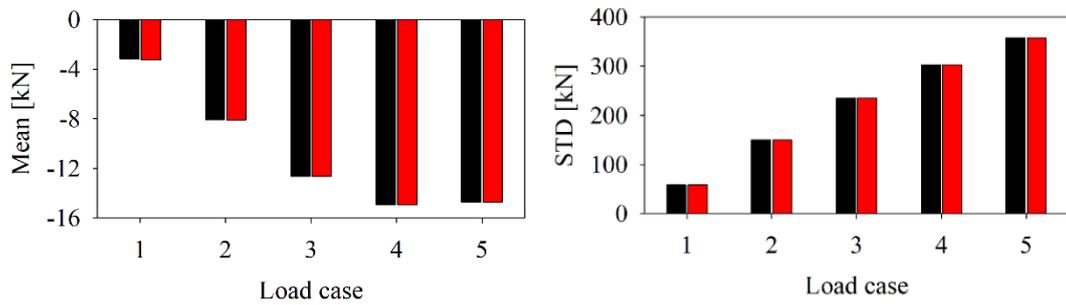
(b) Side force
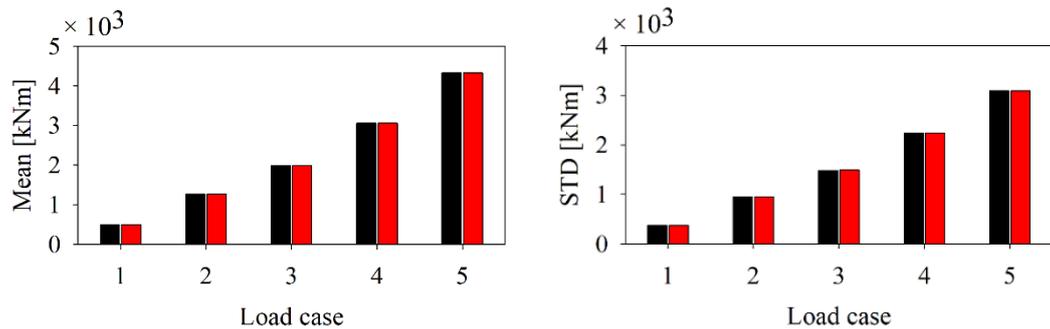


(c) Torque
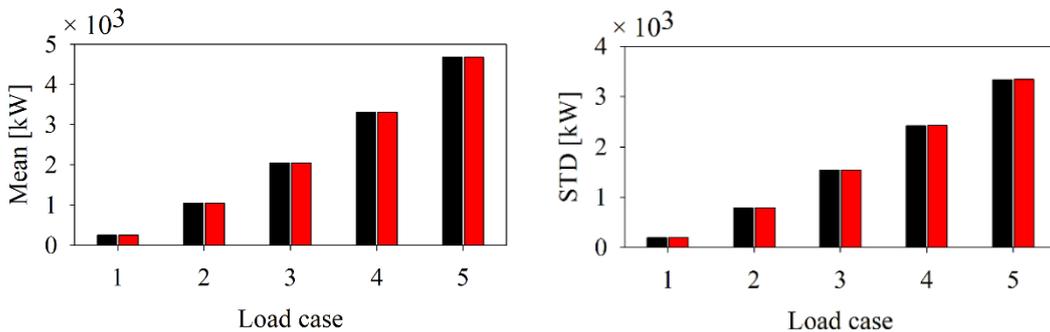


(d) Aerodynamic power

Figure 3.14 Mean and STD values of the loads acting on the rotor and the aerodynamic power in LC1 and LC2

The mean value of the platform motions of the H-type floating VAWTs is dominantly affected by the wind loads, and the wave loads mostly contribute to the standard deviation [72][75], as well shown in Figure 3.15. Surge and pitch motions are related to the thrust. As the thrust increases according to the load cases, the surge and pitch displacements also

increase accordingly. Similarly, sway and roll motions follow the trend of the side force. One of the notable points in this result is that the mean value of yaw displacement is quite large because it correlates to the rotor torque. The wave loads excite the platform motions centred on the mean value, and it is shown in the standard deviations of the platform motions. Due to the incident wave direction, the differences resulting from the wave loads are well visible in surge, heave and pitch modes. The variations of the motions, especially in surge, heave, pitch and yaw, under the irregular wave can be seen in Figure 3.16.

(a)  Surge

(b)  Sway
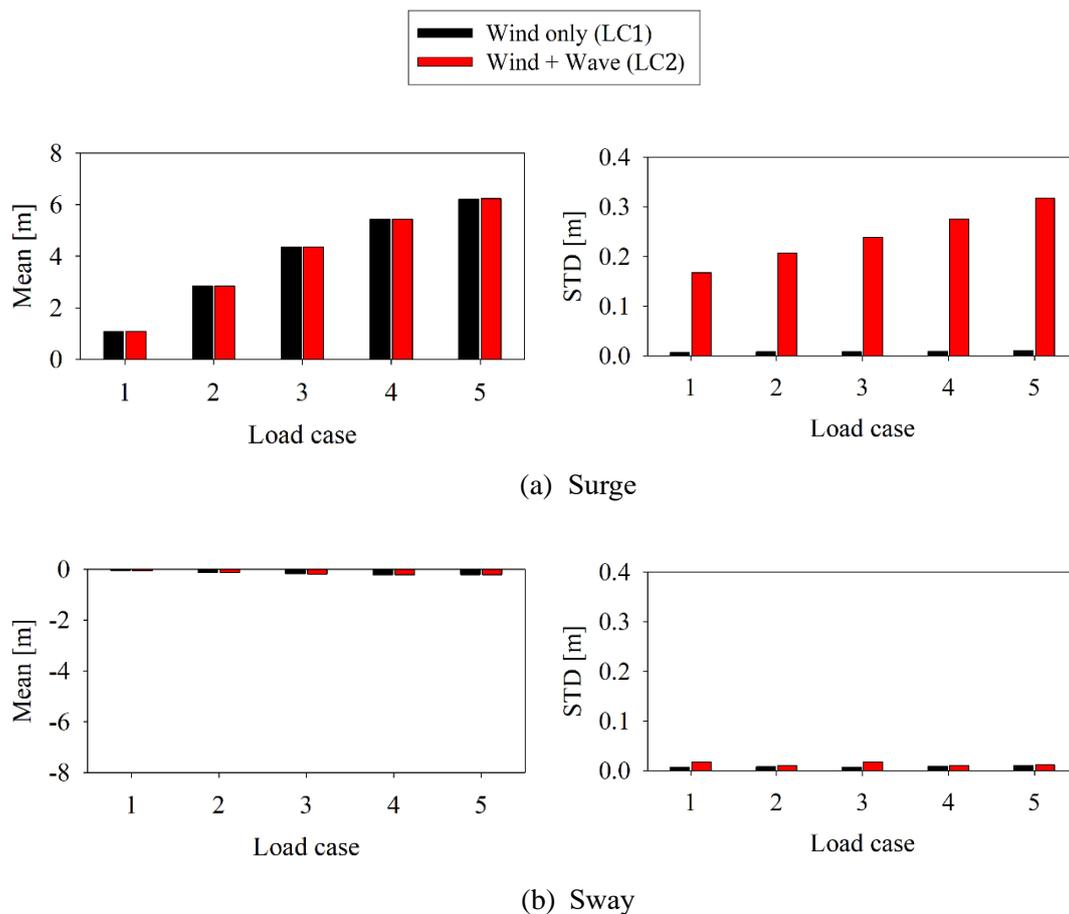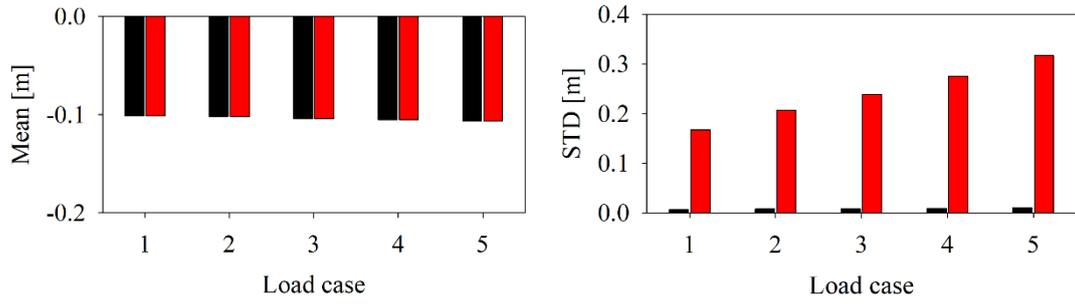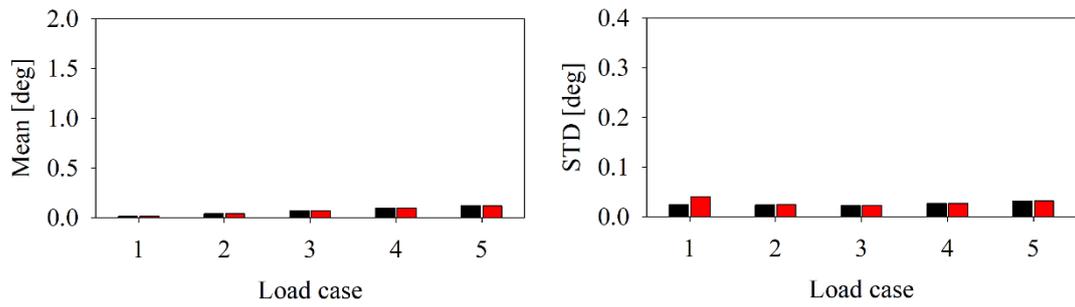
(c) Heave



(d) Roll
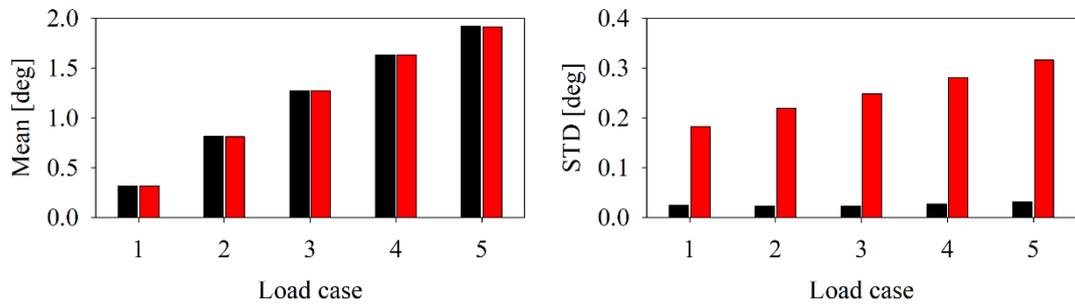


(e) Pitch
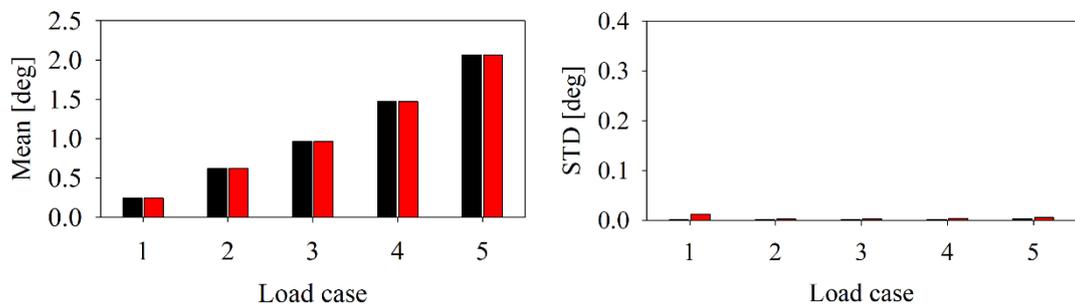


(f) Yaw

Figure 3.15 Mean and STD values of the platform motions in LC1 and LC2

(a) Surge
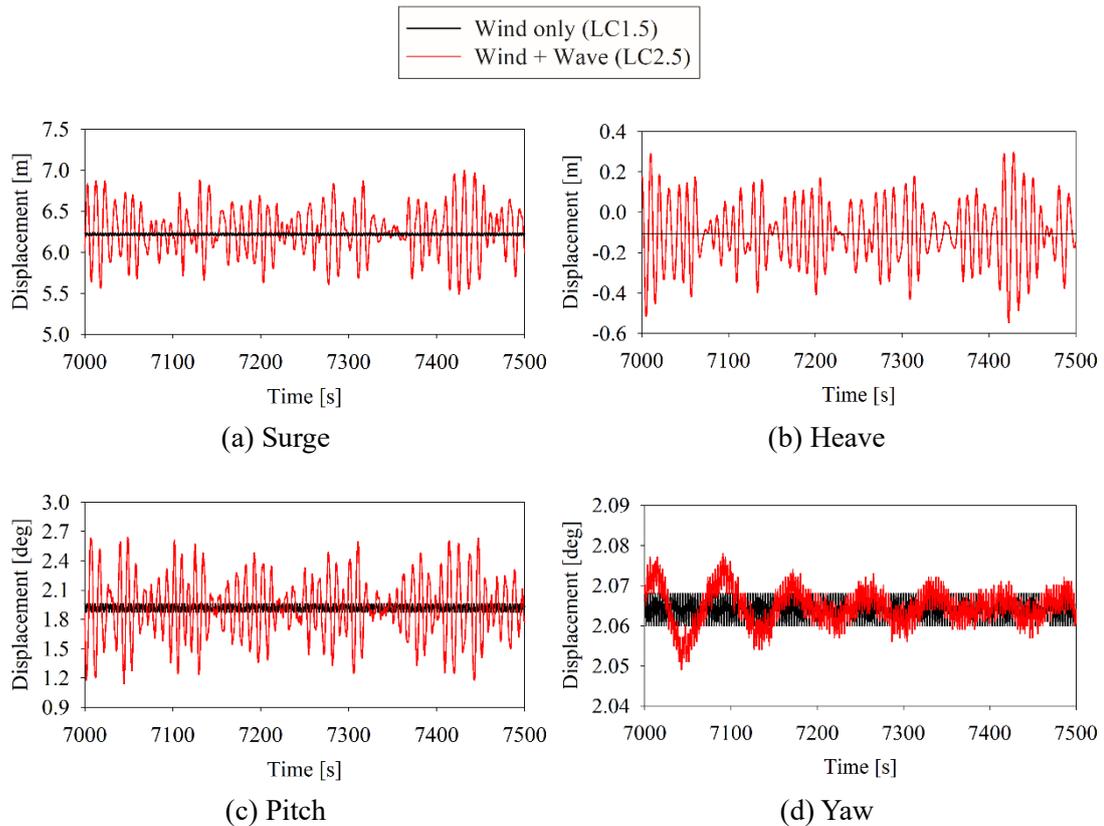
(b) Heave

(c) Pitch

(d) Yaw

Figure 3.16 Time histories of floating VAWT motions in surge, heave, pitch and yaw

As aforementioned, the aerodynamic loads acting on the rotor and the load contributions from gravity and inertia due to the roll and pitch motions of the platform cause the tower-base loads when the wave loads are considered. Since there were little differences in the aerodynamic loads regardless of whether the wave loads were applied or not and the wave loads resulted in slight changes in the standard deviations of the platform motion, the tower-base fore-aft and side-to-side moments are barely affected by the wave loads (Figure 3.17).

(a) Tower-base fore-aft moment

(b) Tower-base side-to-side moment

(c) Tower-base yaw moment
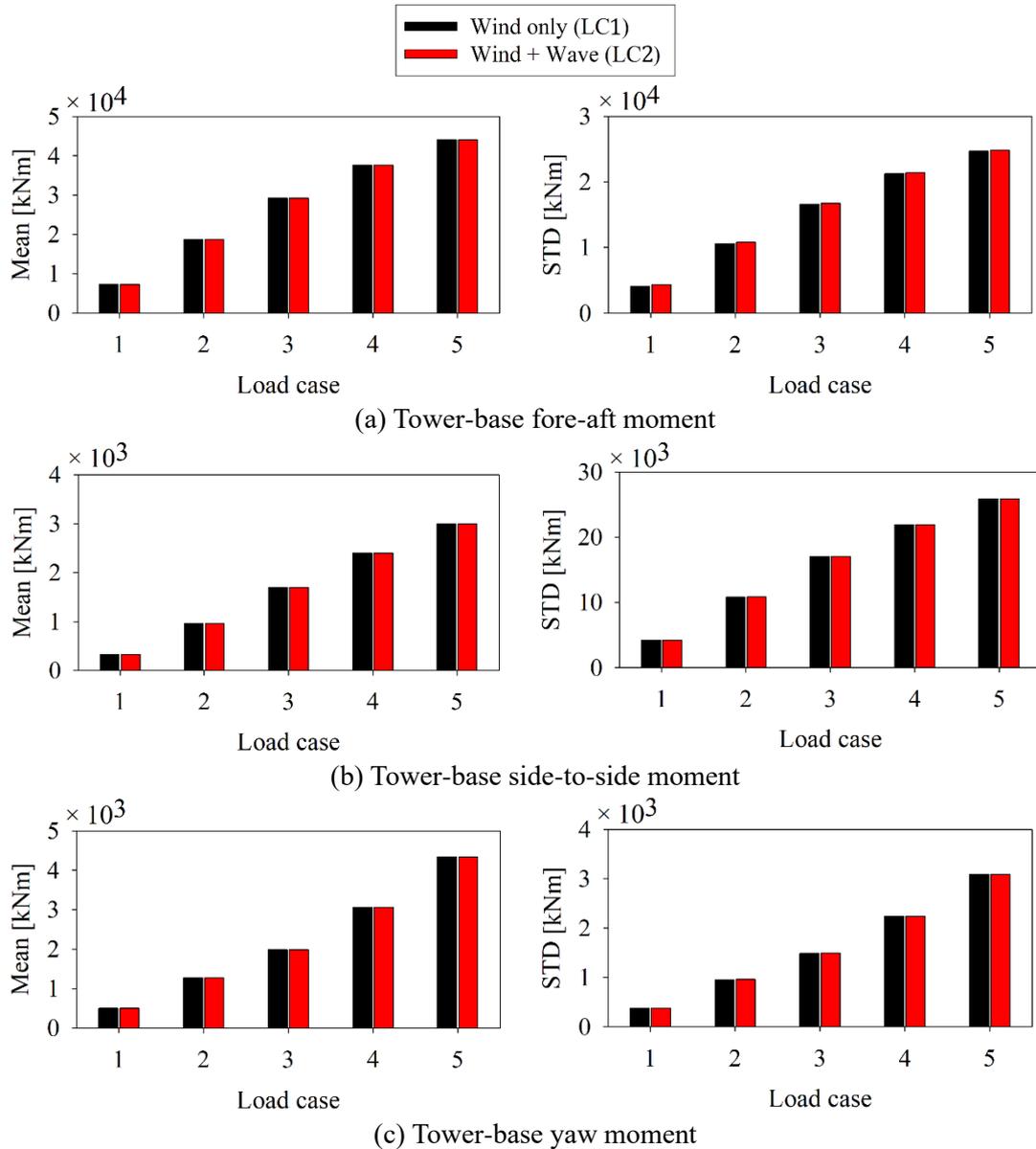
Figure 3.17 Mean and STD values of the tower-base loads in LC1 and LC2

The associated mooring line top tensions need to be checked. As a result of the platform

motions in six modes (Figure 3.15), the mooring line in the weather side (L1) will have a

more considerable tension than other two mooring lines. Figure 3.18 is the mean and standard

deviation values of the tension at the fairlead of L1. As expected, the effect of the wave loads

on the mooring tension is clearly observed at STD.
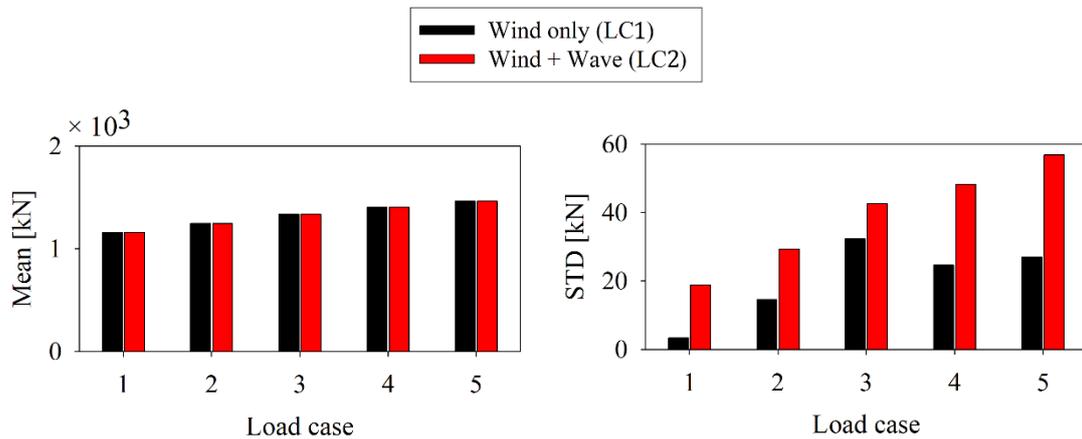


Figure 3.18 Mean and STD values of the tension at fairlead of mooring line L1

## 3.8 COMPUTATIONAL EFFICIENCY

The developed integrated analysis code for FOVAWT aims to have faster computational

time and secure reasonable results compared to the other analysis codes. To assess the

computational efficiency of the developed code, the computational results for LC 1.3 and

time ratio, which defined as simulation time divided by simulation CPU time, were compared.

When comparing thrust and side force curves between Cheng's, CFD and the developed

code (Figure 3.19 (a) and (b)), the magnitudes are similar, but there are differences at the

peaks. In the case of the torque, the differences between CFD and the developed code is

significant, showing a somewhat different trend additionally. The values at three maximum

peaks and three minimum peaks of the results from CFD and the developed code are tabulated

in Table 3.7.



(a) Thrust



(b) Sideforce



(c) Aerodynamic torque
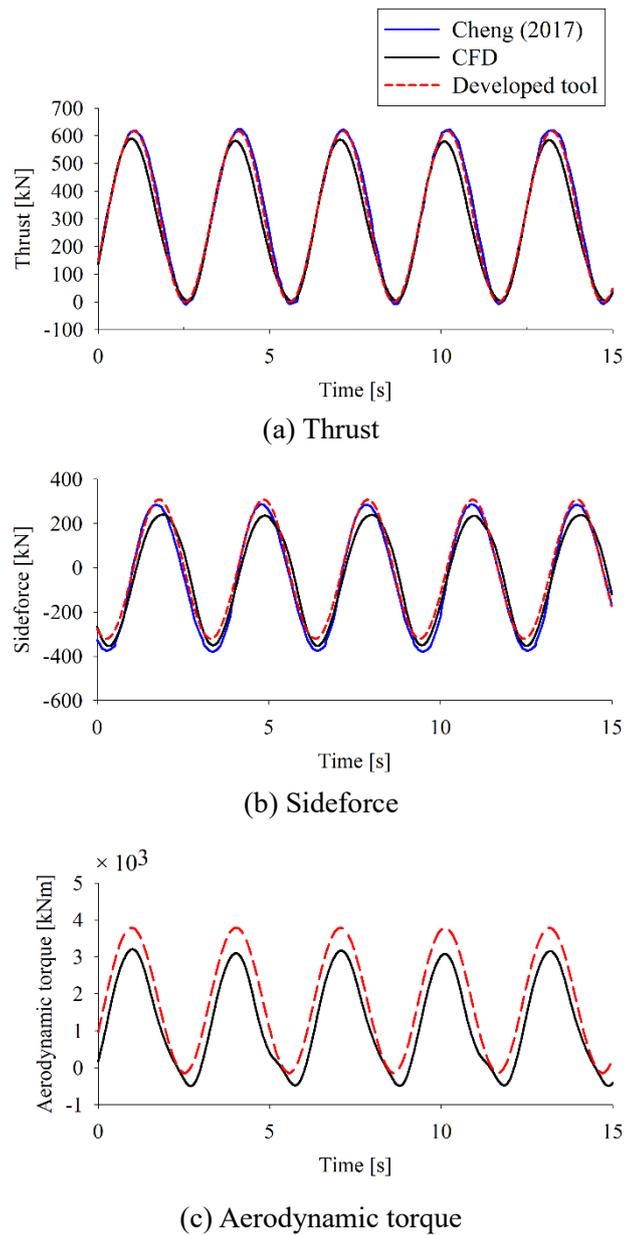
Figure 3.19 Comparison of the analysis results of land-based model for LC 1.3

Table 3.7 Computation results of land-based model for LC 1.3

| | CFD | | Developed analysis code | | % differences | |
|---|---|---|---|---|---|---|
| | Max. | Min. | Max. | Min. | Max. | Min. |
| Thrust [kN] | 589.17 | 3.58 | 616.50 | -0.92 | 4.64 | -125.70 |
| | 581.62 | 3.24 | 616.60 | -0.85 | 6.01 | -126.23 |
| | 585.48 | 3.66 | 616.40 | -0.76 | 5.28 | -120.77 |
| | | | | Average | *5.31* | *-124.00* |
| Sideforce [kN] | 240.14 | -353.39 | 308.10 | -320.70 | 28.30 | 9.25 |
| | 236.12 | -350.49 | 308.20 | -320.80 | 30.53 | 8.47 |
| | 238.87 | -353.28 | 308.20 | -320.90 | 29.02 | 9.17 |
| | | | | Average | *29.30* | *8.96* |
| Torque [kNm] | 3206.47 | -494.05 | 3784.00 | -148.10 | 18.01 | 70.02 |
| | 3097.51 | -481.78 | 3785.00 | -149.70 | 22.19 | 68.93 |
| | 3166.87 | -493.71 | 3787.00 | -152.30 | 19.58 | 69.15 |
| | | | | Average | *19.90* | *69.40* |

Table 3.8 shows the time ratio of CFD and the developed code. Higher time ratio means fast calculation. Therefore, the developed code needs a shorter CPU time for the analysis of the land-based wind turbine with steady wind loading than CFD. Even for the floating wind turbine with steady wind loading and irregular wave loading, the developed code calculates faster than the time for CFD analysis of the land-based wind turbine with a steady wind.

Table 3.8 Time ratio

| | CFD | Developed analysis code | |
|---|---|---|---|
| | Aerodynamics | Land-based | Floating (wind+wave) |
| Time ratio [s] $(\frac{Simulated\ time}{Simulation\ CPU\ time})$ | 6.02E-05 (with 12 processors) | 4.2667 | 0.3168 |

Although the developed integrated analysis code for the floating VAWT under- or overpredicted when compared to the CFD, the magnitude was retained, and computational time was much faster. It proves that the developed code is useful for the preliminary design of the floating wind turbine.

## 3.9 CONCLUSIONS

This chapter introduced the developed integrated analysis code for floating offshore VAWTs. Based on the structure of FAST, the geometry layout and the aerodynamics were appropriately modified for the VAWT in the ElastoDyn and AeroDyn. The advanced analysis code was validated by comparing the results to the literature using the land-based VAWT. Since the present study did not consider the tower elasticity, the magnitude of the rotor performance and the tower-base loads had differences in magnitude when the wind velocity increases. Overall the tendencies of the results from the developed code followed those from the literature.

Due to the absence of the control system in the developed code, the turbulence cannot be included for the simulations. Instead, the effect of the wave loads on the wind turbine performance, platform motions, tower-base loads, and mooring tension was evaluated. As expected, the mean values of the rotor performance were mainly dominated by wind loads, and even the standard deviations of it were hardly affected by wave loads. With respect to the platform motions, the trends of it followed those of the rotor performance. Particularly, the

platform rotated around the vertical axis due to the rotor torque. There were little differences in the mean values despite the wave loads, but waves visibly induced the standard deviations of the platform motions in surge and pitch. Concerning the tower-base moments, wave loads barely affected the results because the effect of the platform motions was relatively smaller than the aerodynamic loads. With regard to the mooring tension, the mean value was mainly affected by the wind load as platform motions. When the wave excited the platform, it resulted in the considerable variation of the standard deviation of the mooring tension as well.

The present validation and analysis results prove that the developed code can predict the rotor performance and platform motion. When the tower elasticity is considered, and the appropriate control is adopted, the developed integrated analysis code for floating offshore VAWT will give more improved results.

# Chapter 4

# CONTRA-ROTATING VAWT

## 4.1 GENERAL

In the case of propellers, there are two concepts to improve its performance. One is the counter-rotating propellers. It has propellers rotating in opposite directions to each other. When it is adopted for aircraft propellers, it is like Figure 4.1 (a). It balances the effects of torque. Another concept is the contra-rotating propellers. It comprises two coaxial propellers rotating in opposite directions about a common axis, as shown in Figure 4.1 (b).



(a)                                          (b)

Figure 4.1 Two concepts of propellers; (a) Counter-rotating propellers (b) Contra-rotating propellers [76][77]

An idea of contra-rotating (coaxial contra-rotating) is used to minimise the effect of

torque. This idea is usually used for aircraft and helicopter propellers or marine propellers. Contra-rotating propeller systems have been dealt with by lots of theoretical and experimental research. Furthermore, it has been used in some practical development exercises. In ship design, contra-rotating propellers possess a capability for balancing the torque reaction from the propulsor as well as the hydrodynamic advantage [78].

These concepts have been adopted for the design of VAWTs as well as HAWTs to take the advantages as introduced in Chapter 1. With a well-designed rotor control system, the two rotors rotating in different directions can eliminate the side force and the effect of torque of the rotor, and, consequently, mitigate the structural loads and responses. As a result, more stable platform motions and reduced fatigue loads in mooring systems can be expected. Hence the present study investigates the contra-rotating VAWT for the use of an offshore wind turbine. The contra-rotating rotor requires further improvement of the developed analysis code by including the two rotors in the aerodynamic calculations. After the code development, the contra-rotating VAWT is analysed for three cases: the land-based WT with the uniform wind, the floating WT with the uniform wind and the floating WT with the uniform wind and irregular waves.

## 4.2 CODE DEVELOPMENT

The developed integrated analysis code was further extended to the contra-rotating VAWT analysis. In the first step, the geometrical layout was modified as Figure 4.2. It was

assumed that both hubs are at the level of the centre of blade length, and all blades were

geometrically identical.
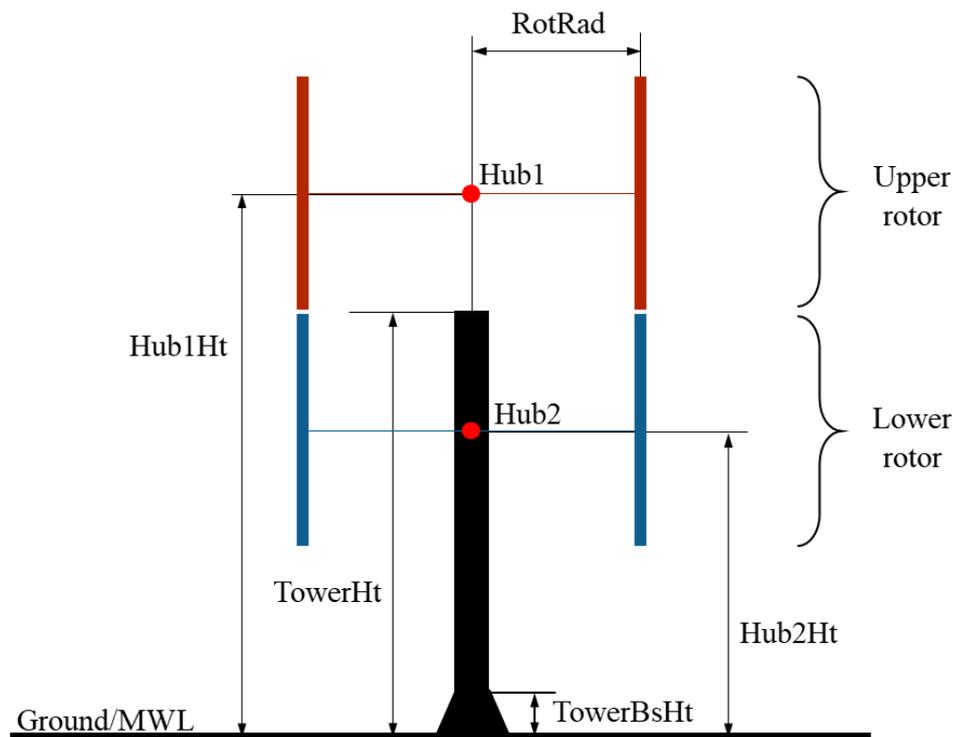
Figure 4.2 Contra-rotating wind turbine

The coordinates and position of each hub and blade were adjusted in ElastoDyn. The

upper rotor was set to rotate in the anti-clockwise direction and the lower rotor in the

clockwise direction (Figure 4.3).

(a) Upper rotor                    (b) Lower rotor
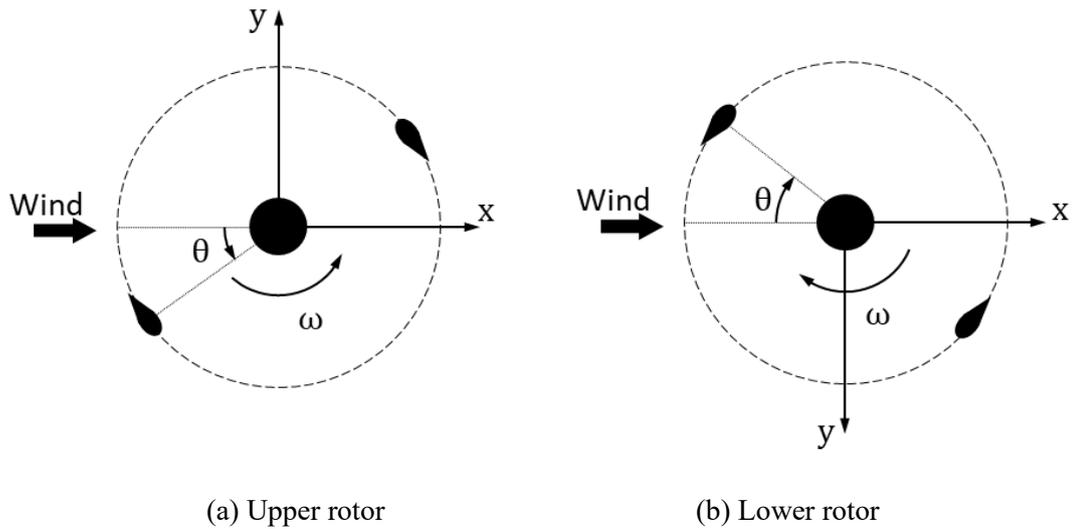
Figure 4.3 Coordinate systems of contra-rotating VAWT

Due to the limitation of the aerodynamic model, the present study did not include the aerodynamic interaction between the upper and lower rotors. The aerodynamic calculation was performed for the full revolution of each rotor. The tip-loss effect was included in the calculation as it showed improved predictions (see Section 2.4).

## 4.3 COMPARISON WITH THE CONVENTIONAL VAWT

In the following section, the effect of contra-rotating VAWT on the rotor performance, platform motions and the resultant tower-base moment has been evaluated by comparing to the results of the conventional VAWT presented in Chapter 3. The geometric configurations are presented in Figure 4.4. At this preliminary study of the contra-rotating VAWT, the total blade length of the conventional VAWT was split into two equal blade lengths. 'Hub1' was assumed to be at an imaginary position. The rotor performance of the contra-rotating VAWT

was estimated at the tower-top in order to compare the results with the conventional VAWT.

The wind was assumed to be uniform with a speed of 14 m/s (rated) to keep the rotational speed of both rotors identical. In the case of waves, the significant wave height and peak period were 3.62 m and 10.29 s respectively (Table 3.6).



(a) Conventional VAWT (Cheng)          (b) Contra-rotating VAWT
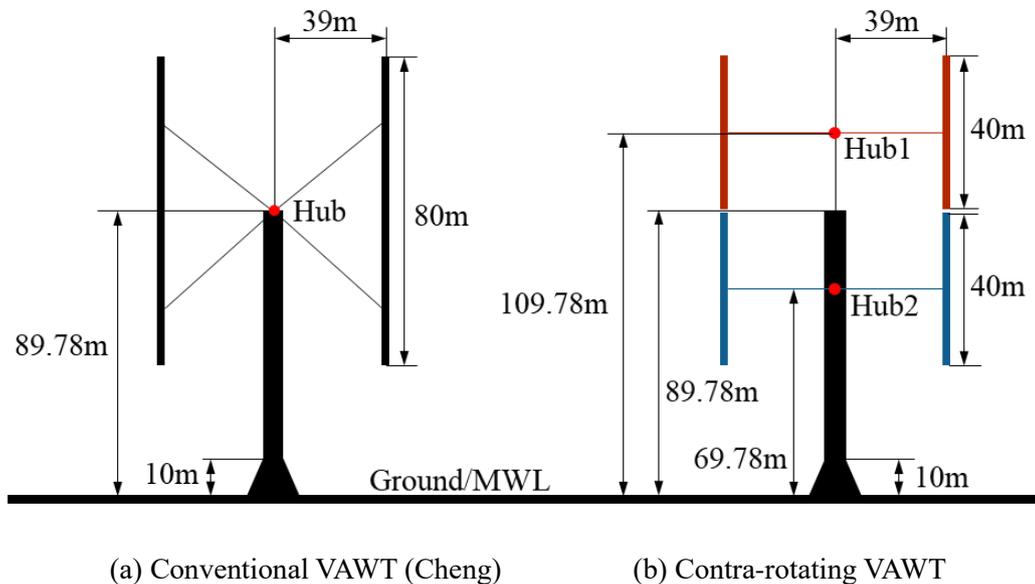
Figure 4.4 Geometrical configurations of the contra-rotating VAWT

Firstly, the rotor performance is compared. Overall, having the contra-rotating rotor reduces the forces acting on the rotor, as shown in Figure 4.5. Due to the tip-loss effect on the shorter blade, the mean values of the thrust of contra-rotating are also reduced by about 15.91 % (land-based model) and 16.84 % (floating model) from that of conventional VAWT. Also, the side forces are reduced due to the effect of the contra-rotating rotors. Aerodynamic torque of the contra-rotating rotor is presented in Figure 4.5(c). The magnitude of the torque applied to

each rotor is the same, but the direction is reversed, so the effect of torque will be cancelled.

However, compared with the aerodynamic power of conventional VAWT, the power of

contra-rotating VAWT decreases by about 28% in both land-based and floating models.



(a) Thrust

(b) Side force

(c) Aerodynamic torque

(d) Aerodynamic power

(solid: upper rotor, dashed: lower rotor)
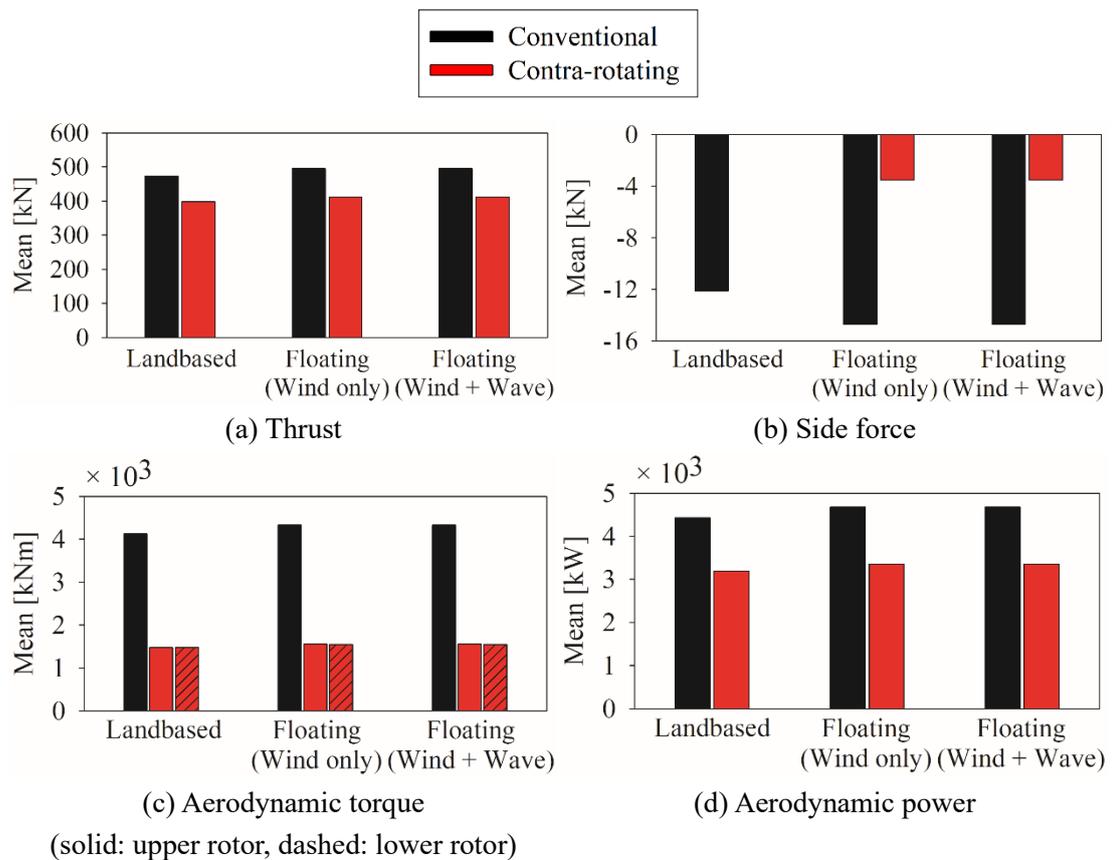
Figure 4.5 Rotor performance of the conventional VAWT and contra-rotating VAWT

In the case of floating wind turbines, the platform surge, pitch and yaw motions are also

affected. As can be seen in Figure 4.6, the mean value of the pitch displacement decreases,

and the variation also mitigates even under the wave loads by adopting a contra-rotating rotor.

The mean value and standard deviation of yaw motion are hardly seen in the case of the

contra-rotating VAWT compared to the conventional VAWT. It is because the effect of the

aerodynamic torque is almost eliminated.



(a) Surge

(b) Pitch

(c) Yaw
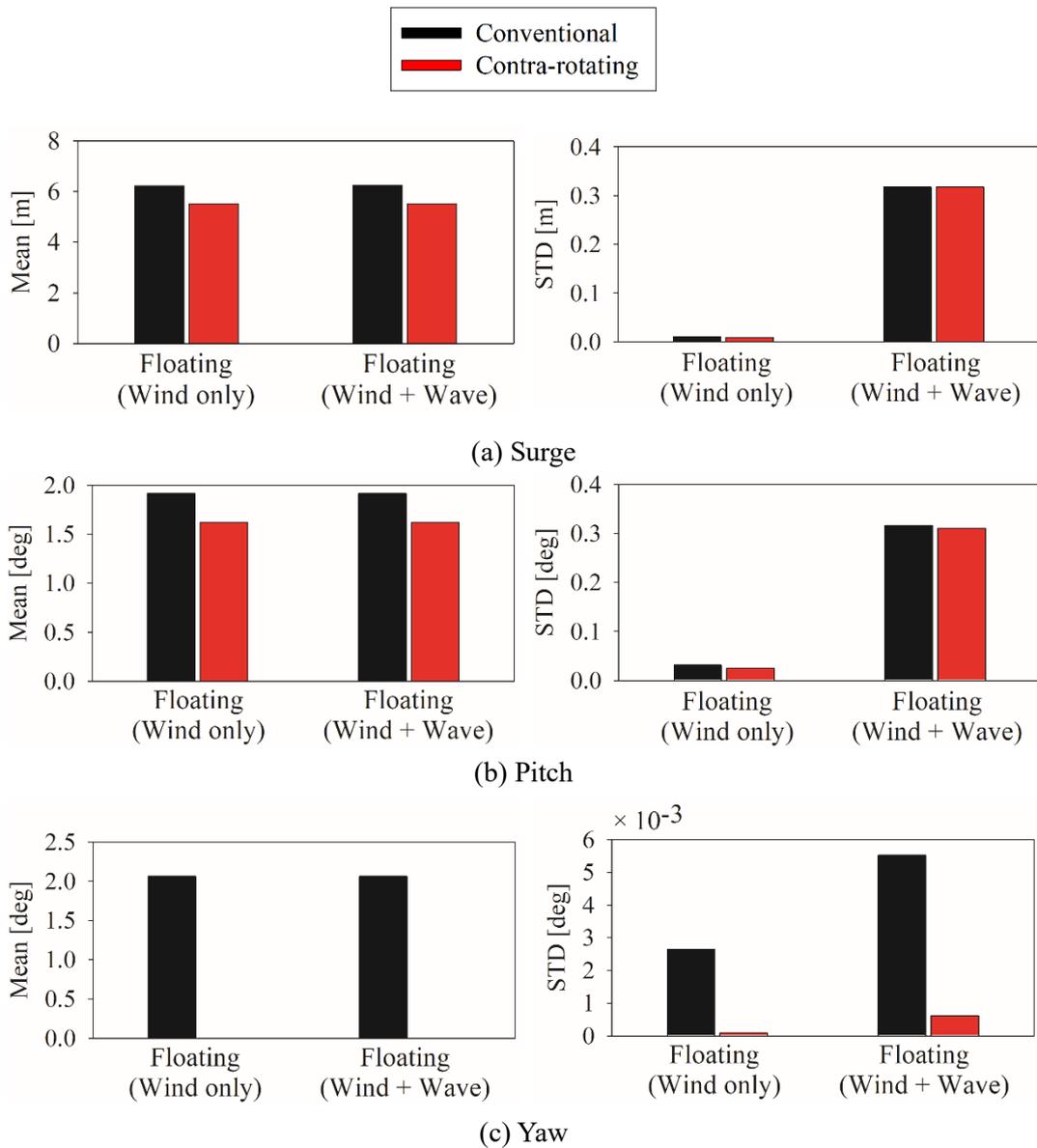
Figure 4.6 Platform displacements of the conventional VAWT and contra-rotating VAWT in the case of floating wind turbines

95

When it comes to tower-base loads, there are decreasing trends as well by adopting the contra-rotating rotor (Figure 4.7). The tower-base fore-aft moment is affected by the rotor thrust, so tendencies are similar to those of the thrust. The tower-base side-to-side moment and yaw moment are eliminated by contra-rotating rotor in the case of the land-based model. The floating contra-rotating VAWT has the very small mean and STD values of side-to-side and torsional moments compared to those of the conventional VAWT, so it can be negligible.



(a) Fore-aft moment



(b) Side-to-side moment

(c) Yaw moment
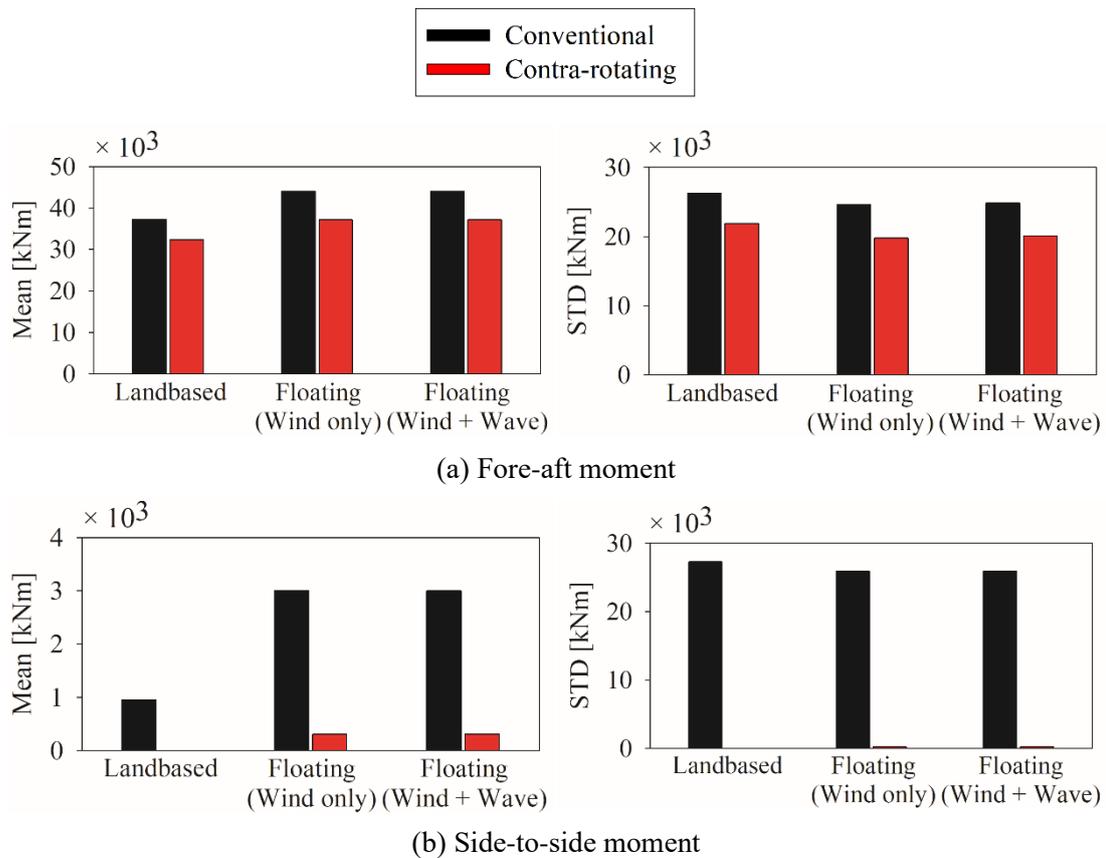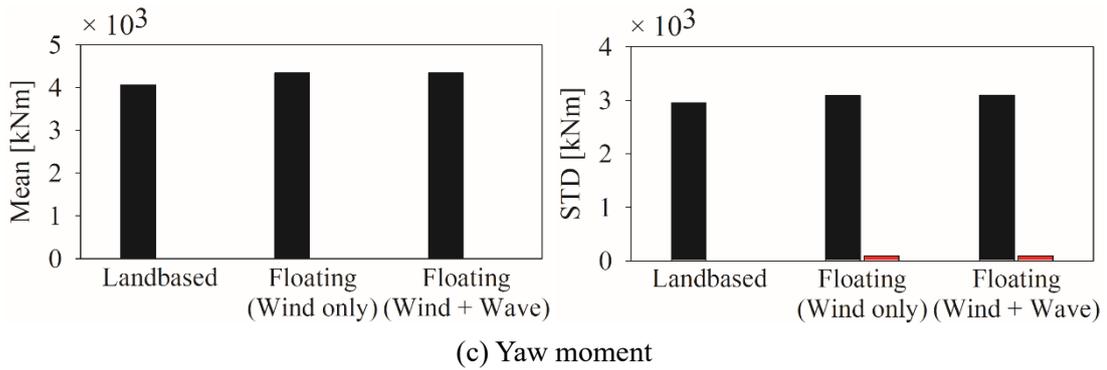
Figure 4.7 Tower-base loads of the conventional VAWT and contra-rotating VAWT

The resultant mooring line top tension is also assessed. As mentioned in Chapter 3, the mooring line in weather side (L1) has a more significant tension than other two mooring lines because the platform is pushed along the x-axis due to the influence of steady wind as can be seen in Figure 4.6(a). Figure 4.8 shows the mean and STD values of the tension at the fairlead of mooring line #2. In the case of the contra-rotating VAWT under the wind and wave loads, the mean tension decreases by 3.66% and the STD by 8.63%. The reduced standard deviations of the tension mean the fatigue loads at the fairlead is lowered.
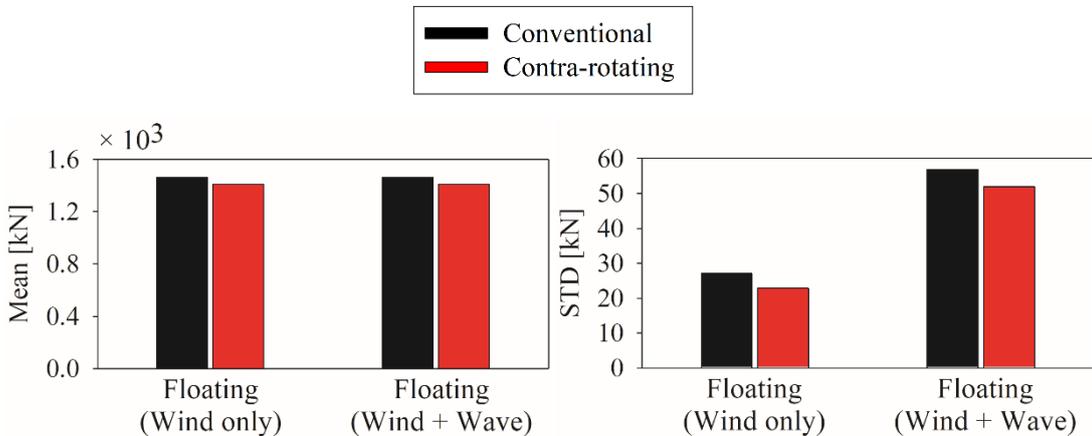


Figure 4.8 Mean and STD values of the tension at fairlead of a mooring line in weather side

From those results, it is found that the contra-rotating VAWT shows better structural response than the conventional. The less mean value of the structural response means that the design of the tower and substructure does not have to be as sturdy as it is. Furthermore, less STD value of the structural response will result in reduced fatigue loads on the structure, including the mooring, leading to longer fatigue life. Overall, the manufacturing and maintenance cost can be reduced by adopting the contra-rotating VAWT. On the contrary, the disadvantage of the contra-rotating rotor is the decrease in aerodynamic power. Nevertheless, because the life cycle could be longer by adopting the contra-rotating rotor, the power output during the total life cycle is expected to increase.

For further investigation, after adjusting the rotor radius and blade length to achieve similar power outputs, the structural responses of the land-based model are compared. Firstly, the torque and power were calculated by varying the blade length. Other parameters kept constant. Interference occurs between the two rotors because the hub position was fixed and the blade length increased, but the interference was ignored.

Figure 4.9 presents the mean value of the total aerodynamic torque and power of the conventional VAWT and the contra-rotating VAWTs, having the blade length of 40 m, 48 m, 48.5 m and 50m for each rotor. If the blade length is 48.5m, the contra-rotating VAWT show almost the same torque and power as the conventional VAWT (Figure 4.9). In this case, the mean value of thrust increase by about 10.40 % (Figure 4.10 (a)). Consequently, the mean value of the tower-base fore-aft moment increases by about 16.68 % (Figure 4.10 (b)),

whereas the tower-base side-to-side and yaw moments are eliminated. The STD value of the

tower-base fore-aft moment also increases by 6.98 %.



(a) Total aerodynamic torque      (b) Total aerodynamic power
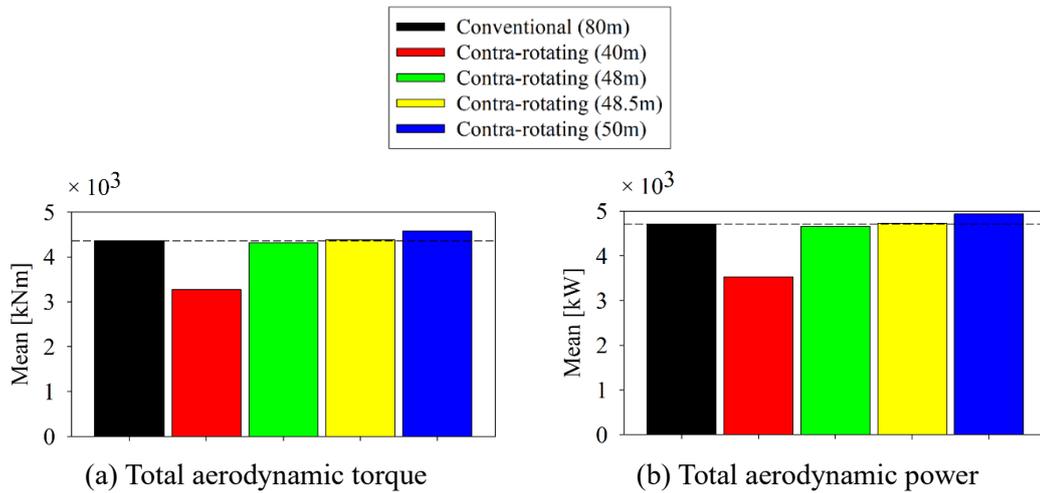
Figure 4.9 Mean value of the total aerodynamic torque and power by the change of the blade
length



(a) Thrust

(b) Tower-base fore-aft moment
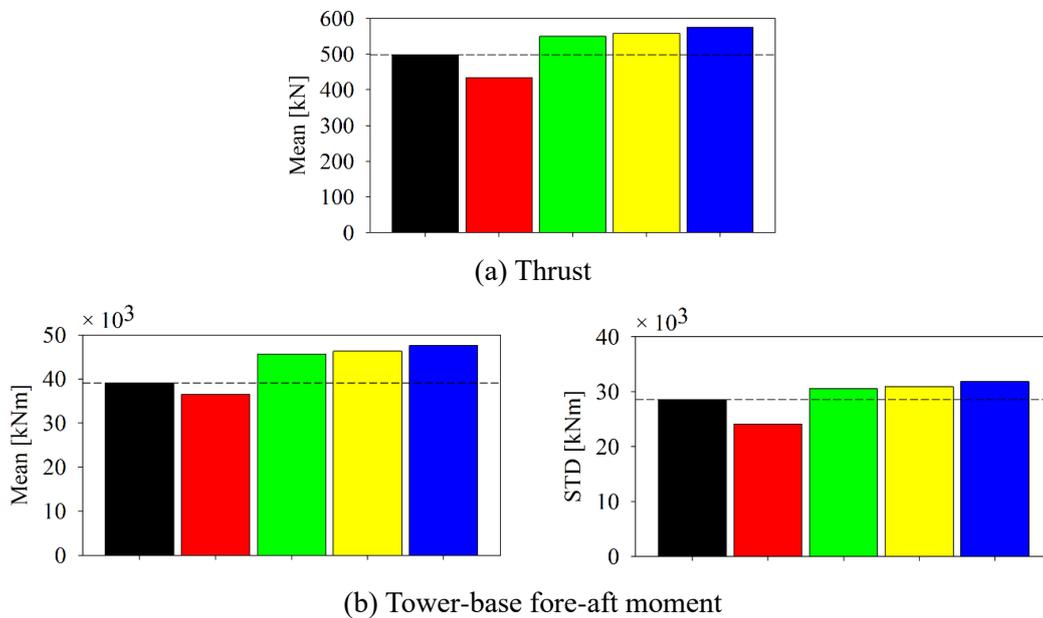
Figure 4.10 Mean and STD value of the thrust and the tower-base fore-aft moment by the
change of the blade length

Next results in Figure 4.11 are by the change of the rotor radius to obtain almost the same torque and power. Except for the rotor radius, the other parameters were not changed. The rotor radius of the contra-rotating VAWT was increased by 10 m and 15 m. As a result, when the rotor radius was 54 m, the power was the same as that of conventional VAWT.



(a) Total aerodynamic torque     (b) Total aerodynamic power
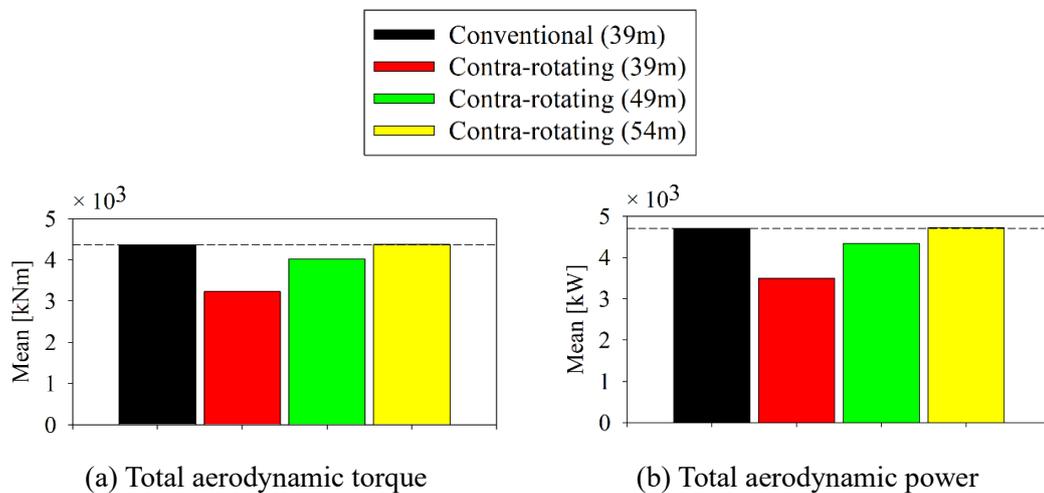
Figure 4.11 Mean value of the total aerodynamic torque and power by the change of the rotor radius

When the rotor radius is 54 m, the mean value of the thrust increases by 19.68 % (Figure 4.12 (a)), and the mean and STD value of the tower-base fore-aft moment increase by 25.95 % and 17.54 %, respectively (Figure 4.12 (b)).

(a) Thrust



(b) Tower-base fore-aft moment
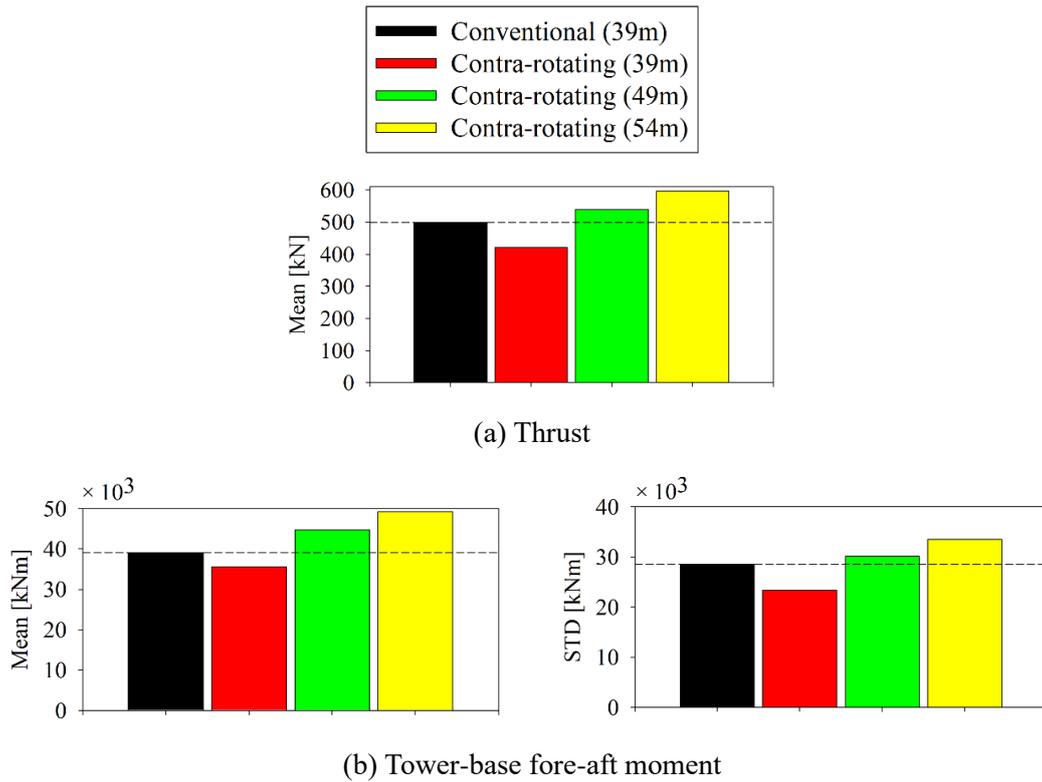
Figure 4.12 Mean and STD value of the thrust and the tower-base fore-aft moment by the change of the rotor radius

Thus the contra-rotating VAWT showed the same power as the conventional VAWT when the blade length becomes 48.5 m, or the rotor radius is 54 m. In both cases, the thrust of the rotor and the tower-base fore-aft moment increased more than the conventional VAWT. Although the side force and the tower-base side-to-side and yaw moments are not presented in these cases, it is apparent that those loads were eliminated regardless of the blade length or rotor radius due to the contra-rotating rotor. These results indicate the optimisation of the contra-rotating rotor design will lead to better results of both power and structural responses can be anticipated.

## 4.4 CONCLUSION

This study adopted a contra-rotating concept for the land-based and floating VAWTs to reduce the effect of torque on the structure and evaluated the rotor performance and tower-base loads. In the case of the floating VAWTs, the platform motions and mooring tension were also investigated. The developed integrated analysis code was advanced to be possible to analyse the contra-rotating rotor. For the simulation, all blades of the upper and lower rotors of the contra-rotating VAWT were assumed to be geometrically identical. Uniform wind speed was used to maintain the same rotational speed for both rotors.

Compared to the conventional VAWT, the contra-rotating VAWT led the decreases in the forces on rotor resulting in the reduction of the related platform motions and tower-base loads. The thrust, affecting the platform pitch motion and tower-base fore-aft moment, was still shown but reduced by about 15% compared to those of conventional VAWT. However, due to the reduced thrust, the torque of each rotor and the aerodynamic power were reduced. The side force was almost eliminated, resulting in the diminishes of the tower-base side-to-side moments. The advantage of the contra-rotating was obviously shown at the tower-base yaw moment and the platform yaw motion. The same amount of torque generated by the two rotors rotating in the opposite direction counteracted the tower-base yaw moment due to the opposite torque acting on the tower-base. Especially in the case of the floating model, the yaw motion of the platform cancelled out.

Consequently, notwithstanding the reduced aerodynamic power, the decreases in the

structural responses of the contra-rotating VAWT indicates lower manufacturing and maintenance costs and reduced fatigue loads by comparison with the conventional VAWT. Especially, under the offshore environment which requires robust design and high total costs and has the difficulties in maintenance, the better structural responses and loads and the reduced costs as a result of adopting the contra-rotating VAWT would be significant advantages.

# Chapter 5

# **CONCLUSIONS**

## 5.1 CONCLUSIONS

The interest in vertical-axis wind turbines (VAWTs) is recently increasing along with the growth of offshore wind industries. Although the VAWTs are rarely used for the onshore and offshore wind industries so far, the interest in it recently increases due to its advantages, compared to horizontal-axis wind turbines (HAWTs), when it is used for the floating offshore wind turbines. Although the technologies of VAWT is not as mature as that of HAWT up to now, many researchers have continuously proposed and investigated many concepts of VAWT.

In this study, a contra-rotating vertical-axis rotor was adopted for the floating offshore wind turbine, and the overall performance of the whole turbine system was evaluated. First of all, the aerodynamic analysis code for the conventional H-type VAWT was developed and verified by modifying the structure of a standalone code of AeroDyn ver15.03.00. Next, the integrated analysis code was developed for the VAWT, which can be used for the preliminary

design stage, based on FAST, which is the aero-hydro-servo-elastic analysis tool for HAWT. After verification of the developed integrated analysis code, the performance evaluation of the contra-rotating VAWT under the onshore and offshore environment was done by further development of the integrated analysis code.

In order to develop the aerodynamic analysis tool of VAWT, a double-multiple streamtube model (DMSM) was used, expecting the simple calculation and computational efficiency. Tip loss effect was considered to obtain more realistic results. As a result of comparing the DMSM results to the experimental and CFD results, it is shown that the DMSM might under- or overpredicted the aerodynamic loads, but it gave similar tendencies and magnitudes of the results as those from CFD.

For the integrated analysis code for floating offshore VAWTs, submodules AeroDyn and ElastoDyn of FAST ver. 8.16.00a-bjj were modified. The geometry data and mechanical parameters in the input files and the calculation process were modified appropriately for the VAWT. The other submodules remained intact. The verification was done by accounting for the aerodynamics, hydrodynamics and mooring systems. Due to the limit of the full information on the simulation model, elasticity and control strategies were not considered in this study. It is shown the performance of the floating offshore VAWT were well predicted using the developed integrated analysis code.

Using the further development of the integrated analysis code by adopting the contra-rotating concept, the performance of the land-based and floating contra-rotating

VAWT were evaluated compared to that of the conventional VAWT. Because of the contra-rotating rotor, the aerodynamic power was reduced, but the better tower-base yaw moment and platform yaw motion were shown. From the better structural responses and loads of the floating contra-rotating VAWT under the offshore environment, the less robust design and the reduced manufacturing and maintenance costs are anticipated.

## 5.2 RECOMMENDATIONS FOR FUTURE WORK

The further improvement of the developed integrated analysis code is required to predict more accurate and realistic wind turbine performance by including the various secondary effects in the calculation. These secondary effects are well described in [19]. One of the principal drawbacks of the VAWTs is the sophisticated unsteady aerodynamics. Dynamic stall is a principal impediment, which causes lower efficiencies. It arises from the significant and rapid changes in the angle of attack that occur on each blade during the rotation cycle. It introduces excessive structural vibrations, reduces efficiency, and produces unwanted noise. Therefore, massive efforts have been invested in developing modifications to the original DMSM to include dynamic stall [79][80][81][82][83][84]. Most of the dynamic stall models have been applied to DMSM by a series of semi-empirical procedures in the calculation of the lift and drag coefficients of the blades. That means additional interlaced steps are required within the main calculation procedure. Tower influence on the wind is another important effect since a blade passes through the low momentum wake behind a tower. It can be

considered by locally modifying the velocity field behind the tower through empirically derived correction factor.

In the present study, the wind loads were assumed to be steady due to the absence of the control strategies for the VAWT. The rotor power can be plotted against the rotational speed as a function of wind speed. For wind speeds below the rated wind speed, the designed rotational speed is determined by maximising the power capture. For the turbulence wind loads, the rotor should rotate instantaneously with the desired rotational speed. For this reason, the appropriate controller is required so that the turbulent wind loads can be considered in the simulation.

The specific properties of the tower and blades are also required to predict the forces and moments of the whole turbine. Scaling methods with the published data can achieve it. For the general use, it is also required to analyse on the different geometries of the VAWTs–for instance, phi (Φ)-rotor.

Concerning the contra-rotating VAWT, the parametric study should be carried out in further research. The optimisation to improve the performance using the contra-rotating rotor can be done with each rotor height, initial blade position, rotational speed, the distance between the upper and lower rotor, different number of blades for each rotor and so forth.

# BIBLIOGRAPHY

[1]  IRENA, *Global energy transformation-a roadmap to 2050*, 2018.

[2]  Available online: https://en.wikipedia.org/wiki/Cost_of_electricity_by_source (accessed on 22 November 2019)

[3]  GWEC, *Global Wind Report 2018*, 2019.

[4]  Bauer J, Available online: https://www.energy.gov/eere/articles/us-conditions-drive-inno vation-offshore-wind-foundations (accessed on 20 December 2019)

[5]  Wiser R, Jenni K, Seel J, Baker E, Hand M, Lantz E, Smith A, *Forecasting Wind Energy Costs and Cost Drivers: The Views of the World's Leading Experts*, Lawrence Berkeley National Laboratory, LBNL-1005717, 2016.

[6]  WindEurope, *Floating Offshore Wind Vision Statement*, 2017.

[7]  WindEurope, *Floating Offshore Wind Energy - A Policy Blueprint for Europe*, 2018.

[8]  Skopljak N, GE Haliade-X 12MW Produces First Power in Rotterdam. Available online: https://www.offshorewind.biz/2019/11/07/ge-haliade-x-12mw-produces-first-power-in-r otterdam/ (accessed on 19 November 2019)

[9]  Principle power, *Enabling a paradigm shift for the electricity sector in the US*, 2019.

[10]  Equinor, Available online: https://cloud.brandmaster.com/fr/gallery/34/images/lowres/d baf81569d7f4e50887b8718148871f6.png

[11]  MHI Vestas, Available online: http://www.mhivestasoffshore.com/first-turbine-of-wind float-atlantic-moves-into-position/ (accessed on 19 November 2019)

[12]  Gipe P, WIND-WORKS: Modern History of Vertical-Axis (Darrieus) Wind Turbines Published, Available online: http://www.wind-works.org/cms/index.php?id=64&tx_ttne ws%5Btt_news%5D=5322&cHash=345e48d80ec1772b603ff1c838ab3a6e (accessed on 19 November 2019)

[13]  Available online: http://www.verticalwindturbineinfo.com/vertical-axis-wind-turbine-de sign/ (accessed on 25 November 2019)

[14]  Jang H, Paek I, Kim S, Jeong D, "Performance prediction and validation of a small-capacity twisted savonius wind turbine," *Energies*, **12**(9), 1–12, 2019.

[15]  Diaz AP, Pajaro GJ, Salas KU, "Computational model of Savonius turbine," Ingeniare.

Revista chilena de ingeniería, **23**(3), 406–412, 2015.

[16] Darrieus G, "Turbine Having Its Rotating Shaft Transverse to the Flow of the Current," U.S. Patent 1835018, 8 December 1931.

[17] Shires A, "Design optimization of an offshore vertical axis wind turbine," *Proceedings of the Institution of Civil Engineers*, **166**(1), 7–18, February 2013.

[18] Tjiu W, Marnoto T, Mat S, Ruslan MH, Sopian K, "Darrieus vertical axis wind turbine for power generation I: Assessment of Darrieus VAWT configurations," *Renewable Energy*, **75**, 50–67, 2015.

[19] Borg M, Shires A, Collu M, "Offshore floating vertical axis wind turbines, dynamics modelling state of the art. Part I: Aerodynamics," *Renewable and Sustainable Energy Reviews*, **39**, 1214–1225, 2014.

[20] Chaichana T, Chaitep S, "Performance Evaluation of Co-Axis Counter-Rotation Wind Turbine," *Energy Procedia*, **79**, 149–156, 2015.

[21] Didane DH, Rosly N, Zulkafli MF, Shamsudin SS, "Performing evaluation of a novel vertical axis wind turbine with coaxial contra-rotating concept," *Renewable Energy*, **115**, 353–361, 2018.

[22] Alam MJ, Iqbal MT, "Design and development of hybrid vertical axis turbine," *2009 Canadian Conference on Electrical and Computer Engineering*, St. John's, NL, 1178–1183, 2009.

[23] Bhuyan S, Biswas A, "Investigations on self-starting and performance characteristics of simple H and hybrid H-Savonius vertical axis wind rotors," *Energy Conversion and Management*, **87**, 859–867, 2014.

[24] Sun X, Chen Y, Cao Y, Wu G, Zheng Z, Huang D, "Research on the aerodynamic characteristics of a lift drag hybrid vertical axis wind turbine," *Advances in Mechanical Engineering*, **8**(1), 1–11, 2016.

[25] Dwiyantoro BA, Suphandani V, "The system design and performance test of hybrid vertical axis wind turbine," *AIP Conference Proceedings*, **1831**, 020030, 2017.

[26] Small Wind Turbines, Available online: http://www.acelaenergy.com/aloha/products/small-wind-turbines/ (accessed on 19 November 2019)

[27] Vita L, Paulsen US, Pedersen TF, Madsen HA, Rasmussen F, "A novel floating offshore wind turbine concept," *Proceedings of the European Wind Energy Conference (EWEC)*, Marseille, France, 2009.

[28] Vita L, Pedersen FT, Madsen AH, "Offshore vertical axis wind turbine with floating and rotating foundation," Risø-PhD-80(EN), Technical University of Denmark, 2011.

[29] Dabiri JO, "Potential order-of-magnitude enhancement of wind farm power density via counter-rotating vertical-axis wind turbine arrays," *Journal of Renewable and Sustainable Energy*, **3**, 043104, 2011.

[30] Ertem S, "Enhancing the features of vertical axis wind turbines with active flap control and airfoil design," *Master of Sciences Thesis*, Delft University of Technology, 2015.

[31] Paillard B, "Numerical simulation and optimization of a crossflow axis tidal turbine with active pitch control", *PhD thesis*, 2011.

[32] Parneix N, Fuchs R, Immas A, Silvert F, Deglaire P, "Efficiency improvement of vertical-axis wind turbines with counter-rotating lay-out," *Proceedings of the EWEA*, Sep, 1–8, 2016.

[33] SeaTwirl, Available online: https://seatwirl.com/products/seatwirl-s1/ (accessed on 10 November 2019)

[34] SeaTwirl, Available online: https://seatwirl.com/products/seatwirl-s2/ (accessed on 10 November 2019)

[35] Wang K, Moan T, Hansen MOL, "A method for modeling of floating vertical axis wind turbine," *Proceedings of the ASME 2013 32nd International Conference on Ocean, Offshore and Arctic Engineering*, 2013.

[36] Wang K, Hansen MOL, Moan T, "Model improvements for evaluating the effect of tower tilting on the aerodynamics of a vertical axis wind turbine," *Wind Energy*, **18**, 91–110, 2015.

[37] Collu M, Borg M, Shires A, Brennan FP, "FloVAWT: progress on the development of a coupled model of dynamics for floating offshore vertical axis wind turbines," *Proceedings of the ASME 2013 32nd International Conference on Ocean, Offshore and Arctic Engineering*, Nantes, France, June 2013.

[38] Collu M, Borg M, Shires A, Rizzo FN, Lupi E, "FloVAWT: further progresses on the development of a coupled model of dynamics for floating offshore VAWTs," *Proceedings of the ASME 2014 33rd International Conference on Ocean, Offshore and Arctic Engineering*, San Francisco, California, June 2014.

[39] Fowler MJ, Owens B, Bull D, Goupee AJ, Hurtado J, Griffith DT, Alves M, "Hydrodynamic Module Coupling in the Offshore Wind Energy Simulation (OWENS) Toolkit," *Proceedings of the ASME 2014 33rd International Conference on Ocean, Offshore and Arctic Engineering*, San Francisco, California, USA, June 2014.

[40] Madsen HA, Larsen T, Vita L, Paulsen U, "Implementation of the Actuator Cylinder flow model in the HAWC2 code for aeroelastic simulations on Vertical Axis Wind Turbines," *Proceedings of 51st AIAA Aerospace Sciences Meeting including the New Horizons Forum and Aerospace Exposition*, 2013.

[41] Paulsen US, Vita L, Madsen HA, Hattel JH, Ritchie E, Leban KM, Berthelsen PA, Carstensen S, "1st DeepWind 5MW baseline design," *Energy Procedia*, **24**, 27–35, 2012.

[42] Paulsen US, Madsen HA, Hattel JH, Baran I, Nielsen PH, "Design Optimization of a 5 MW Floating Offshore Vertical-Axis Wind Turbine," *Energy Procedia*, **35**, 22–32, 2013.

[43] Cheng Z, Madsen HA, Gao Z, Moan T, "A fully coupled method for numerical modeling and dynamic analysis of floating vertical axis wind turbines," *Renewable Energy*, **107**, 604–619, 2017.

[44] Jonkman BJ, Michalakes J, Jonkman JM, Buhl ML, Platt A. Jr., Sprague, "NWTC Programmer's Handbook: A Guide for software development within the FAST computer-aided engineering tool," Technical Report, NREL/TP-xxxx-xxxxx, NREL, 2012.

[45] Duncan WJ, *An Elementary Treatise on the Mechanics of Fluids*, Edward Arnold Ltd, 1962.

[46] Templin RJ, "Aerodynamic performance theory for the NRC vertical-axis wind turbine," LTR-LA-190, NRC Lab, 1974.

[47] Wilson RE, Lissaman PB, *Applied aerodynamics of wind power machines*. (PB-238595). Corvallis (USA), Oregon State University, 1974.

[48] Strickland JH, "The Darrieus turbine: a performance prediction model using multiple streamtubes," SAND75-0431. Albuquerque, USA: Sandia National Laboratories; October 1975.

[49] Lapin EE, "Theoretical Performance of Vertical-Axis Wind Machines," ASME paper 75-WA/ENER-1, 1975.

[50] Newman BG, "Actuator-Disk Theory for Vertical-Axis Wind Turbines," *Journal of Wind Engineering and Industrial Aerodynamics*, **15**, 347, 1983.

[51] Paraschivoiu I, "Double-multiple streamtube model for Darrieus wind turbines," *Second DOE/ NASA wind turbines dynamics workshop*, NASACP-2186, Cleveland, OH; February 1981,19–25, 1981.

[52] Paraschivoiu I, *Wind turbine design: emphasis on the Darrieus concept*. 1st edition. Montreal: Polytechnic International Press, 2002.

[53] Islam M, Ting DSK, Fartaj A, "Aerodynamic models for Darrieus-type straight-bladed vertical axis wind turbines," *Renewable and Sustainable Energy Reviews*, **12**(4), 1087–1109, 2008.

[54] Madsen HA, *The Actuator Cylinder – A Flow Model for Vertical Axis Wind Turbines*. Institute of Industrial Constructions and Energy Technology, Aalborg University Centre, Denmark, 1982.

[55] Prandtl L, Göttinger Klassiker der Strömungsmechanik Bd, **3**, 89–92 (in German), 1919.

[56] Willmer AC, *Aerodynamic Investigation into the Feasibility of a 25 m Vertical-Axis Windmill*, 1979.

[57] Jonkman JM, Hayman GJ, Jonkman BJ, Damiani RR, Murray RE, *AeroDyn v15 User's Guide and Theory Manual (Draft version)*, NREL, 2017.

[58] Marten D, Wendler J, Pechlivanoglou G, Nayen CN, Paschereit CO, "Qblade: An Open

Source Tool for Design and Simulation of Horizontal and Vertical Axis Wind Turbines", *International Journal of Emerging Technology and Advanced* Engineering, **3**(3), 264–269, 2013.

[59] Castelli MR, Englaro A, Bernini E, "The Darrieus wind turbine: Proposal for a new performance prediction model based on CFD," *Energy*, **36**(8), 4919–4934, 2011.

[60] Lei H, Zhou D, Bao Y, Li Y, Han Z, "Three-dimensional Improved Delayed Detached Eddy Simulation of a two-bladed vertical axis wind turbine," *Energy Conversion and Management*, **133**, 235–248, 2017.

[61] Shur ML, Spalart PR, Strelets MK, Travin AK, "A hybrid RANS-LES approach with delayed-DES and wall-modelled LES capabilities," *International Journal of Heat Fluid Flow*, **29**(6), 1638–1649, 2008.

[62] Jonkman JM, "Dynamics Modeling and Loads Analysis of an Offshore Floating Wind Turbine," Technical Report, NREL/TP-500-41958, November 2007.

[63] Jonkman JM, "Modeling of the UAE Wind Turbine for Refinement of FAST_AD," Technical Report, NREL/TP-500-34755, December 2003.

[64] Guo Y, Liu L, Gao X, Xu W, "Aerodynamics and motion performance of the H-type floating vertical axis wind turbine," *Applied Science*, **8**, 262, 2018.

[65] Jonkman JM, Sciavounos PD, "Development of fully coupled aeroelastic and hydrodynamic models for offshore wind turbines," NREL/CP-500-39066, NREL, 2006.

[66] Jonkman JM, Buhl Jr ML, "Development and verification of a fully coupled simulator for offshore wind turbines," NREL/CP-500-40979, NREL, 2007.

[67] Jonkman JM, "Dynamics modelling and loads analysis of an offshore floating wind turbine," *Technical Report*, NREL/TP-500-41958, NREL, 2007.

[68] Jonkman JM, "Dynamics of offshore floating wind turbines–Model development and verification," *Wind Energy*, **12**, 459–492, 2009.

[69] Hall M, *MoorDyn User's Guide*, 2017.

[70] MAP++, Available online: https://map-plus-plus.readthedocs.io/en/latest/index.html (accessed on 20 December 2019)

[71] Bae YH, *Development of a Dynamic Mooring Module FEAM for FAST v8*.

[72] Cheng Z, Madsen HA, Gao Z, Moan T, "Effect of the number of blades on the dynamics of floating straight-bladed vertical axis wind turbines," *Renewable Energy*, **101**, 1285–1298, 2017.

[73] Robertson A, Jonkman J, Masciola, M, Song H, Goupee A, Coulling A, Luan C, "Definition of the semisubmersible floating system for phase II of OC4," Technical Report, NREL/TP-5000-60601, NREL, 2014.

[74] Ramachandran GKV, Robertson A, Jonkman JM, Masciola MD, "Investigation of response amplitude operators for floating offshore wind turbines," *Proceedings of the*

*23rd International Ocean, Offshore and Polar Engineering Conference, Anchorage*, Alaska, June–July 2013.

[75] Cheng Z, Wang K, Gao Z, Moan T, "Dynamic response analysis of three floating wind turbine concepts with a two-bladed Darrieus rotor," *Journal of Ocean Wind Energy*, **2**, 213–222, 2015.

[76] Michael Frey, Available online: https://commons.wikimedia.org/wiki/File:Counter-rotating_propellers.gif (accessed on 6 October 2019)

[77] Michael Frey, Available online: https://commons.wikimedia.org/wiki/File:Contra-rotating_propellers.gif (accessed on 6 October 2019)

[78] Molland AF, *The Maritime engineering reference book: A guide to ship design, construction and operation*: Chapter 5. 2008.

[79] Gormont RE, Boeing Vertol Company, "A mathematical model of unsteady aerodynamics and radial flow for application to helicopter rotors," Technical Report AD-767 240, Army Air Mobility Research and Development Laboratory, Philadelphia, Pa, May 1973. Distributed by National Technical Information Service.

[80] Berg DE, "Improved double-multiple streamtube model of the Darrieus-type vertical axis wind turbine," *American Solar Energy Society Meeting*, Minneapolis, 1983.

[81] Strickland JH, Nguyen T, Webster BT, Sandia National Laboratories, United States Department of Energy, "A vortex model of the Darrieus turbine: an analytical and experimental study," Sandia Laboratories, 1980.

[82] Paraschivoiu I, "Double-multiple streamtube model for studying vertical-axis wind turbines," *AIAA Journal of Propulsion and Power*, **4**, 370–378, 1988.

[83] Beddoes TS, Leishman JG, "A semiempirical model for dynamic stall," *Journal of the American Helicopter Society*, **34**(3), 3–17, 1989.

[84] Hansen MH, Gaunaa M, Madsen HA, "A Beddoes-Leishman type dynamic stall model in state-space and indicial formulations," Technical Report Risøo-R-1354, Risøo National Laboratory, Roskilde, Denmark, 2004.